

# Fundamental limits on the rate of bacterial cell division

Nathan M. Belliveau<sup>†, 1</sup>, Griffin Chure<sup>†, 2</sup>, Christina L. Hueschen<sup>3</sup>, Hernan G. Garcia<sup>4</sup>, Jane Kondev<sup>5</sup>, Daniel S. Fisher<sup>6</sup>, Julie A. Theriot<sup>1, 7, \*</sup>, Rob Phillips<sup>8, 9, \*</sup>

<sup>1</sup>Department of Biology, University of Washington, Seattle, WA, USA; <sup>2</sup>Department of Applied Physics, California Institute of Technology, Pasadena, CA, USA; <sup>3</sup>Department of Chemical Engineering, Stanford University, Stanford, CA, USA; <sup>4</sup>Department of Molecular Cell Biology and Department of Physics, University of California Berkeley, Berkeley, CA, USA; <sup>5</sup>Department of Physics, Brandeis University, Waltham, MA, USA; <sup>6</sup>Department of Applied Physics, Stanford University, Stanford, CA, USA; <sup>7</sup>Allen Institute for Cell Science, Seattle, WA, USA; <sup>8</sup>Division of Biology and Biological Engineering, California Institute of Technology, Pasadena, CA, USA; <sup>9</sup>Department of Physics, California Institute of Technology, Pasadena, CA, USA; \*Co-corresponding authors. Address correspondence to phillips@pboc.caltech.edu and jtheriot@uw.edu; <sup>†</sup>These authors contributed equally to this work

14

**Abstract** Recent years have seen a deluge of experiments dissecting the relationship between bacterial growth rate, cell size, and protein content, quantifying the abundance of proteins across growth conditions with unprecedented resolution. However, we still lack a rigorous understanding of what sets the scale of these quantities and when protein abundances should (or should not) depend on growth rate. Here, we seek to quantitatively understand this relationship across a collection of *Escherichia coli* proteomic data sets covering  $\approx$  4000 proteins and 36 growth rates. We estimate the basic requirements for steady-state growth by considering key processes in nutrient transport, energy generation, cell envelope biogenesis, and the central dogma. From these estimates, ribosome biogenesis emerges as a primary determinant of growth rate. We expand on this assessment by exploring a model of ribosomal regulation as a function of the nutrient supply, revealing a mechanism that ties cell size and growth rate to ribosomal content.

25

## Introduction

The observed range of bacterial growth rates is enormously diverse. In natural environments, some microbial organisms may double only once per year (*Mikucki et al., 2009*) while in comfortable laboratory conditions, growth can be rapid with several divisions per hour (*Schaechter et al., 1958*). This six order-of-magnitude difference in time scales encompasses different microbial species and lifestyles, yet even for a single species such as *Escherichia coli*, the growth rate can be modulated over a comparably large scale by tuning the type and amount of nutrients in the growth medium. This remarkable flexibility in growth rate illustrates the intimate relationship between environmental conditions and the rates at which cells convert nutrients into new cellular material – a relationship that has remained a major topic of inquiry in bacterial physiology for over a century (*Jun et al., 2018*).

Jacques Monod once remarked that “the study of the growth of bacterial cultures does not constitute a specialized subject or branch of research, it is the basic method of Microbiology.” Those words ring as true today as they did when they were written 70 years ago (*Monod, 1949*) with the quantitative power of this “method” recently undergoing renaissance. Many of the key questions addressed by the pioneering efforts in the middle of the last century can be revisited by examining them through the lens of the increasingly refined molecular census that is available for bacteria such as the microbial workhorse *E. coli*.

Several of the evergreen questions about bacterial growth and physiology that were originally raised by

42 microbiologists in the middle of the 20th century can now be reframed in light of this newly available data. For  
43 example, what biological processes are the primary determinants for how quickly bacterial cells can grow and  
44 reproduce? How do cells modulate the absolute numbers and relative ratios of their molecular constituents as  
45 a function of changes in growth rate or nutrient availability? In this paper, we begin by considering these two  
46 questions from two distinct angles. First, as a result of an array of high-quality proteome-wide measurements of *E.*  
47 *coli* under diverse growth conditions, we have a census that allows us to explore how the number of key molecular  
48 players change as a function of growth rate. Here, we have assembled a singular data set using measurements  
49 collected over the past decade via mass spectrometry (*Schmidt et al., 2016; Peebo et al., 2015; Valgepea et al.,  
50 2013*) or ribosomal profiling (*Li et al., 2014*) of the composition of the *E. coli* proteome across 36 unique growth  
51 rates (see Appendix Experimental Details Behind Proteomic Data for further discussion of the data). Second,  
52 by compiling molecular turnover rate measurements for many of the fundamental processes associated with  
53 bacterial growth, we make quantitative estimates of key cellular processes (schematized in *Figure 1*) to determine  
54 whether our current understanding of the dynamics of these processes are sufficient to explain the magnitude  
55 of the observed protein copy numbers across conditions. The census, combined with these estimates, provide a  
56 window into the question of whether the rates of central processes such as energy generation or DNA synthesis  
57 are regulated systematically as a function of cell growth rate by altering protein copy number.

58 Throughout our estimates, we consider an archetypal growth rate of  $\approx 0.5 \text{ hr}^{-1}$  corresponding to a doubling  
59 time of  $\approx 5000$  seconds, as the data sets examined here heavily sample this growth regime. While we formulate  
60 point estimates for the protein abundances at this division time, we also consider how these values will vary  
61 at other growth rates due to changes in cell size, surface area, and chromosome copy number (*Taheri-Araghi  
62 et al., 2015*). Broadly, we find that the protein copy numbers appeared tuned for the task of cell doubling across  
63 a continuum of growth rates for the majority of the processes estimated here. Thus, our understanding of the  
64 kinetics of myriad biological processes is sufficient to quantitatively explain the observed abundances of these  
65 proteins.

66 From these estimates, it emerges that translation, particularly the synthesis of ribosomal proteins, is a plausible  
67 candidate that limits the rate of cell division. We reach this conclusion by considering that ribosome synthesis is  
68 1) a rate limiting step for the *fastest* bacterial division, and 2) a major determinant of bacterial growth across the  
69 nutrient conditions we have considered under steady state, exponential growth. This enables us to suggest that the  
70 long-observed correlation between growth rate and cell size (*Schaechter et al., 1958; Si et al., 2017*) can be simply  
71 attributed to the increased absolute number of ribosomes per cell under conditions supporting extremely rapid  
72 growth. To better understand how the observed alterations in absolute protein abundances, and in particular,  
73 changes in ribosome copy number, influence growth rate across different nutrient conditions we consider a  
74 minimal model of cellular growth. Our conclusions from these analyses provide important insight into how *E.*  
75 *coli* regulates growth across conditions of differing nutrient availability and identifies fundamental constraints in  
76 bacterial growth more broadly.

## 117 Nutrient Transport

118 We begin by considering the critical transport processes diagrammed in *Figure 1(A)*. In order to build new cellular  
119 mass, the molecular and elemental building blocks must be scavenged from the environment in different forms.  
120 Carbon, for example, is acquired via the transport of carbohydrates and sugar alcohols with some carbon sources  
121 receiving preferential treatment in their consumption (*Monod, 1947*). Phosphorus, sulfur, and nitrogen, on the  
122 other hand, are harvested primarily in the forms of inorganic salts, namely phosphate, sulfate, and ammonia (*Jun  
123 et al., 2018; Assentoft et al., 2016; Stasi et al., 2019; Antonenko et al., 1997; Rosenberg et al., 1977; Willsky et al.,  
124 1973*). All of these compounds have different membrane permeabilities (*Phillips, 2018*) and most require some  
125 energetic investment either via ATP hydrolysis or through the proton electrochemical gradient to bring the material  
126 across the hydrophobic cell membrane.

127 The elemental composition of *E. coli* has received much quantitative attention over the past half century  
128 (*Neidhardt et al., 1991; Taymaz-Nikerel et al., 2010; Heldal et al., 1985; Bauer and Ziv, 1976*), providing us with  
129 a starting point for estimating how many atoms of each element must be scavenged from the environment. A  
130 synthesis of these studies presents an approximate dry mass composition of  $\approx 50\%$  carbon (BNID: 100649, see  
131 *Box 1*),  $\approx 15\%$  nitrogen (BNID: 106666),  $\approx 3\%$  phosphorus (BNID: 100653), and 1% sulfur (BNID: 100655) with

78 **Box 1. The Rules of Engagement for Order-Of-Magnitude Estimates**

79 This work relies heavily on "back-of-the-envelope" estimates to understand the growth-rate dependent  
80 abundances of molecular complexes. This moniker arises from the limitation that any estimate should be  
81 able to fit on the back of a postage envelope. As such, we must draw a set of rules governing our precision  
82 and sources of key values.

83 **The rule of "one, few, and ten".** The philosophy behind order-of-magnitude estimates is to provide a estimate  
84 of the appropriate scale, not a prediction with many significant digits. We therefore define three different  
85 scales of precision in making estimates. The scale of "one" is reserved for values that range between 1 and 2.  
86 For example, If a particular process has been experimentally measured to transport 1.87 protons for a process  
87 to occur, we approximate this process to require 2 protons per event. The scale of "few" is reserved for values  
88 ranging between 3 and 7. For example, we will often use Avogadro's number to compute the number of  
89 molecules in a cell given a concentration and a volume. Rather than using Avogadro's number as  $6.02214 \times 10^{23}$ ,  
90 we will approximate it as  $5 \times 10^{23}$ . Finally, the scale of "ten" is reserved for values which we know within an  
91 order of magnitude. If a particular protein complex is present at 883 copies per cell, we say that it is present  
92 in approximately  $10^3$  copies per cell. These different scales will be used to arrive at simple estimates that  
93 report the expected scale of the observed data. Therefore, the estimates presented here should not be viewed  
94 as hard-and-fast predictions of precise copy numbers, but as approximate lower (or upper) bounds for the  
95 number of complexes that may be needed to satisfy some cellular requirement.  
96 Furthermore, we use equality symbols (=) sparingly and frequently defer to approximation ( $\approx$ ) or scaling ( $\sim$ )  
97 symbols when reporting an estimate. When  $\approx$  is used, we are implicitly stating that we are confident in this  
98 estimate within a factor of a few. When a scaling symbol  $\sim$  is used, we are stating that we are confident in our  
99 estimate to within an order of magnitude.

100 **The BioNumbers Database as a source for values.** In making our estimates, we often require approximate  
101 values for key cellular properties, such as the elemental composition of the cell, the average dry mass, or  
102 approximate rates of synthesis. We rely heavily on the BioNumbers Database ([bionumbers.hms.harvard.edu](http://bionumbers.hms.harvard.edu),  
103 **Milo et al. (2010)**) as a repository for such information. Every value we draw from this database has an  
104 associated BioNumbers ID number, abbreviated as BNID, and we provide this reference in grey-boxes in each  
105 figure.

106 **Uncertainty in the data sets and the accuracy of an estimate.** The data sets presented in this work are the  
107 products of careful experimentation with the aim to report, to the best of their ability, the absolute copy  
108 numbers of proteins in the cell. These data, collected over the span of a few years, come from different  
109 labs and use different internal standards, controls, and even techniques (discussed further in Appendix  
110 Experimental Details Behind Proteomic Data). As a result, there is notable disagreement in the measured copy  
111 numbers for some complexes across data sets. In assessing whether our estimates could explain the observed  
112 scales and growth-rate dependencies, we also considered the degree of variation between the different data  
113 sets. For example, say a particular estimate undercuts the observed data by an order of magnitude. If all  
114 data sets agree within a factor of a few of each other, we revisit our estimate and consider what me may  
115 have missed. However, if the data sets themselves disagree by an order of magnitude, we determine that our  
116 estimate is appropriate given the variation in the data.

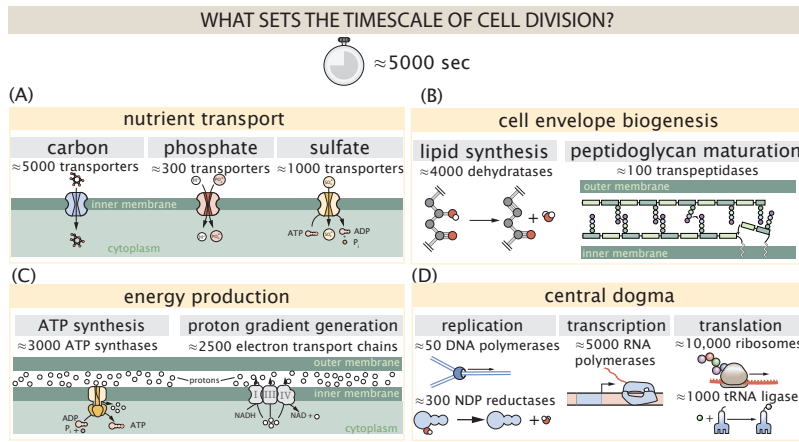


**Figure 1. Transport and synthesis processes necessary for cell division.** We consider an array of processes necessary for a cell to double its molecular components, broadly grouped into four classes. These categories are (A) nutrient transport across the cell membrane, (B) cell envelope biogenesis, (C) energy production (namely, ATP synthesis), and (D) processes associated with the central dogma. Numbers shown are the approximate number of complexes of each type observed at a growth rate of  $0.5 \text{ hr}^{-1}$ , or a cell doubling time of  $\approx 5000$  s.

132 remainder being attributable to oxygen, hydrogen, and various transition metals. We use this stoichiometric  
 133 breakdown to estimate the abundance and growth rate dependence of a variety of transporters responsible for  
 134 carbon uptake, and provide more extensive investigation of the other critical elements – phosphorus, sulfur, and  
 135 nitrogen – in the Appendix Additional Estimates of Fundamental Biological Processes.

136 Using  $\approx 0.3 \text{ pg}$  as the typical *E. coli* dry mass at a growth rate of  $\approx 0.5 \text{ hr}^{-1}$  (BNID: 103904), coupled with an  
 137 approximation that  $\approx 50\%$  of this mass is carbon, we estimate that  $\sim 10^{10}$  carbon atoms must be brought into  
 138 the cell in order to double all of the carbon-containing molecules (Figure 2(A), top). Typical laboratory growth  
 139 conditions provide carbon as a single class of sugar (such as glucose, galactose, or xylose) often transported cross  
 140 the cell membrane by a transporter complex specific to that particular sugar. One such mechanism of transport  
 141 is via the PTS system which is a highly modular system capable of transporting a diverse range of sugars with  
 142 high specificity (Escalante *et al.*, 2012). The glucose-specific component of this system transports  $\approx 200$  glucose  
 143 molecules ( $\approx 1200$  carbon atoms) per second per transporter (BNID: 114686). Making the assumption that this is a  
 144 typical sugar transport rate for the PTS system, coupled with the need to transport  $\sim 10^{10}$  carbon atoms, we then  
 145 expect on the order of  $\approx 1000$  transporters must be expressed per cell in order to bring in enough carbon atoms  
 146 (Figure 2(A), top).

147 However, we find this estimate to be exceeded by several fold by experimental measurements (Figure 2(A),  
 148 bottom), implying that the cell is capable of transporting more carbon atoms than strictly needed for biosynthesis.  
 149 While we estimate  $\approx 1000$  transporters are needed with a 5000 second division time, we can abstract this calculation  
 150 to consider any particular growth rate given knowledge of the cell density and volume as a function of growth rate  
 151 and direct the reader to the Appendix Extending Estimates to a Continuum of Growth Rates for more information.  
 152 This abstraction, shown as a grey line in Figure 2(A), reveals an excess of transporters even at faster growth rates.  
 153 This contrasts with our observations for uptake of phosphorus and sulfur, which align well with our expectations  
 154 across different growth conditions (Figure 2–Figure Supplement 1 and discussed further in Appendix Additional  
 155 Estimates of Fundamental Biological Processes).

156 It is important to note, however, that this estimate neglects any specifics of the regulation of the carbon  
 157 transport system. Using the diverse array of growth conditions available in the data, we can explore how individual  
 158 carbon transport systems depend on specific carbon availability. In Figure 2(B), we show the total number of  
 159 carbohydrate transporters specific to different carbon sources. A striking observation, shown in the top-left plot of  
 160 Figure 2(B), is the constancy in the expression of the glucose-specific transport systems, an observation that stands  
 161 in contrast with other species of transporters. Additionally, we note that the total number of glucose-specific  
 162 transporters is tightly distributed at  $\approx 10^4$  per cell, the approximate number of transporters needed to sustain  
 163 rapid growth of several divisions per hour. This illustrates that *E. coli* maintains a substantial number of complexes

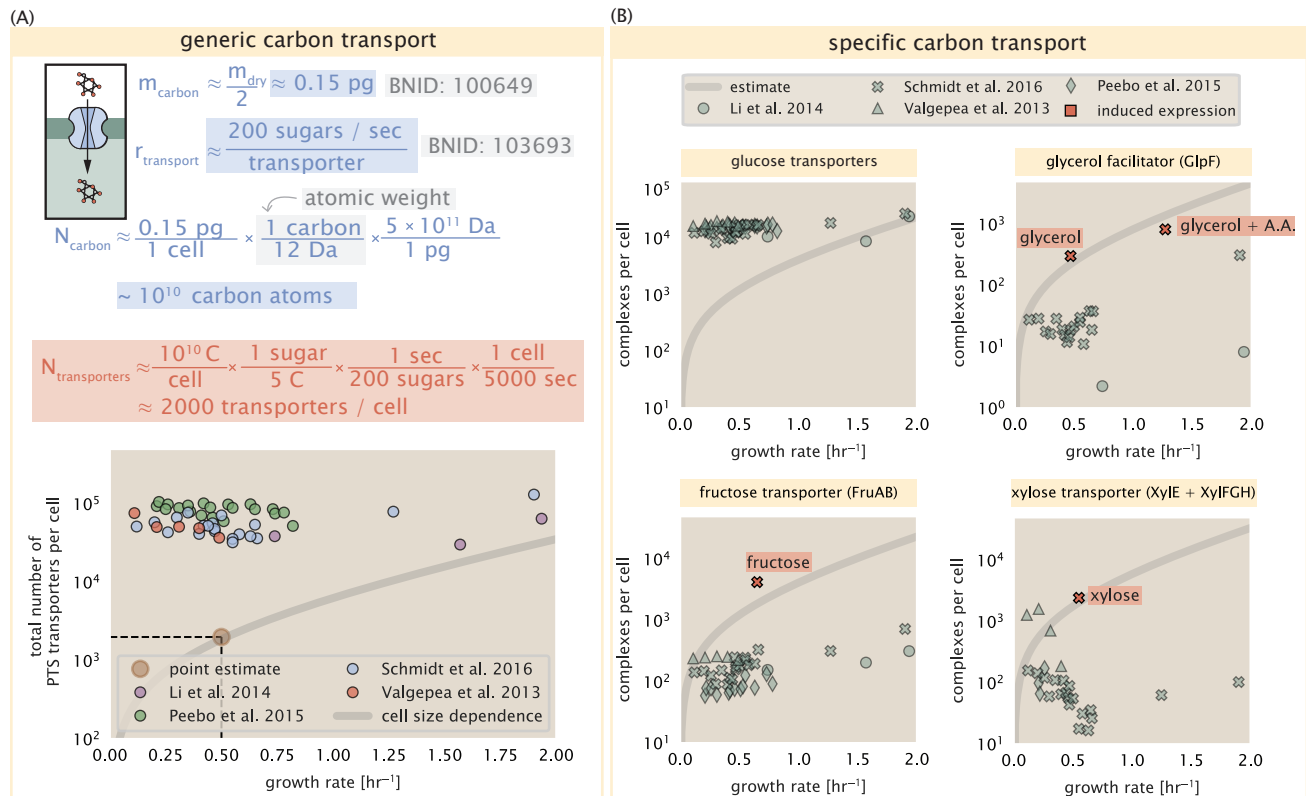


**Figure 2. The abundance of carbon transport systems across growth rates.** (A) A simple estimate for the minimum number of generic carbohydrate transport systems (top) assumes  $\sim 10^{10}$  C are needed to complete division, each transported sugar contains  $\approx 5$  C, and each transporter conducts sugar molecules at a rate of  $\approx 200$  per second. Bottom plot shows the estimated number of transporters needed at a growth rate of  $\approx 0.5$  per hr (light-brown point and dashed lines). Colored points correspond to the mean number of complexes involved in carbohydrate import (complexes annotated with the Gene Ontology terms GO:0009401 and GO:0098704) for different growth conditions across different published datasets. (B) The abundance of various specific carbon transport systems plotted as a function of the population growth rate. The rates of substrate transport differ between these transporter species. To compute the continuum growth rate estimate (grey line), we used the following transport rates for each transporter species: 200 glucose-  $\text{s}^{-1}$  (BNID: 103693), 2000 glycerol- $\text{s}^{-1}$  (*Lu et al., 2003*), 200 fructose-  $\text{s}^{-1}$  (assumed to be similar to PtsI, BNID: 103693), and 50 xylose- $\text{s}^{-1}$  (assumed to be comparable to LacY, BNID:103159). Red points and highlighted text indicate conditions in which the only source of carbon in the growth medium induces expression of the transport system. Grey lines in (A) and (B) represents the estimated number of transporters per cell at a continuum of growth rates.

**Figure 2-Figure supplement 1.** Estimates and observed abundances of phosphate and sulfate transporters.

164 present for transporting glucose regardless of growth condition, which is known to be the preferential carbon  
165 source (*Monod, 1947; Liu et al., 2005; Aidelberg et al., 2014*).

166 Many metabolic operons are regulated with dual-input logic gates that are only expressed when glucose  
167 concentrations are low and the concentration of other carbon sources are elevated (*Gama-Castro et al., 2016;*  
168 *Zhang et al., 2014b; Gama-Castro et al., 2016; Belliveau et al., 2018; Ireland et al., 2020*). Points colored in red in  
169 *Figure 2(B)* (labeled by red text-boxes) correspond to growth conditions in which the specific carbon source (glycerol,  
170 xylose, or fructose) is present as the sole source of carbon. The grey lines in *Figure 2(B)* show the estimated number  
171 of transporters needed at each growth rate to satisfy the cellular carbon requirement, adjusted for the specific  
172 carbon source in terms of number of carbon atoms per molecule and the rate of transport for the particular  
173 transporter species. These plots show that, in the absence of the particular carbon source, expression of the  
174 transporters is maintained on the order of  $\sim 10^2$  per cell. The low but non-zero abundances may reflect the specific  
175 regulatory logic involved, requiring that cells are able to transport some minimal amount of an alternative carbon  
176 source in order to induce expression of these alternative carbon-source systems.

### 177 **Limits on Transporter Expression**

178 If acquisition of nutrients was a limiting process in cell division under the typical growth conditions explored  
179 here, the growth rate could be theoretically increased simply by expressing more transporters, but is this feasible  
180 at a physiological level? A way to approach this question is to compute the amount of space in the bacterial  
181 membrane that could be occupied by nutrient transporters. Considering a rule-of-thumb for the surface area  
182 of *E. coli* of about  $5 \mu\text{m}^2$  (BNID: 101792), we expect an areal density for 1000 transporters to be approximately  
183 200 transporters/ $\mu\text{m}^2$ . For a typical transporter occupying about  $50 \text{ nm}^2$ , this amounts to about only  $\approx 1\%$  of the  
184 total inner membrane area (*Szenk et al., 2017*). Additionally, bacterial cell membranes typically have densities  
185 of  $10^5$  proteins/ $\mu\text{m}^2$  (*Phillips, 2018*), implying that the cell could accommodate more membrane and this places  
186 additional limitations on cell size and surface area that we will consider further in the coming sections.

### 187 **Cell Envelope Biogenesis**

188 In contrast to nutrient transporters, which support the synthesis of biomolecules throughout the cell and therefore  
189 need to scale with the cell size, here we must consider the synthesis of components that will need to scale with  
190 the surface area of the cell. *E. coli* is a rod-shaped bacterium with a remarkably robust length-to-width aspect  
191 ratio of  $\approx 4:1$  (*Harris and Theriot, 2018; Ojic et al., 2019*). At modest growth rates, the total cell surface area is  
192  $\approx 5 \mu\text{m}^2$  (BNID: 101792). Assuming this surface area is approximately the same between the inner and outer  
193 membranes of *E. coli*, and the fact that each membrane is itself a lipid bilayer, cells have a the total membrane  
194 surface area of  $\approx 20 \mu\text{m}^2$  (see Appendix Estimation of Cell Size and Surface Area for a description of the calculation  
195 of cell surface area as a function of cell size). In this section, we will estimate the number of protein complexes  
196 needed to produce this membrane surface area as well as the complexes involved in assembling the peptidoglycan  
197 scaffold it encapsulates.

### 198 **Lipid Synthesis**

199 The dense packing of the membrane with proteins means that the cell membranes are not composed entirely of  
200 lipid molecules, with only  $\approx 40\%$  of the membrane area is occupied by lipids (BNID: 100078). Using a rule-of-thumb  
201 of  $0.5 \text{ nm}^2$  as the surface area of the typical lipid (BNID: 106993), we can estimate  $\sim 2 \times 10^7$  lipids per cell, which is  
202 in close agreement with experimental measurements (BNID: 100071, 102996).

203 The membranes of *E. coli* are composed of a variety of different lipids, each of which are unique in their  
204 structures and biosynthetic pathways (*Sohlenkamp and Geiger, 2016*). Recently, a combination of stochastic kinetic  
205 modeling (*Ruppe and Fox, 2018*) and *in vitro* kinetic measurements (*Ranganathan et al., 2012; Yu et al., 2011*)  
206 have revealed remarkably slow steps in the fatty acid synthesis pathways which may serve as the rate limiting  
207 reactions for making new membrane phospholipids. One such step is the removal of hydroxyl groups from the  
208 fatty-acid chain by ACP dehydratase that leads to the formation of carbon-carbon double bonds. This reaction,  
209 catalyzed by proteins FabZ and FabA in *E. coli* (*Yu et al., 2011*), have been estimated to have kinetic turnover  
210 rates of  $\approx 1$  dehydration per second per enzyme (*Ruppe and Fox, 2018*). Thus, given this rate and the need to  
211 synthesize  $\approx 2 \times 10^7$  lipids over 5000 seconds, one can estimate that a typical cell requires  $\approx 4000$  ACP dehydratases.

212 This is in reasonable agreement with the experimentally observed copy numbers of FabZ and FabA (*Figure 3(A)*).  
213 Furthermore, we can extend this estimate to account for the change in membrane surface area as a function of the  
214 growth rate (grey line in *Figure 3(A)*), which captures the observed growth rate dependent expression of these two  
215 enzymes.

## 216 Peptidoglycan Synthesis

217 Bacterial cells demonstrate exquisite control over their cell shape. This is primarily due to the cell wall, a stiff, several  
218 nanometer thick meshwork of polymerized disaccharides. The formation of the peptidoglycan is an intricate  
219 process involving many macromolecular players (*Shi et al., 2018; Morgenstein et al., 2015*), whose coordinated  
220 action maintains cell shape and integrity even in the face of large-scale perturbations (*Harris and Theriot, 2018;*  
221 *Shi et al., 2018*). The peptidoglycan alone comprises  $\approx 3\%$  of the cellular dry mass (BNID: 1019360, making it  
222 the most massive molecule in *E. coli*). The polymerized unit of the peptidoglycan is a N-acetylglucosamine and  
223 N-acetylmuramic acid disaccharide, of which the former is functionalized with a short pentapeptide. With a mass  
224 of  $\approx 1000$  Da, this unit, which we refer to as a murein monomer, it is polymerized to form long strands in the  
225 periplasm which are then attached to each other via their peptide linkers. Together, these quantities provide an  
226 estimate of  $\approx 5 \times 10^6$  murein monomers per cell.

227 The crosslinking of the pentapeptides between adjacent glycan strands is responsible for maintaining the  
228 structural integrity of the cell wall and, in principle, each murein monomer can be involved in such a crosslink.  
229 In some microbes, such as in gram-positive bacterium *Staphylococcus aureus*, the extent of crosslinking can be  
230 large with  $> 90\%$  of pentapeptides forming a connection between glycan strands. In *E. coli*, however, a much  
231 smaller proportion ( $\approx 20\%$ ) of the peptides are crosslinked, resulting in a weaker and more porous cell wall *Vollmer*  
232 *et al. (2008); Rogers et al. (1980)*. The formation of these crosslinks occurs primarily during the polymerization  
233 of the murein monomers and is facilitated by a family of enzymes called transpeptidases. The four primary  
234 transpeptidases of *E. coli* have only recently been quantitatively characterized *in vivo* via liquid chromatography  
235 mass spectrometry which revealed a notably slow kinetic turnover rate of  $\approx 2$  crosslinking reactions formed per  
236 second per enzyme (*Catherwood et al., 2020*).

237 Assembling these quantities permits us to make an estimate that on the order of  $\approx 100$  transpeptidases per cell  
238 are needed for complete maturation of the peptidoglycan, given a division time of  $\approx 5000$  seconds; a value that is  
239 comparable to experimental observations (*Figure 3(B)*). Expanding this estimate to account for the changing mass  
240 of the peptidoglycan as a function of growth rate (grey line in *Figure 3(B)*) also qualitatively captures the observed  
241 dependence in the data, though systematic disagreements between the different data sets makes the comparison  
242 more difficult.

## 243 Limits on Cell Wall Biogenesis

244 While the processes we have considered represent only a small portion of proteins devoted to cell envelope  
245 biogenesis, we find it unlikely that they limit cellular growth in general. The relative amount of mass required  
246 for lipid and peptidoglycan components decrease at faster growth rates due to a decrease in their surface area  
247 to volume (S/V) ratio (*Ojkic et al., 2019*). Furthermore, despite the slow catalytic rate of FabZ and FabA in lipid  
248 synthesis, experimental data and recent computational modeling has shown that the rate of fatty-acid synthesis  
249 can be drastically increased by increasing the concentration of FabZ (*Yu et al., 2011; Ruppe and Fox, 2018*). With  
250 a proteome size of  $\approx 3 \times 10^6$  proteins, a hypothetical 10-fold increase in expression from 4000 to 40,000 ACP  
251 dehydratases would result in a paltry  $\approx 1\%$  increase in the size of the proteome. In the context of peptidoglycan  
252 synthesis, we note that our estimate considers only the transpeptidase enzymes that are involved lateral and  
253 longitudinal elongation of the peptidoglycan. This neglects the presence of other transpeptidases that are present  
254 in the periplasm and also involved in remodeling and maturation of the peptidoglycan. It is therefore possible that  
255 if this was setting the speed limit for cell division, the simple expression of more transpeptidases may be sufficient  
256 to maintain the structural integrity of the cell wall.

## 257 Energy Production

258 Cells consume and generate energy predominantly in the form of nucleoside triphosphates (NTPs) in order to  
259 grow. The high-energy phosphodiester bonds of (primarily) ATP power a variety of cellular processes that drive

## CELL ENVELOPE BIOSYNTHESIS

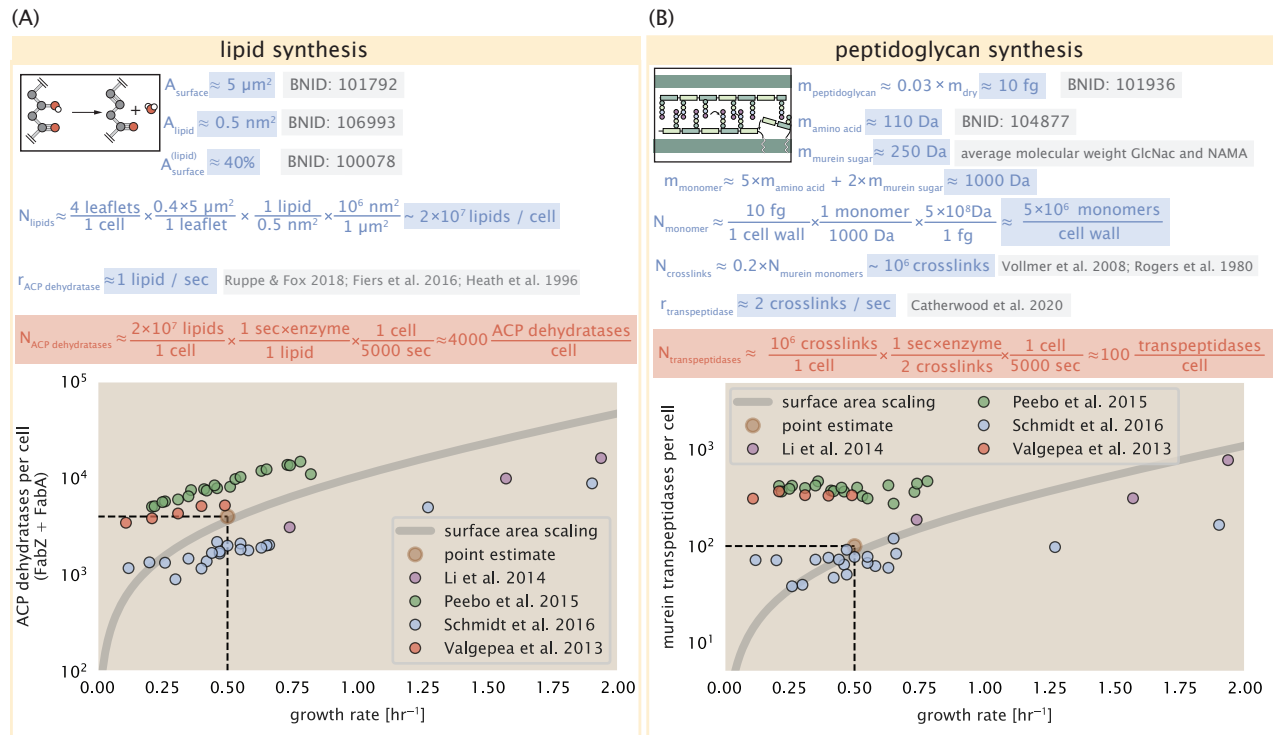


**Figure 3.** (A) Top panel shows an estimation for the number of ACP dehydratases necessary to form functional phospholipids, which is assumed to be a rate-limiting step on lipid synthesis. The rate of ACP dehydratases was inferred from experimental measurements via a stochastic kinetic model described in [Ruppe and Fox \(2018\)](#). Bottom panel shows the experimentally observed complex copy numbers using the stoichiometries  $[\text{FabA}]_2$  and  $[\text{FabZ}]_2$ . (B) An estimate for the number of peptidoglycan transpeptidases needed to complete maturation of the peptidoglycan. The mass of the murein monomer was estimated by approximating each amino acid in the pentapeptide chain as having a mass of 110 Da and each sugar in the disaccharide having a mass of 250 Da. The *in vivo* rate of transpeptidation in *E. coli* was taken from recent analysis by [Catherwood et al. \(2020\)](#). The bottom panel shows experimental measurements of the transpeptidase complexes in *E. coli* following the stoichiometries  $[\text{MrcA}]_2$ ,  $[\text{MrcB}]_2$ ,  $[\text{MrdA}]_1$ , and  $[\text{MrdB}]_1$ . Grey curves in each plot show the estimated number of complexes needed to satisfy the synthesis requirements scaled by the surface area as a function of growth rate.

260 biological systems away from thermodynamic equilibrium. We next turn to the synthesis of ATP as a potential  
261 process that may limit growth, which also requires us to consider the maintenance of the electrochemical proton  
262 gradient which powers it.

263 **ATP Synthesis**

264 Hydrolysis of the terminal phosphodiester bond of ATP into ADP (or alternatively GTP and GDP) and an inorganic  
265 phosphate provides the thermodynamic driving force in a wide array of biochemical reactions. One such reaction  
266 is the formation of peptide bonds during translation, which requires  $\approx 2$  ATPs for the charging of an amino acid  
267 to the tRNA and  $\approx 2$  GTP for the formation of each peptide bond. Assuming the ATP costs associated with error  
268 correction and post-translational modifications of proteins are negligible, we can make the approximation that each  
269 peptide bond has a net cost of  $\approx 4$  ATP (BNID: 101442, *Milo et al. (2010)*). Formation of GTP from ATP is achieved  
270 via the action of nucleoside diphosphate kinase, which catalyzes this reaction without an energy investment  
271 (*Lascu and Gonin, 2000*) and therefore consider all NTP requirements of the cell to be functionally equivalent to  
272 being exclusively ATP. In total, the energetic costs of peptide bond formation consume  $\approx 80\%$  of the cells ATP  
273 budget (BNID: 107782; 106158; 101637; 111918, *Lynch and Marinov (2015); Stouthamer (1973)*). The pool of ATP is  
274 produced by the F<sub>1</sub>-F<sub>0</sub> ATP synthase – a membrane-bound rotary motor which under ideal conditions can yield  $\approx$   
275 300 ATP per second (BNID: 114701; *Weber and Senior (2003)*).

276 To estimate the total number of ATP equivalents consumed during a cell cycle, we will make the approximation  
277 that there are  $\approx 3 \times 10^6$  proteins per cell with an average protein length of  $\approx 300$  peptide bonds (BNID: 115702;  
278 108986; 104877). Taking these values together, coupled with an estimate of  $\approx 4$  ATP equivalents per peptide bond,  
279 we find that the typical *E. coli* cell consumes  $\sim 5 \times 10^9$  ATP per cell cycle on protein synthesis alone. Assuming  
280 that each ATP synthases operates at its maximal speed (300 ATP per second per synthase),  $\approx 3000$  ATP synthases  
281 are needed to keep up with the energy demands of the cell. This estimate is comparable with the experimental  
282 observations, shown in *Figure 4* (A). We note that this estimate assumes all ATP is synthesized via ATP synthase  
283 and neglects synthesis via fermentative metabolism. This assumption may explain why at the fastest growth rates  
284 ( $\approx 2$  hr<sup>-1</sup>), our continuum estimate predicts more synthase than is experimentally observed (gray line in *Figure 4*).  
285 At rapid growth rates, *E. coli* enters a type of overflow metabolism where fermentative metabolism becomes  
286 pronounced (*Szenk et al., 2017*).

287 **Generating the Proton Electrochemical Gradient**

288 In order to produce ATP, the F<sub>1</sub>-F<sub>0</sub> ATP synthase itself must consume energy. Rather than burning through its  
289 own product (and violating thermodynamics), this intricate macromolecular machine has evolved to exploit the  
290 electrochemical potential established across the inner membrane through cellular respiration. This electrochemical  
291 gradient is manifest by the pumping of protons into the intermembrane space via the electron transport chains as  
292 they reduce NADH. In *E. coli*, this potential difference is  $\approx -200$  mV (BNID: 102120). A simple estimate of the inner  
293 membrane as a capacitor with a working voltage of -200 mV reveals that  $\approx 2 \times 10^4$  protons must be present in the  
294 intermembrane space. However, each rotation of an ATP synthase shuttles  $\approx 4$  protons into the cytosol (BNID:  
295 103390). With a few thousand ATP synthases producing ATP at their maximal rate, the potential difference would  
296 be rapidly abolished in a few milliseconds if it were not being actively maintained.

297 The electrochemistry of the electron transport complexes of *E. coli* have been the subject of intense biochemical  
298 and biophysical study (*Ingledew and Poole, 1984; Khademian and Imlay, 2017; Cox et al., 1970; Henkel et al., 2014*).  
299 A recent work (*Szenk et al., 2017*) examined the respiratory capacity of the *E. coli* electron transport complexes  
300 using structural and biochemical data, revealing that each electron transport chain rapidly pumps protons into the  
301 intermembrane space at a rate of  $\approx 1500$  protons per second (BIND: 114704; 114687). Using our estimate of the  
302 number of ATP synthases required per cell [*Figure 4(A)*], coupled with these recent measurements, we estimate  
303 that  $\approx 3000$  electron transport complexes would be necessary to facilitate the  $\sim 5 \times 10^6$  protons per second diet of  
304 the cellular ATP synthases. This estimate is in agreement with the number of complexes identified in the proteomic  
305 datasets (plot in *Figure 4(B)*). This suggests that every ATP synthase must be accompanied by  $\approx 1$  functional electron  
306 transport chain.

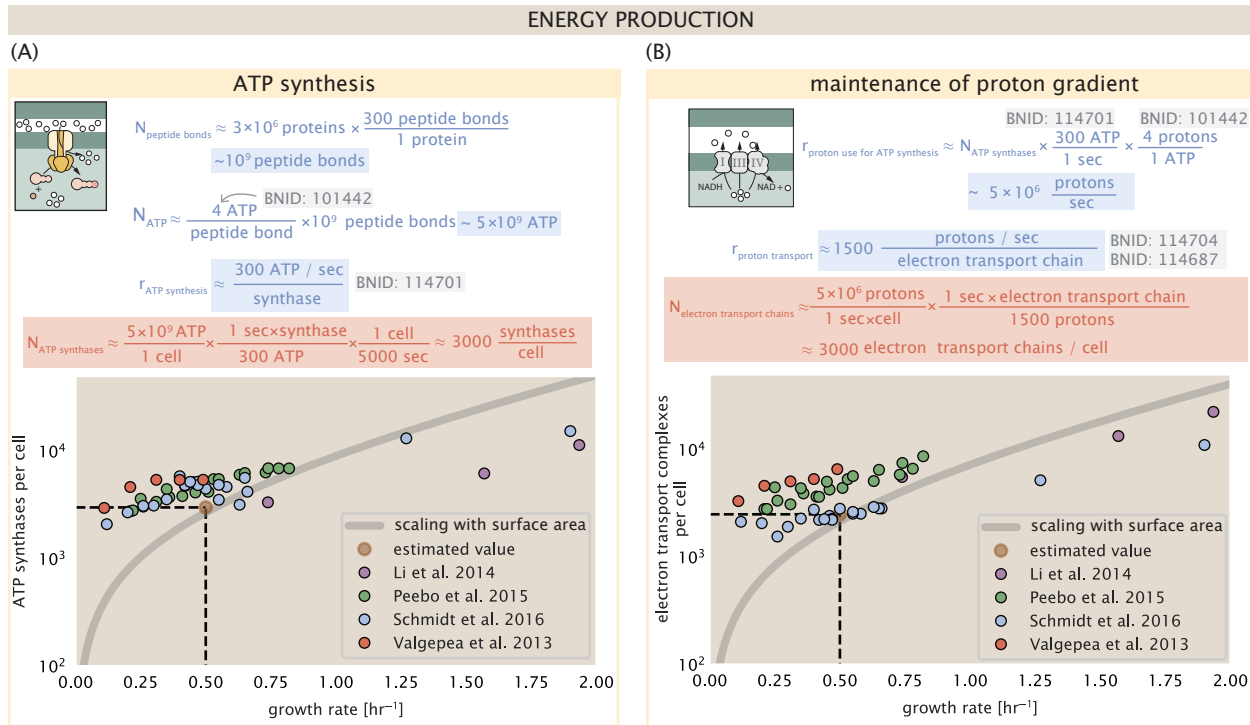


**Figure 4. The abundance of F<sub>1</sub>-F<sub>0</sub> ATP synthases and electron transport chain complexes as a function of growth rate.**

(A) Estimate of the number of F<sub>1</sub>-F<sub>0</sub> ATP synthase complexes needed to accommodate peptide bond formation and other NTP dependent processes. Points in plot correspond to the mean number of complete F<sub>1</sub>-F<sub>0</sub> ATP synthase complexes that can be formed given proteomic measurements and the subunit stoichiometry [AtpE]<sub>10</sub>[AtpF]<sub>2</sub>[AtpB][AtpC][AtpH][AtpA]<sub>3</sub>[AtpG][AtpD]<sub>3</sub>. (B) Estimate of the number of electron transport chain complexes needed to maintain a membrane potential of -200 mV given estimate of number of F<sub>1</sub>-F<sub>0</sub> ATP synthases from (A). Points in plot correspond to the average number of complexes identified as being involved in aerobic respiration by the Gene Ontology identifier GO:0019646 that could be formed given proteomic observations. These complexes include cytochromes *bd1* ([CydA][CydB][CydX][CydH]), *bdII* ([AppC][AppB]), *bo<sub>3</sub>*,([CyoD][CyoA][CyoB][CyoC]) and NADH:quinone oxioreductase I ([NuoA][NuoH][NuoJ][NuoK][NuoL][NuoM][NuoN][NuoB][NuoC][NuoE][NuoF][NuoG][NuoI]) and II ([Ndh]). Grey lines in both (A) and (B) correspond to the estimate procedure described, but applied to a continuum of growth rates. We direct the reader to the Supporting Information for a more thorough description of this approach.

307 Limits on Biosynthesis in a Crowded Membrane

308 Our estimates thus far have focused on biochemistry at the periphery of the cell and have generally been  
309 concordant with the abundances predicted by our estimates. However, as surface area and volume do not scale  
310 identically, it is necessary to consider the physical limits for transport and energy production given the S/V ratio,  
311 which as we've noted will decrease at faster growth rates.

312 In our estimate of ATP production above we found that a cell demands about  $5 \times 10^9$  ATP per cell cycle or  $10^6$   
313 ATP/s. With a cell volume of roughly 1 fL (BNID: 100004), this corresponds to about  $2 \times 10^{10}$  ATP per fL of cell volume,  
314 in line with previous estimates (*Stouthamer and Bettenhausen, 1977; Szenk et al., 2017*). In **Figure 5 (A)** we plot  
315 this ATP demand as a function of the S/V ratio in green, where we have considered a range of cell shapes from  
316 spherical to rod-shaped with an aspect ratio (length/width) equal to 4. In order to consider the maximum ATP that  
317 could be produced, we consider the amount of ATP that can be generated by a membrane filled with ATP synthase  
318 and electron transport complexes, which provides a maximal production of about 3 ATP / (nm<sup>2</sup>·s) (*Szenk et al.,*  
319 *2017*). This is shown in blue in **Figure 5(A)**, which shows that at least for the growth rates observed (right column  
320 in plot), the energy demand is roughly an order of magnitude less. Interestingly, *Szenk et al. (2017)* also found  
321 that ATP production by respiration is less efficient than by fermentation per membrane area occupied due to the  
322 additional proteins of the electron transport chain. This suggests that, even under anaerobic growth, there will be  
323 sufficient membrane space for ATP production.

324 The analysis highlights the diminishing capacity to provide resources as the cell increases in size. However,  
325 the maximum energy production in **Figure 5(A)** does represent a somewhat unachievable limit since the inner  
326 membrane must also include other proteins including those required for lipid and membrane synthesis. To  
327 better understand the overall proteomic makeup of the inner membrane, we therefore used Gene Ontology (GO)  
328 annotations (*Ashburner et al., 2000; The Gene Ontology Consortium, 2018*) to identify all proteins embedded or  
329 peripheral to the inner membrane (GO term: 0005886). Those associated but not membrane-bound include  
330 proteins like MreB and FtsZ and must nonetheless be considered as a vital component occupying space on the  
331 membrane. In **Figure 5(B)**, we find that the total protein mass per  $\mu\text{m}^2$  is nearly constant across growth rates.  
332 Interestingly, when we consider the distribution of proteins grouped by their Clusters of Orthologous Groups (COG)  
333 (*Tatusov et al., 2000*), the relative abundance for those in metabolism (including ATP synthesis via respiration) is  
334 also relatively constant across growth rates, suggesting that no one process (energy production, nutrient uptake,  
335 etc.) is particularly dominating even at fast growth rates **Figure 5(C)**.

336 **Processes of the Central Dogma**

337 Up to this point, we have considered a variety of transport and biosynthetic processes that are critical to acquiring  
338 and generating new cell mass. While there are of course many other metabolic processes we could consider, we  
339 now turn our focus to some of the most central processes which *must* be undertaken irrespective of the growth  
340 conditions – those of the central dogma.

341 **DNA Replication**

342 Most bacteria (including *E. coli*) harbor a single, circular chromosome and can have extra-chromosomal plasmids  
343 up to  $\sim 100$  kbp in length. While we consider the starting material dNTPs in **Figure 6-Figure Supplement 1** and  
344 discussed further in Appendix Additional Process of the Central Dogma, here we focus our quantitative thinking on  
345 the chromosome of *E. coli* which harbors  $\approx 5000$  genes and  $\approx 5 \times 10^6$  base pairs.

346 To successfully divide and produce viable progeny, this chromosome must be faithfully replicated and seg-  
347 regated into each nascent cell. Replication is initiated at a single region of the chromosome termed the *oriC*  
348 locus at which a pair of replisomes, each consisting of two DNA polymerase III, begin their high-fidelity replication  
349 of the genome in opposite directions (*Fijalkowska et al., 2012*). *In vitro* measurements have shown that DNA  
350 Polymerase III copies DNA at a rate of  $\approx 600$  nucleotides per second (BNID: 104120). Therefore, to replicate a single  
351 chromosome, two replisomes moving at their maximal rate would copy the entire genome in  $\approx 4000$  s. Thus, with  
352 a division time of 5000 s, there is sufficient time for a pair of replisomes complexes to replicate the entire genome.

353 In rapidly growing cultures, bacteria like *E. coli* can initiate as many as 10 - 12 replication forks at a given time  
354 (*Bremer and Dennis, 2008; Si et al., 2017*), we expect only a few DNA polymerases ( $\approx 10$ ) are needed. However, as

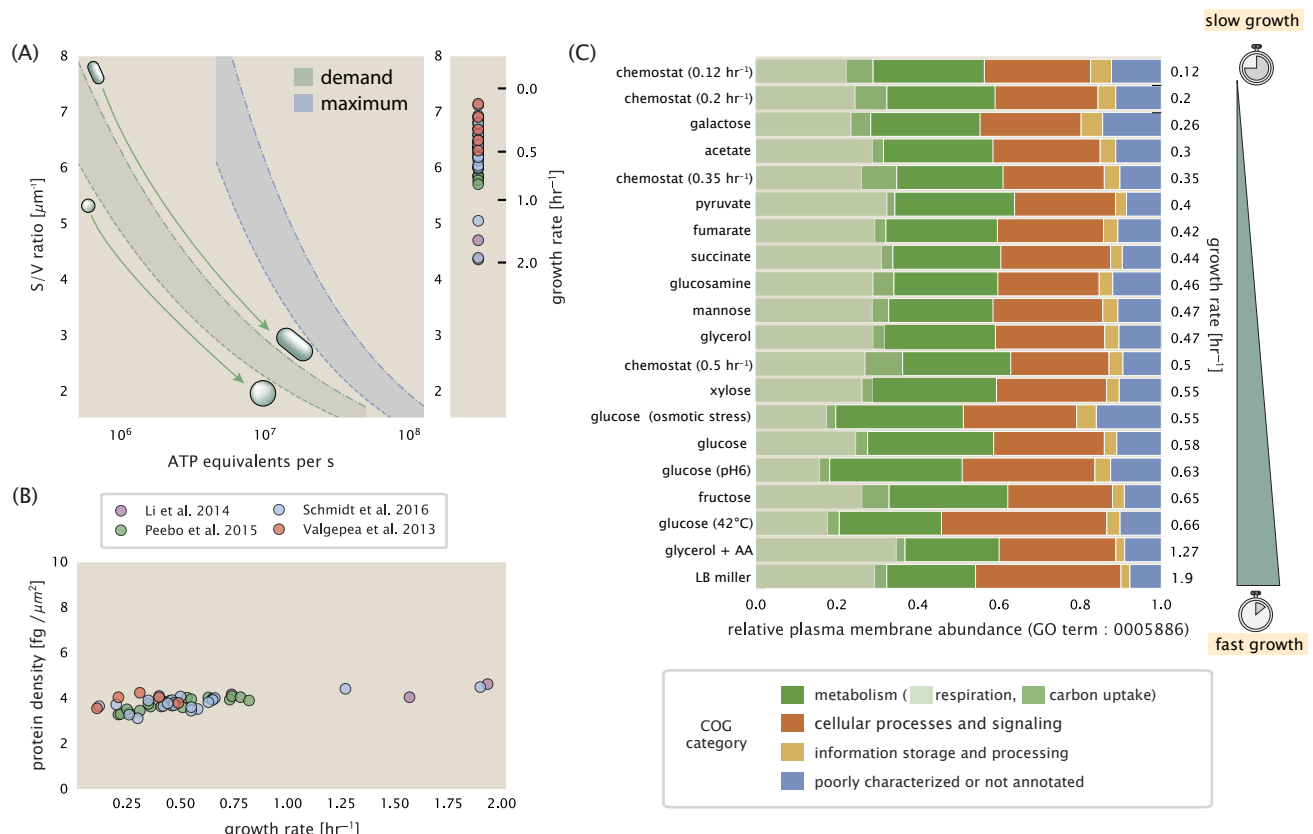


**Figure 5. Influence of cell size and S/V ratio on ATP production and inner membrane composition.** (A) Scaling of ATP demand and maximum ATP production as a function of S/V ratio. Cell volumes of 0.5 fL to 50 fL were considered, with the dashed (—) line corresponding to a sphere and the dash-dot line (---) reflecting a rod-shaped bacterium like *E. coli* with a typical aspect ratio (length / width) of 4 (Shi et al., 2018). Approximately 50% of the bacterial inner membrane is assumed to be protein, with the remainder lipid. The right plot shows the measured growth rates, and their estimated S/V ratio using growth rate dependent size measurements from Si et al. (2017) (See Appendix Estimation of Cell Size and Surface Area on calculation). (B) Total protein mass per  $\mu\text{m}^2$  calculated for proteins with inner membrane annotation (GO term: 0005886). (C) Relative protein abundances by mass based on COG annotation. Metabolic proteins are further separated into respiration (F<sub>1</sub>-F<sub>0</sub> ATP synthase, NADH dehydrogenase I, succinate:quinone oxidoreductase, cytochrome bo<sub>3</sub> ubiquinol oxidase, cytochrome bd-I ubiquinol oxidase) and carbohydrate transport (GO term: GO:0008643). Note that the elongation factor EF-Tu can also associate with the inner membrane, but was excluded in this analysis due to its high relative abundance (roughly identical to the summed protein shown in part (B)).

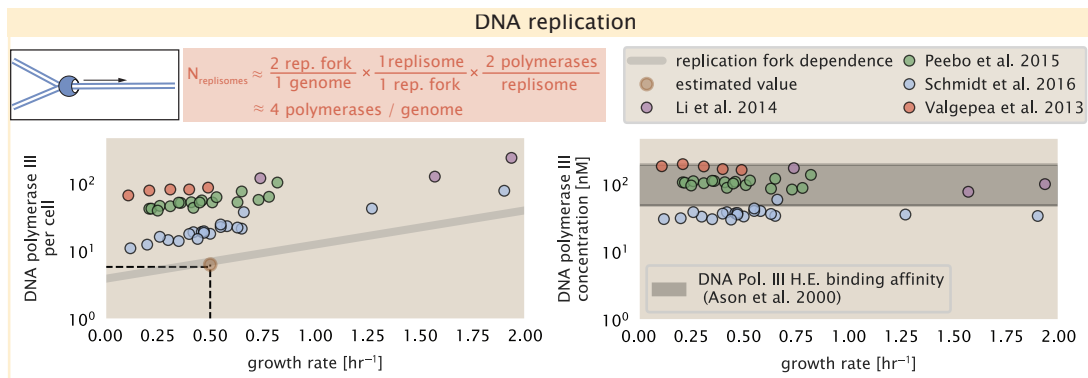


**Figure 6. Complex abundance estimates for dNTP synthesis and DNA replication.** An estimate for the minimum number of DNA polymerase holoenzyme complexes needed to facilitate replication of a single genome. Points in the left-hand plot correspond to the total number of DNA polymerase III holoenzyme complexes ( $[DnaE]_3[DnaQ]_3[HolE]_3[DnaX]_5[HolB][HolA][DnaN]_4[HolC]_4[HolD]_4$ ) per cell. Right-hand plot shows the effective concentration of DNA polymerase III holoenzyme (See Appendix Estimation of Cell Size and Surface Area for calculation of cell size). Grey lines in left-hand panel show the estimated number of complexes needed as a function of growth, the details of which are described in the Supplemental Information.

**Figure 6-Figure supplement 1.** Estimate and observations of the abundance of ribonucleotide reductase, a key component in dNTP synthesis.

355 shown in **Figure 6** DNA polymerase III is nearly an order of magnitude more abundant. This discrepancy can be  
 356 understood by considering its binding constant to DNA. *In vitro* characterization has quantified the  $K_D$  of DNA  
 357 polymerase III holoenzyme to single-stranded and double-stranded DNA to be 50 and 200 nM, respectively (Ason  
 358 et al., 2000). The right-hand plot in **Figure 6** shows that the concentration of DNA polymerase III across all data  
 359 sets is within this range. Thus, its copy number appears to vary such that its concentration is approximately  
 360 equal to the dissociation constant to the DNA. While the processes regulating the initiation of DNA replication are  
 361 complex and involve more than just the holoenzyme, these data indicate that the kinetics of replication rather than  
 362 the explicit copy number of the DNA polymerase III holoenzyme is the more relevant feature of DNA replication  
 363 to consider. In light of this, the data in **Figure 6** suggests that for bacteria like *E. coli*, DNA replication does not  
 364 represent a rate-limiting step in cell division. However, it is worth noting that for bacterium like *C. crescentus*  
 365 whose chromosomal replication is initiated only once per cell cycle (Jensen et al., 2001), the time to double their  
 366 chromosome indeed represents an upper limit to their growth rate.

### 367 RNA Synthesis

368 We now turn our attention to the next stage of the central dogma – the transcription of DNA to form RNA. We  
 369 consider three major groupings of RNA, namely the RNA associated with ribosomes (rRNA), the RNA encoding the  
 370 amino-acid sequence of proteins (mRNA), and the RNA which links codon sequence to amino-acid identity during  
 371 translation (tRNA).

372 rRNA serves as the catalytic and structural component of the ribosome, comprising approximately 2/3 of the  
 373 total ribosomal mass, and is decorated with  $\approx 50$  ribosomal proteins. Each ribosome contains three rRNA molecules  
 374 of lengths 120, 1542, and 2904 nucleotides (BNID: 108093), meaning each ribosome contains  $\approx 4500$  nucleotides  
 375 overall. *In vivo* measurements of the kinetics of rRNA transcription have revealed that RNA polymerases are loaded  
 376 onto the promoter of an rRNA gene at a rate of  $\approx 1$  per second (BNID: 111997, 102362). If RNA polymerases are  
 377 constantly loaded at this rate, then we can assume that  $\approx 1$  functional rRNA unit is synthesized per second per  
 378 rRNA operon. While *E. coli* possesses 7 of these operons per chromosome, the fact that chromosome replication  
 379 can be parallelized means that the average dosage of rRNA genes can be substantially higher (up to  $\approx 70$  copies) at  
 380 fast growth rates. At a growth rate of  $\approx 0.5 \text{ hr}^{-1}$ , however, the average cell has  $\approx 1$  copy of its chromosome and  
 381 therefore approximately  $\approx 7$  copies of the rRNA operons, therefore producing  $\approx 7$  rRNA units per second. With a  
 382 5000 second division time, this means the cell is able to generate around  $3 \times 10^4$  functional rRNA units, comparable  
 383 within an order of magnitude to the number of ribosomes per cell.

384 How many RNA polymerases are then needed to constantly transcribe the required rRNA? If one polymerase is  
385 loaded per second, and the transcription rate is  $\approx$  40 nucleotides per second (BNID: 101094), then the typical  
386 spacing between polymerases will be  $\approx$  40 nucleotides. However, we must note that the polymerase itself has a  
387 footprint of  $\approx$  40 nucleotides (BNID: 107873), meaning that one could expect to find one RNA polymerase per 80  
388 nucleotide stretch of an rRNA gene. With a total length of  $\approx$  4500 nucleotides per operon and 7 operons per cell,  
389 the number of RNA polymerases transcribing rRNA at any given time is then  $\approx$  500 per cell.

390 As outlined in **Figure 7**, and discussed further the Appendix Additional Process of the Central Dogma, synthesis  
391 of mRNA and tRNA together require on the order of  $\approx$  400 RNAP. Thus, in total, one would expect the typical  
392 cell to require  $\approx$  1000 RNAP to satisfy its transcriptional demands. As is revealed in **Figure 7(B)**, this estimate  
393 is about an order of magnitude below the observed number of RNA polymerase complexes per cell ( $\approx$  5000 -  
394 7000). The difference between the estimated number of RNA polymerase needed for transcription and these  
395 observations, however, are consistent with recent literature revealing that  $\approx$  80 % of RNA polymerases in *E. coli* are  
396 not transcriptionally active (**Patrick et al., 2015**).

397 Our estimates also neglect other mechanistic features of transcription and transcriptional initiation more  
398 broadly. For example, we acknowledge that some fraction of the RNAP pool is nonspecifically bound to DNA  
399 during its search for promoters from which to begin transcription. Furthermore, we ignore the obstacles that RNA  
400 polymerase and DNA polymerase present to each other as they move along the DNA (**Finkelstein and Greene,**  
401 **2013**). Finally, we neglect the fact that RNA polymerase also require  $\sigma$ -factors for promoter recognition and  
402 transcription initiation (**Browning and Busby, 2016**).

403 While they are the machinery for transcription, RNA polymerase is not sufficient to initiate transcription.  
404 Promoter recognition and initiation of transcription is dependent on the presence of  $\sigma$ -factors, protein cofactors  
405 which bind directly to the polymerase (**Browning and Busby, 2016**). In **Figure 7–Figure Supplement 1**, we show that  
406 the predicted RNA polymerase copy number indeed is more comparable with the abundance of  $\sigma$ -70 (RpoD), the  
407 primary sigma factor in *E. coli*. There therefore remains more to be investigated as to what sets the observed  
408 abundance of RNA polymerase in these proteomic data sets. However, we conclude that our the observed excess  
409 in abundance for RNA polymerase abundances are generally in excess of what appears to be needed for growth,  
410 suggesting that the abundance of RNA polymerase itself is not particularly limiting.

## 411 Protein Synthesis

412 We conclude our dialogue between back-of-the-envelope estimates and comparison with the proteomic data by  
413 examining the final process in the central dogma – translation. In doing so, we will begin with an estimate of the  
414 number of ribosomes needed to replicate the cellular proteome. While the rate at which ribosomes translate is  
415 well known to be dependent on the growth rate (**Dai et al. (2018)**, a phenomenon we consider later in this work) we  
416 will make the approximation that translation occurs at a modest rate of  $\approx$  15 amino acids per second per ribosome  
417 (BNID: 100233) Under this approximation and our previous estimate of  $10^9$  peptide bonds per cell at a growth rate  
418 of  $0.5 \text{ hr}^{-1}$ , we can easily arrive at an estimate of  $\approx 10^4$  ribosomes needed per cell to replicate the entire protein  
419 mass (**Figure 8(A)**, top). This point estimate, as well as the corresponding estimate across a continuum of growth  
420 rates, proves to be notably comparable to the experimental observations, shown in the bottom panel of **Figure 8(A)**.  
421 While the ribosome is responsible for the formation of peptide bonds, we do not diminish the importance of  
422 charging tRNAs with their appropriate amino acid, a process with occurs with remarkable fidelity. In the Appendix  
423 and in **Figure 8–Figure Supplement 1**, we consider the process of ligating tRNAs to their corresponding amino acid  
424 and again find notable accord between the data and our quantitative expectations.

425 Having completed our circuit through key processes of cellular growth outlined in **Figure 1**, we can now take stock  
426 of our understanding of the observed growth rate dependence and abundances of various protein complexes. We  
427 note that, broadly speaking, these simple estimates have been reasonably successful in quantitatively describing  
428 the observations in the proteomic data, suggesting that the proteome is tuned in composition and absolute  
429 abundance to match the growth rate requirements without any one process representing a singular bottleneck or  
430 rate limiting step in division. However, in our effort to identify key limitations on growth, there are two notable  
431 observations that we wish to emphasize.

432 The first is a recurring theme throughout our estimates. Of those investigated here, any inherent biochemical  
433 rate limitation can be overcome by expressing more proteins. We can view this as a parallelization of each

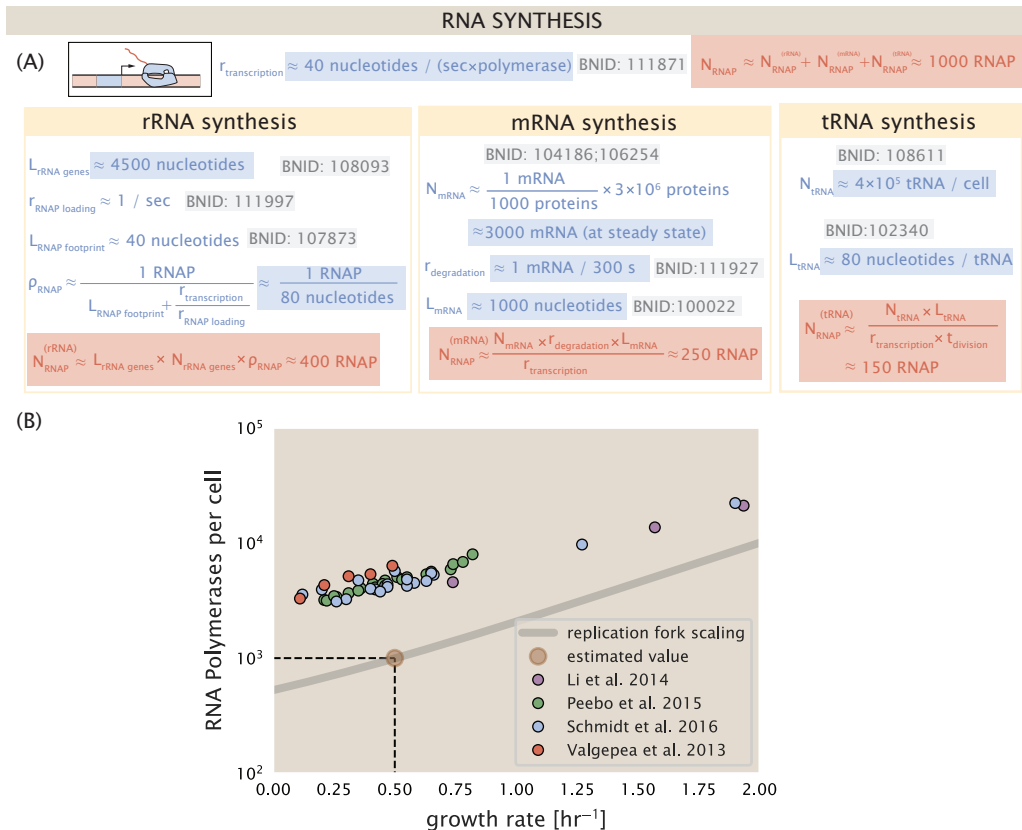


**Figure 7. Estimation of the RNA polymerase demand and comparison with experimental data.** (A) Estimations for the number of RNA polymerase needed to synthesize sufficient quantities of rRNA, mRNA, and tRNA from left to right, respectively.(B) The RNA polymerase core enzyme copy number as a function of growth rate. Colored points correspond to the average number RNA polymerase core enzymes that could be formed given a subunit stoichiometry of  $[RpoA]_2[RpoC][RpoB]$ .

**Figure 7-Figure supplement 1.** Abundance and growth rate dependence of  $\sigma$ -70.

434 biosynthesis task, which helps explain why bacteria tend to increase their protein content (and cell size) as growth  
435 rate increases (*Ojkic et al., 2019*). The second, and ultimately the most significant in defining the cellular growth  
436 rate, is that the synthesis of ribosomal proteins presents a special case where parallelization is *not* possible and  
437 thereby imposes a limit on the fastest possible growth rate. Each ribosome has  $\approx$  7500 amino acids across all of its  
438 protein components which must be strung together as peptide bonds through the action of another ribosome.  
439 Once again using a modest elongation rate of  $\approx$  15 amino acids per second, we arrive at an estimate of  $\approx$  500 seconds  
440 or  $\approx$  7 minutes to replicate a single ribosome. This limit, as remarked upon by others (*Dill et al., 2011*), serves as a  
441 hard theoretical boundary for how quickly *E. coli* could replicate. As each ribosome would therefore need to copy  
442 itself, this 7 minute speed limit is independent of the number of ribosomes per cell (*Figure 8(B)*), yet assumes that  
443 the only proteins that need to be replicated for division to occur are ribosomal proteins, an unrealistic regime not  
444 met in biological reality. This poses an optimization problem for the cell – how are the translational demands of  
445 the entire proteome met without investing resources in the production of an excess of ribosomes?

446 This question, more frequently presented as a question of optimal resource allocation, has been the target of  
447 an extensive dialogue between experiment and theory over the past decade. In a now seminal work, *Scott et al.*  
448 (*2010*) present an elegant treatment of resource allocation through partitioning of the proteome into sectors – one  
449 of which being ribosome-associated proteins whose relative size ultimately defines the total cellular growth rate. In  
450 more recent years, this view has been more thoroughly dissected experimentally (*Klumpp and Hwa, 2014; Basan*  
451 *et al., 2015; Dai et al., 2018, 2016; Erickson et al., 2017*) and together have led to a paradigm-shift in how we think  
452 of cellular physiology at the proteomic-level. However, the quantitative description of these observations is often  
453 couched in terms of phenomenological constants and effective parameters with the key observable features of  
454 expression often computed in relative, rather than absolute, abundances. Furthermore, these approaches often  
455 exclude or integrate away effects of cell size and chromosome content, which we have found through our estimates  
456 to have important connections to the observed cellular growth rate.

457 In the closing sections of this work, we explore how ribosomal content, total protein abundance, and chromo-  
458 somal replication are intertwined in their control over the cellular growth rate. To do so, we take a more careful  
459 view of ribosome abundance, increasing the sophistication of our analysis by exchanging our order-of-magnitude  
460 estimates for a minimal mathematical model of growth rate control. This is defined by parameters with tangible  
461 connections to the biological processes underlying cellular growth and protein synthesis. Using this model, we  
462 interrogate how the size of the ribosome pool and its corresponding translational capacity enable cells to maintain  
463 a balance between the consumption of amino acids via metabolism and catabolism and their consumption through the peptide  
464 bond formation required for growth.

## 465 Maximum Growth Rate is Determined by the Ribosomal Mass Fraction

466 The 7 minute speed limit shown in *Figure 8(B)* assumes all proteins in the cell are ribosomes. In order to connect  
467 this to the experimental data (and physiological reality more broadly), we first need to relax this assumption and  
468 determine a translation-limited growth rate. Here, we will assume that the cell is composed of  $N_{\text{pep}}$  peptide bonds  
469 and  $R$  ribosomes, whose precise values will depend on the growth rate  $\lambda$ . The protein subunits of each ribosomal  
470 protein sum to a total of  $\approx$  7500 amino acids as noted earlier, which we denote by  $L_R$ . With an average mass of an  
471 amino acid of  $m_{\text{AA}} \approx 110$  Da (BNID: 104877), the total ribosomal mass fraction  $\Phi_R$  is given by

$$\Phi_R = \frac{m_{\text{ribosomes}}}{m_{\text{proteome}}} \approx \frac{m_{\text{AA}} \times R \times L_R}{m_{\text{AA}} \times N_{\text{pep}}} = \frac{R \times L_R}{N_{\text{pep}}}. \quad (1)$$

472 For exponentially growing cells (*Godin et al., 2010*), the rate of cellular growth will be related to the rate of protein  
473 synthesis via

$$\lambda N_{\text{pep}} = r_t \times R \times f_a, \quad (2)$$

474 where  $r_t$  is the translation rate. Here, we've introduced a multiplicative factor  $f_a$  which represents the fraction of the  
475 ribosomes that are actively translating. This term allows us to account for immature or non-functional ribosomes  
476 or active sequestration of ribosomes through the action of the secondary messenger alarmone (p)ppGpp in poorer  
477 nutrient conditions (*Hauryliuk et al. (2015)*).

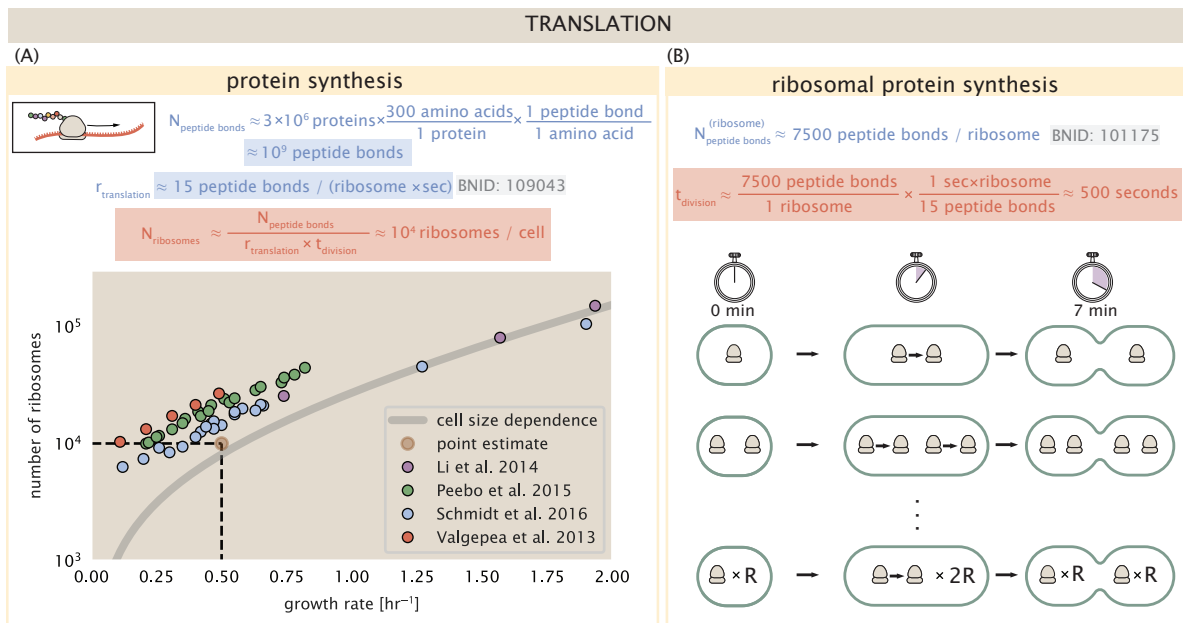


**Figure 8. Estimation of the required number of ribosomes and the speed limit for bacterial replication.** (A) Estimation of the number of ribosomes required to synthesize  $10^9$  peptide bonds with an elongation rate of 15 peptide bonds per second. The average abundance of ribosomes is plotted as a function of growth rate. Our estimated values are shown for a growth rate of  $0.5 \text{ hr}^{-1}$ . Grey lines correspond to the estimated complex abundance calculated at different growth rates. (B) Estimation for the time to replicate a ribosome. This rate is independent of the number of ribosomes  $R$  and instead is limited by the time required to double an individual ribosome.

**Figure 8—Figure supplement 1.** Estimate and observed abundance and growth rate dependence of tRNA ligases.

478 Combining **Equation 1** and **Equation 2** results in an expression for a translation-limited growth rate, which is  
479 given by

$$\lambda_{\text{translation-limited}} = \frac{r_i \times \Phi_R \times f_a}{L_R}. \quad (3)$$

480 This result, derived in a similar manner in *Klumpp et al. (2013)*, reflects mass-balance under steady state growth  
481 and has long provided a rationalization of the apparent linear increase in *E. coli*'s ribosomal content as a function  
482 of growth rate (*Maaløe, 1979; Dennis et al., 2004; Scott et al., 2010*). The left-hand panel of **Figure 9(A)** shows this  
483 growth rate plotted as a function of the ribosomal mass fraction. In the regime where all ribosomes are active  
484 ( $f_a = 1$ ) and the entire proteome is composed of ribosomal proteins ( $\Phi_R = 1$ ), indeed, we arrive at the maximum  
485 theoretical growth rate of  $r_i/L_R$ , and  $\approx 7 \text{ min}$  for *E. coli*.

486 Connecting **Equation 3** to the proteomic data serving as the centerpiece of our work, however, requires  
487 knowledge of  $f_a$  at each growth rate as proteomic measurements only provide a measure of  $\Phi_R$ . Recently, *Dai et al.*  
488 (2016) determined  $f_a$  as a function of the growth rate (**Figure 9(A)**, right-hand panel, inset), revealing that  $f_a \approx 1$  at  
489 growth rates above  $0.75 \text{ hr}^{-1}$  and  $f_a < 1$  as the growth rate slows. Using these data, we inferred the approximate  
490 active fraction (see Appendix Calculation of active ribosomal fraction) at each growth rate and used this to compute  
491  $\Phi_R \times f_a$  (**Figure 9(A)**, colored points in right-hand panel). In general, these data skirt the translation-limited growth  
492 rate determined using **Equation 3** with  $r_i$  taken to be the maximal elongation rate of 17 amino acids per second  
493 measured by *Dai et al. (2016)*. There is a notable discrepancy between the data collected in *Schmidt et al. (2016)*;  
494 *Li et al. (2014)* and that collected from *Valgepea et al. (2013); Peebo et al. (2015)*. When compared to other  
495 measurements (non-proteomic with significantly lower resolution) of the active ribosome mass fraction (**Figure 9(B)**,  
496 grey points in right-hand panel), the data from *Valgepea et al. (2013)* and *Peebo et al. (2015)* are notably aberrant,  
497 suggesting a systematic error in these data. These additional measurements come from a number of recent studies  
498 and are determined from measurements of total RNA to total protein mass ratios (**Figure 9—Figure Supplement 1**).

499 Together, these results illustrate that the growth rates observed across the amalgamated data sets are close to  
500 the translation-limited growth rate determined through their ribosomal activity, at least for the data reported in

501 Schmidt et al. (2016) and Li et al. (2014). While this is a useful framework to consider how the relative abundance of  
502 ribosomes (compared to all other proteins) defines the growth rate, it is worth noting that as growth rate increases,  
503 so does the cell size and therefore so will the total proteomic mass (Basan et al., 2015). With a handle on how  
504 elongation rate and the total number of peptide bonds per proteome is related to the growth rate, we now expand  
505 this description to account for the increasing cell size and ribosome copy number at faster growth rates, enabling  
506 us to identify a potential bottleneck in the synthesis of rRNA.

### 507 rRNA Synthesis Presents a Potential Bottleneck During Rapid Growth

508 Even under idealized experimental conditions, *E. coli* rarely exhibits growth rates above  $2 \text{ hr}^{-1}$  (Bremer and Dennis,  
509 2008), which is still well-below the synthesis rate of a single ribosome, and below the maximum growth rates  
510 reported for several other bacteria (Roller et al., 2016). While we have considered potential limits imposed by  
511 translation of ribosomal proteins, here we consider potential limiting regimes for the production of rRNA.

512 Due to multiple initiations of chromosomal replication per cell doubling, the effective number of rRNA operons  
513 increases with growth rate and will do so in proportion to the average number of origins per cell,  $\langle \# \text{ ori} \rangle$ . This later  
514 parameter is set by how often replication must be initiated in order to keep up with cell doubling times  $\tau$  whose  
515 time may be shorter than the cell cycle time  $t_{\text{cyc}}$  (referring to the time from replication initiation to cell division)  
516 Dennis et al. (2004). This is quantified by

$$\langle \# \text{ ori} \rangle = 2^{\tau_{\text{cyc}}/\tau} = 2^{\tau_{\text{cyc}}\lambda/\log(2)}. \quad (4)$$

517 We used the experimental measurements of  $\tau_{\text{cyc}}$  (the timescale of chromosome replication and cell division) and  $\tau$   
518 (the timescale of a cell doubling) from Si et al. (2017) (Figure 9–Figure Supplement 1(B)) to calculate  $\langle \# \text{ ori} \rangle$  with  
519 Equation 4 as a function of growth rates. For growth rates above about  $0.5 \text{ hr}^{-1}$ ,  $t_{\text{cyc}}$  is approximately constant  
520 at about 70 minutes, implying that  $\langle \# \text{ ori} \rangle$  will grow exponentially with growth rates beyond  $0.5 \text{ hr}^{-1}$ . As the  
521 rRNA operons are predominantly located close to origin of replication (BNID: 100352), we make the simplifying  
522 assumption that that the number of rRNA operons will be directly proportional to  $\langle \# \text{ ori} \rangle$ .

523 Returning to our rule-of-thumb of 1 functional rRNA unit per second per transcribing operon, we estimate the  
524 maximum number of ribosomes that could be made as a function of growth rate (Figure 9(B), blue curve). Although  
525 we expect this estimate to significantly overestimate rRNA abundance at slower growth rates ( $\lambda < 0.5 \text{ hr}^{-1}$ ), this  
526 provides a useful reference alongside the proteomic measurements particularly in the regime of fast growth. For  
527 growth rates above about  $1 \text{ hr}^{-1}$ , for example, we find that cells will need to transcribe rRNA near their maximal  
528 rate. As a counter example, if *E. coli* did not initiate multiple rounds of replication, but managed to replicate their  
529 chromosome within the requisite time limit, they would be unable to make enough rRNA for the observed number  
530 of ribosomes (dashed blue curve in Figure 9(C)). The convergence between the maximum rRNA production and  
531 measured ribosome copy number suggests rRNA synthesis may begin to present a bottleneck at the fastest growth  
532 rates due to the still-limited copies of rRNA genes.

### 533 Rapid Growth Requires *E. coli* to Increase Both Cell Size and Ribosomal Mass Fraction

534 In Figure 9(B, right-hand side) we find that above about  $0.75 \text{ hr}^{-1}$ , the growth rate is determined by the ribosomal  
535 mass fraction  $\Phi_R$ , since  $f_a$  is close to 1, and  $r_i$  is near its maximal rate (Dai et al., 2016). While  $\Phi_R$  will need to  
536 increase in order for cells to grow faster, the fractional dependence in Equation 3 gives little insight into how this is  
537 actually achieved in the cell.

538 It is now well-documented that *E. coli* cells add a constant volume per origin of replication, which is robust  
539 to a remarkable array of cellular perturbations (Si et al., 2017). Given the proteomic measurements featured in  
540 this work, it becomes apparent that the ribosome copy number is also scaled in proportion to  $\langle \# \text{ ori} \rangle$  Figure 10(A).  
541 Importantly, however, it will only be due to an increase in  $\Phi_R$  at these moderate to fast growth rates that cells  
542 can achieve an increase in their growth rate. Indeed, we find that the deviations in protein expression with  $\langle \# \text{ ori} \rangle$   
543 are largely restricted to regions of ribosomal protein genes Figure 10(B). Here we have calculated the position-  
544 dependent protein expression across the chromosome by a running Gaussian average of protein copy number (20  
545 kbp st. dev. averaging window) based on each gene's transcriptional start site. These were median-subtracted to  
546 account for the change in total protein abundance with  $\langle \# \text{ ori} \rangle$ . This result suggests that  $\Phi_R$  is also being tuned in

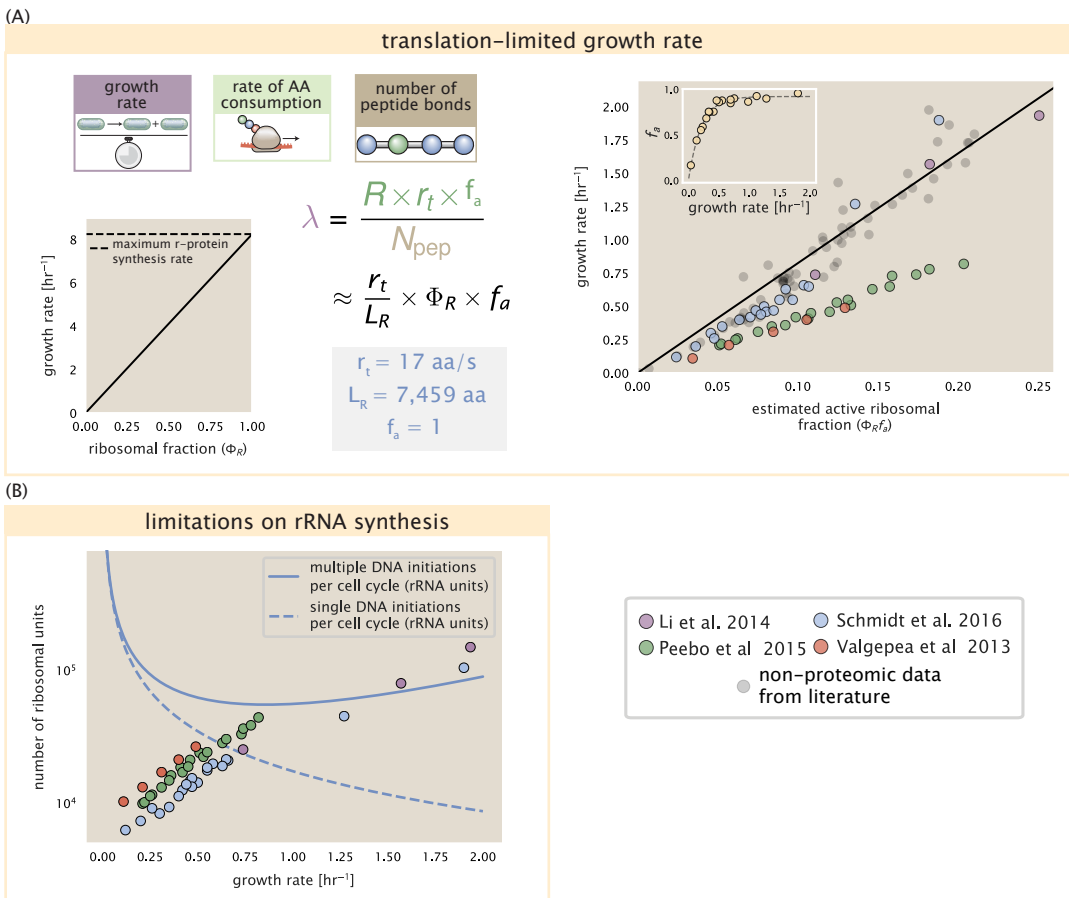


**Figure 9. Translation-limited growth rate.** (A) *left*: Translation-limited growth as a function of the ribosomal fraction. The solid line is calculated for an elongation rate of 17 aa per second. The dashed line corresponds to the maximum rate of ribosomal protein synthesis ( $\approx 7$  min). *right*: Translation-limited growth rate as a function of the actively translating ribosomal fraction. The actively translating ribosomal fraction is calculated using the estimated values of  $f_a$  from [Dai et al. \(2016\)](#) (shown in inset; see Appendix Calculation of active ribosomal fraction for additional detail). Gray data points show additional measurements from literature and consider further in the supplemental figure part (A). (B) Maximum number of rRNA units that can be synthesized as a function of growth rate. Solid curve corresponding to the rRNA copy number is calculated by multiplying the number of rRNA operons by the estimated number of (# ori) at each growth rate. The quantity (# ori) was calculated using Equation 4 and the measurements from [Si et al. \(2017\)](#). The dashed line shows the maximal number of functional rRNA units produced from a single chromosomal initiation per cell cycle.

**Figure 9–Figure supplement 1.** Comparison of  $\Phi_R f_a$  with literature and estimation of (# ori).

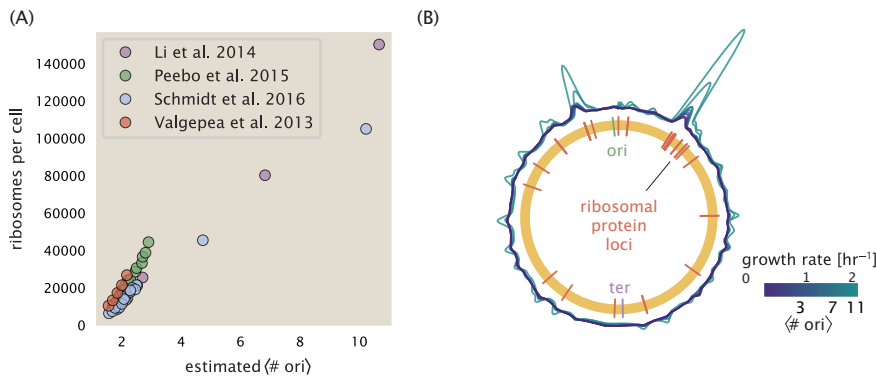


**Figure 10. Cells increase both absolute ribosome abundance and  $\Phi_R$  with (# ori).** (A) Plot of the ribosome copy number estimated from the proteomic data against the estimated (# ori) (see Appendix Estimation of  $\langle \# \text{ori} \rangle / \langle \# \text{ter} \rangle$  and  $\langle \# \text{ori} \rangle$  for additional details). (B) A running Gaussian average (20 kbp st. dev.) of protein copy number is calculated for each growth condition considered by (Schmidt et al., 2016) based on each gene's transcriptional start site. Since total protein abundance increases with growth rate, protein copy numbers are median-subtracted to allow comparison between growth conditions. (# ori) are estimated using the data in (A) and Equation 4.

547 proportion to (# ori) under nutrient-limited growth, and in particular, it is through this additional dependence on  
548  $\Phi_R$  that *E. coli* exhibits an exponential increase in cell size with growth rate.

#### 549 A Minimal Model of Nutrient-Mediated Growth Rate Control

550 While the preceding subsections highlight a dominant role for ribosomes in setting the growth rate, our analysis on  
551 the whole emphasizes that the total proteomic content must also change in response to variable growth conditions  
552 and growth rate. In this final section we use a minimal model of growth rate control to better understand how this  
553 interconnection between ribosomal abundance and total protein influences the observed growth rate.

554 Here we propose that cells modulate their protein abundance in direct response to the availability of nutrients  
555 in their environment. As noted earlier, bacteria can modulate ribosomal activity through the secondary-messenger  
556 molecules like (p)ppGpp in poorer nutrient conditions (Figure 9(C) - inset; Dai et al. (2016)). Importantly, these  
557 secondary-messengers also cause global changes in transcriptional and translational activity (Hauryliuk et al.,  
558 2015; Zhu and Dai, 2019; Büke et al., 2020). In *E. coli*, amino acid starvation leads to the accumulation of de-acylated  
559 tRNAs at the ribosome's A-site and a strong increase in (p)ppGpp synthesis activity by the enzyme RelA (Hauryliuk  
560 et al., 2015). Along with this, there is increasing evidence that (p)ppGpp also acts to inhibit the initiation of DNA  
561 replication (Kraemer et al., 2019), providing a potential mechanism to lower (# ori) and maintain a smaller cell size  
562 in poorer growth conditions (Fernández-Coll et al., 2020).

563 To consider this quantitatively, we assume that cells modulate their proteome ( $N_{\text{pep}}$ ,  $R$ ,  $\Phi_R$ ) to better maximize  
564 their rate of peptide elongation  $r_t$ . The elongation rate  $r_t$  will depend on how quickly the ribosomes can match  
565 codons with their correct amino-acyl tRNA, along with the subsequent steps of peptide bond formation and  
566 translocation. This ultimately depends on the cellular concentration of amino acids, which we treat as a single  
567 effective species,  $[AA]_{\text{eff}}$ . In our model, we determine the the rate of peptide elongation  $r_t$  and achievable growth  
568 rate as simply depending on the supply of amino acids (and, therefore, also amino-acyl tRNAs), through a parameter  
569  $r_{AA}$  in units of AA per second, and the rate of amino acid consumption by protein synthesis ( $r_t \times R \times f_a$ ). This is  
570 shown schematically in Figure 11(A) and derived in Appendix ???. Given our observation that protein synthesis  
571 and energy production are not limiting, we assume that other molecular players required by ribosomes such as  
572 elongation factors and GTP are available in sufficient abundance.

573 In Figure 11(B), we illustrate how the elongation rate will depend on the ribosomal copy number. Here, we  
574 have considered an arbitrarily chosen  $r_{AA} = 5 \times 10^6 \text{ AA} \cdot \text{s}^{-1} \cdot \mu\text{m}^{-3}$  and  $f_a = 1$  for a unit cell volume  $V = 1 \text{ fL}$ . At  
575 low ribosome copy numbers, the observed elongation rate is dependent primarily on  $[AA]_{\text{eff}}$  through  $r_{AA}$  [as  
576  $r_t^{\max} \times R \times f_a \ll r_{AA}$ , point (1) in Figure 11(B)]. As the ribosome copy number is increased such that the amino acid  
577 supply rate and consumption rate are nearly equal [point (2) in Figure 11(B)], the observed elongation rate begins

(A)

## A MINIMAL MODEL FOR NUTRIENT-LIMITED GROWTH

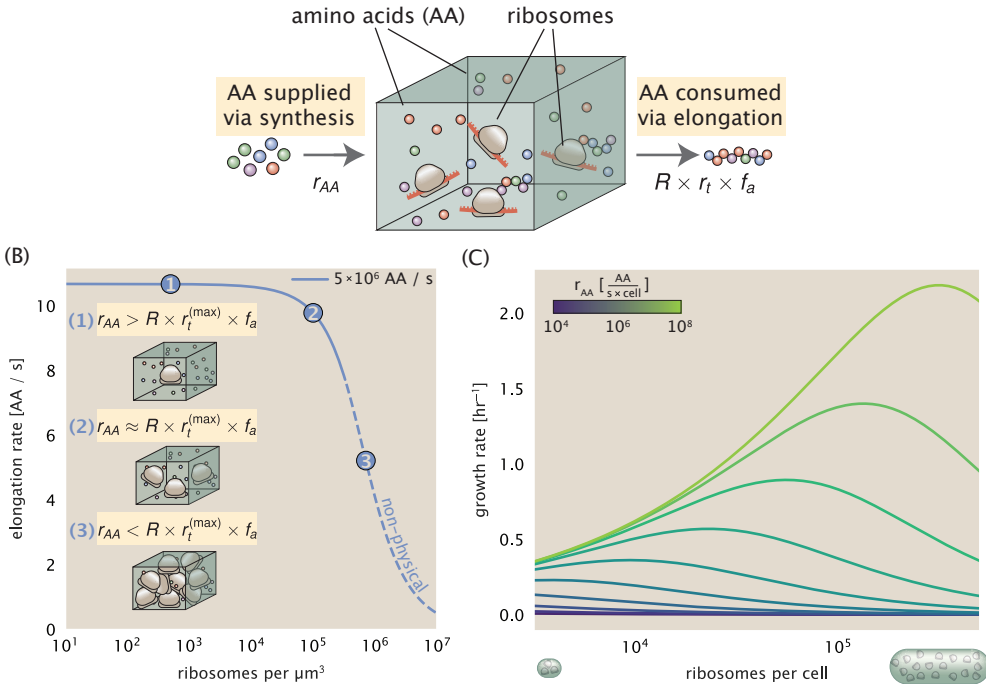


**Figure 11. A minimal model of growth rate control under nutrient limitation.** (A) We consider a unit volume of cellular material composed of amino acids (colored spheres) provided at a supply rate  $r_{AA}$ . These amino acids are polymerized by a pool of ribosomes (brown blobs) at a rate  $r_t \times R \times f_a$ , where  $r_t$  is the elongation rate,  $R$  is the ribosome copy number in the unit volume, and  $f_a$  is the fraction of those ribosomes actively translating. (B) The observed elongation rate is plotted as a function of ribosomes. The three points correspond to three regimes of ribosome copy numbers and are shown schematically on the left-hand side. The region of the curve shown as dashed lines represents a non-physical copy number, but is shown for illustrative purposes. This curve was generated using an amino acid supply rate of  $5 \times 10^6 \text{ AA / s}$ , a maximal elongation rate of  $17.1 \text{ AA / s}$ ,  $f_a = 1$ , and a unit cell volume of  $V = 1 \text{ fL}$ . See Appendix ?? for additional model details. (C) The cellular growth rate is plotted as a function of total cellular ribosome copy number for different cellular amino acid supply rates, with blue and green curves corresponding to low and high supply rates, respectively. As the ribosome copy number is increased, so too is the cell size and total protein abundance  $N_{\text{pep}}$ . We direct the reader to the Supplemental Information for discussion on the inference of the relationship between cell size, number of peptide bonds, and ribosome copy number.

**Figure 11–Figure supplement 1.** An interactive figure for exploration of the model parameter space.

578 to decrease sharply. When the ribosome copy number is increased even further, consumption at the maximum  
579 elongation rate exceeds the supply rate, yielding a significantly reduced elongation rate [point (3) in **Figure 11B**].  
580 While the elongation rate will always be dominated by the amino acid supply rate at sufficiently low ribosome  
581 copy numbers, the elongation rate at larger ribosome abundances can be increased by tuning  $f_a$  such that not all  
582 ribosomes are elongating, reducing the total consumption rate.

583 Optimal Ribosomal Content and Cell Size Depend on Nutrient Availability and Metabolic Capacity  
584 To relate elongation rate to growth rate, we constrain the set of parameters based on our available proteomic  
585 measurements; namely, we restrict the values of  $R$ ,  $N_{\text{pep}}$ , and cell size to those associated with the amalgamated  
586 proteomic data (described in Appendix Estimation of Total Protein Content per Cell). We then consider how changes  
587 in the nutrient conditions, through the parameter  $r_{AA}$ , influence the maximum growth rate as determined by ??.  
588 **Figure 11(C)** shows how the observed growth rate depends on the rate of amino acid supply  $r_{AA}$  as a function of  
589 the cellular ribosome copy number. A feature immediately apparent is the presence of a maximal growth rate  
590 whose dependence on  $R$  (and consequently, the cell size) increases with increasing  $r_{AA}$ . Importantly, however,  
591 there is an optimum set of  $R$ ,  $N_{\text{pep}}$ , and  $V$  that are strictly dependent on the value of  $r_{AA}$ . Increasing the ribosomal  
592 concentration beyond the cell's metabolic capacity has the adverse consequence of depleting the supply of amino  
593 acids and a concomitant decrease in the elongation rate  $r_t$  [**Figure 11(B)**].

Also of note is the growth rate profiles shown for low amino acid supply rates [purple and blue lines in **Figure 11(C)**], representing growth in nutrient-poor media. In these conditions, there no longer exists a peak in growth, at least in the range of physiologically-relevant ribosome copy numbers. Instead, cells limit their pool of actively translating ribosomes by decreasing  $f_a$  ([Dai et al., 2016](#)), which would help maintain the pool of available amino acids  $[AA]_{\text{eff}}$  and increase the achievable elongation rate. This observation is in agreement with the central premise of the cellular resource allocation principle proposed by [Scott et al. \(2010\)](#); [Klumpp et al. \(2009\)](#); [Klumpp and Hwa \(2014\)](#) and [Hui et al. \(2015\)](#).

## Discussion

Continued experimental and technological improvements have led to a treasure trove of quantitative biological data ([Hui et al., 2015](#); [Schmidt et al., 2016](#); [Si et al., 2017](#); [Gallagher et al., 2020](#); [Peebo et al., 2015](#); [Valgepea et al., 2013](#)), and an ever advancing molecular view and mechanistic understanding of the constituents that support bacterial growth ([Taheri-Araghi et al., 2015](#); [Morgenstern et al., 2015](#); [Si et al., 2019](#); [Karr et al., 2012](#); [Kostinski and Reuveni, 2020](#)). In this work we have compiled what we believe to be the state-of-the-art knowledge on proteomic copy number across a broad range of growth conditions in *E. coli*. We have made this data accessible through a [GitHub repository](#), and an [interactive figure](#) that allows exploration of specific protein and protein complex copy numbers. Through a series of order-of-magnitude estimates that traverse key steps in the bacterial cell cycle, this proteomic data has been a resource to guide our understanding of two key questions: what biological processes limit the absolute speed limit of bacterial growth, and how do cells alter their molecular constituents as a function of changes in growth rate or nutrient availability? While not exhaustive, our series of estimates provide insight on the scales of macromolecular complex abundance across four classes of cellular processes – the transport of nutrients, the production of energy, the synthesis of the membrane and cell wall, and the numerous steps of the central dogma.

In general, the copy numbers of the complexes involved in these processes were in reasonable agreement with our order-of-magnitude estimates. Since many of these estimates represent soft lower-bound quantities, this suggests that cells do not express proteins grossly in excess of what is needed for a particular growth rate. Several exceptions, however, also highlight the dichotomy between a proteome that appears to "optimize" expression according to growth rate and one that must be able to quickly adapt to environments of different nutritional quality. Take, for example, the expression of carbon transporters. Shown in **Figure 2(B)**, we find that cells always express a similar number of glucose transporters irrespective of growth condition. At the same time, it is interesting to note that many of the alternative carbon transporters are still expressed in low but non-zero numbers ( $\approx 10\text{-}100$  copies per cell) across growth conditions. This may relate to the regulatory configuration for many of these operons, which require the presence of a metabolite signal in order for alternative carbon utilization operons to be induced ([Monod, 1949](#); [Laxhuber et al., 2020](#)). Furthermore, upon induction, these transporters are expressed and present in abundances in close agreement with a simple estimate.

Of the processes illustrated in **Figure 1**, we arrive at a ribosome-centric view of cellular growth rate control. This is in some sense unsurprising given the long-held observation that *E. coli* and many other organisms vary their ribosomal abundance as a function of growth conditions and growth rate ([Scott et al., 2010](#); [Metzl-Raz et al., 2017](#)). However, through our dialogue with the proteomic data, two additional key points emerge. The first relates to our question of what process sets the absolute speed limit of bacterial growth. While a cell can parallelize many of its processes simply by increasing the abundance of specific proteins or firing multiple rounds of DNA replication, this is not so for synthesis of ribosomes (**Figure 9(A)**). The translation time for each ribosome [ $\approx 7$  min, [Dill et al. \(2011\)](#)] places an inherent limit on the growth rate that can only be surpassed if the cell were to increase their polypeptide elongation rate, or if they could reduce the total protein and rRNA mass of the ribosome. The second point relates to the long-observed correlations between growth rate and cell size ([Schaechter et al., 1958](#); [Si et al., 2017](#)), and between growth rate and ribosomal mass fraction. While both trends have sparked tremendous curiosity and driven substantial amounts of research in their own regards, these relationships are themselves intertwined. In particular, it is the need for cells to increase their absolute number of ribosomes under conditions of rapid growth that require cells to also grow in size. Further experiments are needed to test the validity of this hypothesis. In particular, we believe that the change in growth rate in response to translation-inhibitory drugs (such as chloramphenicol) could be quantitatively predicted, given one had precision measurement of the relevant

644 parameters, including the fraction of actively translating ribosomes  $f_a$  and changes in the metabolic capacity of the  
645 cell (i.e. the rate of amino acid supply) for a particular growth condition.

646 While the generation of new ribosomes plays a dominant role in growth rate control, there exist other physical  
647 limits to the function of cellular processes. One of the key motivations for considering energy production was  
648 the physical constraints on total volume and surface area as cells vary their size (**Harris and Theriot, 2018; Ojkic**  
649 **et al., 2019**). While *E. coli* get larger as it expresses more ribosomes, an additional constraint begins to arise in  
650 energy production due to a relative decrease in total surface area where ATP is predominantly produced (**Szenk**  
651 **et al., 2017**). Specifically, the cell interior requires an amount of energy that scales cubically with cell size, but the  
652 available surface area only grows quadratically (**Figure 5(A)**). While this threshold does not appear to be met for  
653 *E. coli* cells growing at 2 hr<sup>-1</sup> or less, it highlights an additional constraint on growth given the apparent need to  
654 increase in cell size to grow faster. This limit is relevant even to eukaryotic organisms, whose mitochondria exhibit  
655 convoluted membrane structures that nevertheless remain bacteria-sized organelles (**Guo et al., 2018**). In the  
656 context of bacterial growth and energy production more generally, we have limited our analysis to the aerobic  
657 growth conditions associated with the proteomic data and further consideration will be needed for anaerobic  
658 growth.

659 This work is by no means meant to be an exhaustive dissection of bacterial growth rate control, and there are  
660 many aspects of the bacterial proteome and growth that we neglected to consider. For example, other recent work  
661 (**Liebermeister et al., 2014; Hui et al., 2015; Schmidt et al., 2016**) has explored how the proteome is structured  
662 and how that structure depends on growth rate. In the work of **Hui et al. (2015)**, the authors coarse-grained the  
663 proteome into six discrete categories being related to either translation, catabolism, anabolism, and others related  
664 to signaling and core metabolism. The relative mass fraction of the proteome occupied by each sector could be  
665 modulated by external application of drugs or simply by changing the nutritional content of the medium. While  
666 we have explored how the quantities of individual complexes are related to cell growth, we acknowledge that  
667 higher-order interactions between groups of complexes or metabolic networks at a systems-level may reveal  
668 additional insights into how these growth-rate dependences are mechanistically achieved. Furthermore, while we  
669 anticipate the conclusions summarized here are applicable to a wide collection of bacteria with similar lifestyles as *E.*  
670 *coli*, other bacteria and archaea may have evolved other strategies that were not considered. Further experiments  
671 with the level of rigor now possible in *E. coli* will need to be performed in a variety of microbial organisms to learn  
672 more about how regulation of proteomic composition and growth rate control has evolved over the past 3.5 billion  
673 years.

## 674 Methods

### 675 Data Analysis and Availability

676 All proteomic measurements come from the experimental work of **Schmidt et al. (2016); Peebo et al. (2015);**  
677 **Valgepea et al. (2013)** (mass spectrometry) and **Li et al. (2014)** (ribosomal profiling). Data curation and analysis was  
678 done programmatically in Python, and compiled data and analysis files are accessible through a [GitHub repository]  
679 (DOI:XXX) associated with this paper as well as on the associated [paper website](#). An interactive figure that allows  
680 exploration of specific protein and protein complex copy numbers is available at [link].

### 681 Acknowledgements

682 We thank Matthias Heinemann, Alexander Schmidt, and Gene-Wei Li for additional input regarding their data. We  
683 also thank members of the Phillips, Theriot, Kondev, and Garcia labs for useful discussions. We thank Suzannah M.  
684 Beeler, Avi Flamholz, Soichi Hirokawa, and Manuel Razo-Mejia for reading and providing comments on drafts of this  
685 manuscript. R.P. is supported by La Fondation Pierre-Gilles de Gennes, the Rosen Center at Caltech, and the NIH  
686 1R35 GM118043 (MRA). J.A.T. is supported by the Howard Hughes Medical Institute, and NIH Grant R37-AI036929.  
687 N.M.B is a HHMI Fellow of The Jane Coffin Childs Memorial Fund.

### 688 Competing Interests

689 The authors declare no competing interests.

690 **Appendix for: Fundamental limits on the**  
691 **rate of bacterial cell division**

692 **Nathan M. Belliveau<sup>†, 1</sup>, Griffin Chure<sup>†, 2</sup>, Christina L. Hueschen<sup>3</sup>, Hernan G. Garcia<sup>4</sup>, Jane**  
693 **Kondev<sup>5</sup>, Daniel S. Fisher<sup>6</sup>, Julie A. Theriot<sup>1, 7, \*</sup>, Rob Phillips<sup>8, 9, \*</sup>**

694 <sup>1</sup>Department of Biology, University of Washington, Seattle, WA, USA; <sup>2</sup>Department of Applied Physics,  
695 California Institute of Technology, Pasadena, CA, USA; <sup>3</sup>Department of Chemical Engineering, Stanford  
696 University, Stanford, CA, USA; <sup>4</sup>Department of Molecular Cell Biology and Department of Physics,  
697 University of California Berkeley, Berkeley, CA, USA; <sup>5</sup>Department of Physics, Brandeis University,  
698 Waltham, MA, USA; <sup>6</sup>Department of Applied Physics, Stanford University, Stanford, CA, USA; <sup>7</sup>Allen  
699 Institute for Cell Science, Seattle, WA, USA; <sup>8</sup>Division of Biology and Biological Engineering, California  
700 Institute of Technology, Pasadena, CA, USA; <sup>9</sup>Department of Physics, California Institute of Technology,  
701 Pasadena, CA, USA; \*Co-corresponding authors. Address correspondence to phillips@pboc.caltech.edu  
702 and jtheriot@uw.edu; <sup>†</sup>These authors contributed equally to this work

<b>703</b>	<b>Contents</b>	
<b>704</b>	<b>Introduction</b>	<b>1</b>
<b>705</b>	<b>Nutrient Transport</b>	<b>2</b>
706	Limits on Transporter Expression . . . . .	6
<b>707</b>	<b>Cell Envelope Biogenesis</b>	<b>6</b>
708	Lipid Synthesis . . . . .	6
709	Peptidoglycan Synthesis . . . . .	7
710	Limits on Cell Wall Biogenesis . . . . .	7
<b>711</b>	<b>Energy Production</b>	<b>7</b>
712	ATP Synthesis . . . . .	9
713	Generating the Proton Electrochemical Gradient . . . . .	9
714	Limits on Biosynthesis in a Crowded Membrane . . . . .	11
<b>715</b>	<b>Processes of the Central Dogma</b>	<b>11</b>
716	DNA Replication . . . . .	11
717	RNA Synthesis . . . . .	13
718	Protein Synthesis . . . . .	14
719	Maximum Growth Rate is Determined by the Ribosomal Mass Fraction . . . . .	16
720	rRNA Synthesis Presents a Potential Bottleneck During Rapid Growth . . . . .	18
721	Rapid Growth Requires <i>E. coli</i> to Increase Both Cell Size and Ribosomal Mass Fraction . . . . .	18
<b>722</b>	<b>A Minimal Model of Nutrient-Mediated Growth Rate Control</b>	<b>20</b>
723	Optimal Ribosomal Content and Cell Size Depend on Nutrient Availability and Metabolic Capacity . . . . .	21
<b>724</b>	<b>Discussion</b>	<b>22</b>
<b>725</b>	<b>Methods</b>	<b>23</b>
726	Data Analysis and Availability . . . . .	23
<b>727</b>	<b>Acknowledgements</b>	<b>23</b>
<b>728</b>	<b>Competing Interests</b>	<b>23</b>
<b>729</b>	<b>Additional Estimates of Fundamental Biological Processes</b>	<b>27</b>
730	Nutrient Transport . . . . .	27
731	Nitrogen . . . . .	27
732	Phosphorus . . . . .	27
733	Sulfur . . . . .	27
734	Additional Process of the Central Dogma . . . . .	28
735	dNTP synthesis . . . . .	28
736	mRNA and tRNA Synthesis . . . . .	28
737	tRNA Charging . . . . .	29
<b>738</b>	<b>Experimental Details Behind Proteomic Data</b>	<b>30</b>
739	Fluorescence based measurements . . . . .	30
740	Ribosomal profiling measurements . . . . .	31
741	Mass spectrometry measurements . . . . .	31
<b>742</b>	<b>Summary of Proteomic Data</b>	<b>31</b>
<b>743</b>	<b>Estimation of Cell Size and Surface Area</b>	<b>32</b>

744	<b>Estimation of Total Protein Content per Cell</b>	<b>33</b>
745	Estimating Volume and Number of Amino Acids from Ribosome Copy Number . . . . .	34
746	<b>Additional Considerations of Schmidt <i>et al.</i> Data Set</b>	<b>34</b>
747	Effect of cell volume on reported absolute protein abundances . . . . .	38
748	Relaxing assumption of constant protein concentration across growth conditions . . . . .	38
749	Comparison with total protein measurements from Basan <i>et al.</i> 2015. . . . .	38
750	<b>Calculation of Complex Abundance</b>	<b>39</b>
751	<b>Extending Estimates to a Continuum of Growth Rates</b>	<b>40</b>
752	Estimation of the total cell mass . . . . .	40
753	Complex Abundance Scaling With Cell Volume . . . . .	42
754	A Relation for Complex Abundance Scaling With Surface Area . . . . .	43
755	Number of Lipids . . . . .	43
756	Number of Murein Monomers . . . . .	43
757	Complex Abundance Scaling With Number of Origins, and rRNA Synthesis . . . . .	43
758	<b>Calculation of active ribosomal fraction.</b>	<b>44</b>
759	<b>Estimation of <math>\langle \#ori \rangle / \langle \#ter \rangle</math> and <math>\langle \#ori \rangle</math>.</b>	<b>44</b>

760 **Additional Estimates of Fundamental Biological Processes**

761 In the main text of this work, we present estimates for a significant number of fundamental biological processes  
762 that are necessary for cell division. While we believe the estimates provided in the main text provide a succinct  
763 summary of the corresponding process, we left out additional estimates of related processes for brevity. In this  
764 section of the appendix, we present these additional estimates in full.

765 **Nutrient Transport**

766 In the main text, we make passing mention that while transport carbon often comes in the form of carbohydrates  
767 and sugar alcohols while other critical elements – such as nitrogen, sulfur, and phosphorus – are transported as  
768 inorganic ions. Below, we present estimates for the transport requirements of these materials.

769 **Nitrogen**

770 We must first address which elemental sources must require active transport, meaning that the cell cannot acquire  
771 appreciable amounts simply via diffusion across the membrane. The permeability of the lipid membrane to a large  
772 number of solutes has been extensively characterized over the past century. Large, polar molecular species (such  
773 as various sugar molecules, sulfate, and phosphate) have low permeabilities while small, non-polar compounds  
774 (such as oxygen, carbon dioxide, and ammonia) can readily diffuse across the membrane. Ammonia, a primary  
775 source of nitrogen in typical laboratory conditions, has a permeability on par with water ( $\sim 10^5$  nm/s, BNID:110824).  
776 In nitrogen-poor conditions, *E. coli* expresses a transporter (AmtB) which appears to aid in nitrogen assimilation,  
777 though the mechanism and kinetic details of transport are still a matter of debate (*van Heeswijk et al., 2013*;  
778 *Khademi et al., 2004*). Beyond ammonia, another plentiful source of nitrogen come in the form of glutamate,  
779 which has its own complex metabolism and scavenging pathways. However, nitrogen is plentiful in the growth  
780 conditions examined in this work, permitting us to neglect nitrogen transport as a potential rate limiting process in  
781 cell division in typical experimental conditions.

782 **Phosphorus**

783 Phosphorus is critical to the cellular energy economy in the form of high-energy phosphodiester bonds making up  
784 DNA, RNA, and the NTP energy pool as well as playing a critical role in the post-translational modification of proteins  
785 and defining the polar-heads of lipids. In total, phosphorus makes up  $\approx 3\%$  of the cellular dry mass which in typical  
786 experimental conditions is in the form of inorganic phosphate. The cell membrane has remarkably low permeability  
787 to this highly-charged and critical molecule, therefore requiring the expression of active transport systems. In *E. coli*,  
788 the proton electrochemical gradient across the inner membrane is leveraged to transport inorganic phosphate  
789 into the cell (*Rosenberg et al., 1977*). Proton-solute symporters are widespread in *E. coli* (*Ramos and Kaback, 1977*;  
790 *Booth et al., 1979*) and can have rapid transport rates of 50 to 100 molecules per second for sugars and other  
791 solutes (BNID: 103159; 111777). As a more extreme example, the proton transporters in the F<sub>1</sub>-F<sub>0</sub> ATP synthase,  
792 which use the proton electrochemical gradient for rotational motion, can shuttle protons across the membrane at  
793 a rate of  $\approx 1000$  per second (BNID: 104890; 103390). In *E. coli* the PitA phosphate transport system has been shown  
794 to be very tightly coupled with the proton electrochemical gradient with a 1:1 proton:phosphate stoichiometric  
795 ratio (*Harris et al., 2001; Feist et al., 2007*). Taking the geometric mean of the aforementioned estimates gives a  
796 plausible rate of phosphate transport on the order of 300 per second. Illustrated in ??(A), we can estimate that  $\approx$   
797 200 phosphate transporters are necessary to maintain an  $\approx 3\%$  dry mass with a 5000 s division time. This estimate  
798 is consistent with observation when we examine the observed copy numbers of PitA in proteomic data sets (plot in  
799 ??(A)). While our estimate is very much in line with the observed numbers, we emphasize that this is likely a slight  
800 overestimate of the number of transporters needed as there are other phosphorous scavenging systems, such as  
801 the ATP-dependent phosphate transporter Pst system which we have neglected.

802 **Sulfur**

803 Similar to phosphate, sulfate is highly-charged and not particularly membrane permeable, requiring active transport.  
804 While there exists a H<sup>+</sup>/sulfate symporter in *E. coli*, it is in relatively low abundance and is not well characterized  
805 (*Zhang et al., 2014a*). Sulfate is predominantly acquired via the ATP-dependent ABC transporter CysUWA system  
806 which also plays an important role in selenium transport (*Sekowska et al., 2000; Sirko et al., 1995*). While specific

807 kinetic details of this transport system are not readily available, generic ATP transport systems in prokaryotes  
808 transport on the order of 1 to 10 molecules per second (BNID: 109035). Combining this generic transport rate,  
809 measurement of sulfur comprising 1% of dry mass, and a 5000 second division time yields an estimate of  $\approx$  1000  
810 CysUWA complexes per cell (??(B)). Once again, this estimate is in notable agreement with proteomic data sets,  
811 suggesting that there are sufficient transporters present to acquire the necessary sulfur. In a similar spirit of our  
812 estimate of phosphorus transport, we emphasize that this is likely an overestimate of the number of necessary  
813 transporters as we have neglected other sulfur scavenging systems that are in lower abundance.

#### 814 Additional Process of the Central Dogma

815 In the main text, we consider the processes underlying the backbone of the central dogma, namely DNA replication,  
816 RNA transcription, and protein translation. In this section we turn our attention to additional processes related to  
817 the central dogma, primarily dNTP synthesis for DNA replication and amino-acyl tRNA synthesis for translation.  
818 Additionally, we explore in more detail the estimates shown in *Figure 7(A)* for the RNA polymerase requirements of  
819 mRNA and tRNA synthesis.

#### 820 dNTP synthesis

821 The four major dNTPs (dATP, dTTP, dCTP, and dGTP) serve as the fundamental units of the genetic code. Thus, to  
822 faithfully replicate the chromosome, the cell must be able to synthesize enough of these bases in the first place.  
823 All dNTPs are synthesized *de novo* in separate pathways, requiring different building blocks. However, a critical  
824 step present in all dNTP synthesis pathways is the conversion from ribonucleotide to deoxyribonucleotide via  
825 the removal of the 3' hydroxyl group of the ribose ring (Rudd et al., 2016). This reaction is mediated by a class of  
826 enzymes termed ribonucleotide reductases, of which *E. coli* possesses two aerobically active complexes (termed I  
827 and II) and a single anaerobically active enzyme. Due to their peculiar formation of a radical intermediate, these  
828 enzymes have received much biochemical, kinetic, and structural characterization. One such work (Ge et al.,  
829 2003) performed a detailed *in vitro* measurement of the steady-state kinetic rates of these complexes, revealing a  
830 turnover rate of  $\approx$  10 dNTP per second.

831 Since this reaction is central to the synthesis of all dNTPs, it is reasonable to consider the abundance of  
832 these complexes as a measure of the total dNTP production in *E. coli*. Illustrated schematically in *Figure 6 (A)*, we  
833 consider the fact that to replicate the cell's genome, on the order of  $\approx$  10<sup>7</sup> dNTPs must be synthesized. Assuming a  
834 production rate of 10 per second per ribonucleotide reductase complex and a cell division time of 5000 seconds,  
835 we arrive at an estimate of  $\approx$  200 complexes needed per cell. As shown in the bottom panel of *Figure Supplement 1*  
836 (A), this estimate agrees with the experimental measurements of these complexes abundances within  $\approx$  1/2 an  
837 order of magnitude. Extension of this estimate across a continuum of growth rate, including the fact that multiple  
838 chromosomes can be replicated at a given time, is shown as a grey transparent line in *Figure Supplement 1*.  
839 Similarly to our point estimate, this refinement agrees well with the data, accurately describing both the magnitude  
840 of the complex abundance and the dependence on growth rate.

841 Recent work has revealed that during replication, the ribonucleotide reductase complexes coalesce to form  
842 discrete foci colocalized with the DNA replisome complex (Sánchez-Romero et al., 2011). This is particularly  
843 pronounced in conditions where growth is slow, indicating that spatial organization and regulation of the activity of  
844 the complexes plays an important role.

#### 845 mRNA and tRNA Synthesis

846 In *Figure 7* of the main text, we present with limited explanation estimates for the number of RNA polymerases  
847 needed to synthesize enough mRNA and tRNA molecules. Here, we present a rationalization for these estimates.

848 To form a functional protein, all protein coding genes must first be transcribed from DNA to form an mRNA  
849 molecule. While each protein requires an mRNA blueprint, many copies of the protein can be synthesized from  
850 a single mRNA. Factors such as strength of the ribosomal binding site, mRNA stability, and rare codon usage  
851 frequency dictate the number of proteins that can be made from a single mRNA, with yields ranging from 10<sup>1</sup> to 10<sup>4</sup>  
852 (BNID: 104186; 100196; 106254). Computing the geometric mean of this range yields  $\approx$  1000 proteins synthesized  
853 per mRNA, a value that agrees with experimental measurements of the number of proteins per cell ( $\approx$  3  $\times$  10<sup>6</sup>, BNID:  
854 100088) and total number of mRNA per cell ( $\approx$  3  $\times$  10<sup>3</sup>, BNID:100064).

855 This estimation captures the *steady-state* mRNA copy number, meaning that at any given time, there will exist  
856 approximately 3000 unique mRNA molecules. To determine the *total* number of mRNA that need to be synthesized  
857 over the cell's lifetime, we must consider degradation of the mRNA. In most bacteria, mRNAs are rather unstable  
858 with life times on the order of several minutes (BNID: 104324; 106253; 111927; 111998). For convenience, we  
859 assume that the typical mRNA in our cell of interest has a typical lifetime of  $\approx$  300 seconds. Using this value, we  
860 can determine the total mRNA production rate to maintain a steady-state copy number of 3000 mRNA per cell.  
861 While we direct the reader to the appendix for a more detailed discussion of mRNA transcriptional dynamics, we  
862 state here that the total mRNA production rate must be on the order of  $\approx$  15 mRNA per second. In *E. coli*, the  
863 average protein is  $\approx$  300 amino acids in length (BNID: 108986), meaning that the corresponding mRNA is  $\approx$  900  
864 nucleotides which we will further approximate as  $\approx$  1000 nucleotides to account for the non-protein coding regions  
865 on the 5' and 3' ends. This means that the cell must have enough RNA polymerase molecules about to sustain a  
866 transcription rate of  $\approx$   $1.5 \times 10^4$  nucleotides per second. Knowing that a single RNA polymerase polymerizes RNA  
867 at a clip of 40 nucleotides per second, we arrive at a comfortable estimate of  $\approx$  250 RNA polymerase complexes  
868 needed to satisfy the mRNA demands of the cell. It is worth noting that this number is approximately half of that  
869 required to synthesize enough rRNA, as we saw in the previous section. We find this to be a striking result as these  
870 250 RNA polymerase molecules are responsible for the transcription of the  $\approx$  4000 protein coding genes that are  
871 not ribosome associated.

872 We now turn our attention to the synthesis of tRNA. Unlike mRNA or rRNA, each individual tRNA is remarkably  
873 short, ranging from 70 to 95 nucleotides each (BNID: 109645; 102340). What they lack in length, they make up  
874 for in abundance, with reported values ranging from  $\approx 5 \times 10^4$  (BNID: 105280) to  $\approx 5 \times 10^5$  (BNID: 108611). To test  
875 tRNA synthesis as a possible growth-rate limiting stage, we will err towards a higher abundance of  $\approx 5 \times 10^5$  per cell.  
876 Combining the abundance and tRNA length measurements, we make the estimate that  $\approx 5 \times 10^7$  nucleotides are  
877 sequestered in tRNA per cell. Unlike mRNA, tRNA is remarkably stable with typical lifetimes *in vivo* on the order of  $\approx$   
878 48 hours (*Abelson et al., 1974; Svenningsen et al., 2017*) – well beyond the timescale of division. Once again using  
879 our rule-of-thumb for the rate of transcription to be 40 nucleotides per second and assuming a division time of  $\approx$   
880 5000 seconds, we arrive at an estimate of  $\approx$  200 RNA polymerases to synthesize enough tRNA. This requirement  
881 pales in comparison to the number of polymerases needed to generate the rRNA and mRNA pools and can be  
882 neglected as a significant transcriptional burden.

### 883 tRNA Charging

884 In the previous subsection, we focused solely on estimating the number of RNA polymerases needed for the  
885 generation of the tRNA molecule itself. We now explore the protein complex requirements for ligation of the  
886 appropriate amino acid to each tRNA. We begin by again using an estimate of  $\approx 3 \times 10^6$  proteins per cell at a 5000 s  
887 division time (BNID: 115702) and a typical protein length of  $\approx$  300 amino acids (BNID: 100017), we can estimate  
888 that a total of  $\approx 10^9$  amino acids are stitched together by peptide bonds.

889 How many tRNAs are needed to facilitate this remarkable number of amino acid delivery events to the translating  
890 ribosomes? It is important to note that tRNAs are recycled after they've passed through the ribosome and can be  
891 recharged with a new amino acid, ready for another round of peptide bond formation. While some *in vitro* data  
892 exists on the turnover of tRNA in *E. coli* for different amino acids, we can make a reasonable estimate by comparing  
893 the number of amino acids to be polymerized to cell division time. Using our stopwatch of 5000 s and  $10^9$  amino  
894 acids, we arrive at a requirement of  $\approx 2 \times 10^5$  tRNA molecules to be consumed by the ribosome per second.

895 There are many processes which go into synthesizing a tRNA and ligating it with the appropriate amino acids.  
896 As we discussed previously, there appear to be more than enough RNA polymerases per cell to synthesize the  
897 needed pool of tRNAs. Without considering the many ways in which amino acids can be scavenged or synthesized  
898 *de novo*, we can explore ligation the as a potential rate limiting step. The enzymes which link the correct amino acid  
899 to the tRNA, known as tRNA synthetases or tRNA ligases, are incredible in their proofreading of substrates with the  
900 incorrect amino acid being ligated once out of every  $10^4$  to  $10^5$  events (BNID: 103469). This is due in part to the  
901 consumption of energy as well as a multi-step pathway to ligation. While the rate at which tRNA is ligated is highly  
902 dependent on the identity of the amino acid, it is reasonable to state that the typical tRNA synthetase has charging  
903 rate of  $\approx$  20 AA per tRNA synthetase per second (BNID: 105279).

904 We can make an assumption that amino-acyl tRNAs are in steady-state where they are produced at the same

**Table 1.** Overview of proteomic data sets.

Author	Method	Reported Quantity
Taniguchi <i>et al.</i> (2010)	YFP-fusion, cell fluorescence	fg/copies per cell
Valgepea <i>et al.</i> (2012)	mass spectrometry	fg/copies per cell
Peebo <i>et al.</i> (2014)	mass spectrometry	fg/copies per fl
Li <i>et al.</i> (2014)	ribosomal profiling	fg/copies per cell <sup>a</sup>
Soufi <i>et al.</i> (2015)	mass spectrometry	fg/copies per cell
Schmidt <i>et al.</i> (2016)	mass spectrometry	fg/copies per cell <sup>b</sup>

a. The reported values assume that the proteins are long-lived compared to the generation time but are unable to account for post-translational modifications that may alter absolute protein abundances.

b. This mass spectrometry approach differs substantially from the others since in addition to the relative proteome-wide abundance measurements, the authors performed absolute quantification of 41 proteins across all growth conditions (see section on Additional Considerations of Schmidt *et al.* Data Set for more details on this).

905 rate they are consumed, meaning that  $2 \times 10^5$  tRNAs must be charged per second. Combining these estimates  
906 together, as shown schematically in ??, yields an estimate of  $\sim 10^4$  tRNA synthetases per cell with a division time of  
907 5000 s. This point estimate is in very close agreement with the observed number of synthetases (the sum of all  
908 20 tRNA synthetases in *E. coli*). This estimation strategy seems to adequately describe the observed growth rate  
909 dependence of the tRNA synthetase copy number (shown as the grey line in ??, suggesting that the copy number  
910 scales with the cell volume.

911 In total, the estimated and observed  $\sim 10^4$  tRNA synthetases occupy only a meager fraction of the total cell  
912 proteome, around 0.5% by abundance. It is reasonable to assume that if tRNA charging was a rate limiting  
913 process, cells would be able to increase their growth rate by devoting more cellular resources to making more tRNA  
914 synthetases. As the synthesis of tRNAs and the corresponding charging can be highly parallelized, we can argue that  
915 tRNA charging is not a rate limiting step in cell division, at least for the growth conditions explored in this work.

## 916 Experimental Details Behind Proteomic Data

917 Here we provide a brief summary of the experiments behind each proteomic data set considered. The purpose of  
918 this section is to identify how the authors arrived at absolute protein abundances. In the following section (see  
919 section on Summary of Proteomic Data) we will then provide a summary of the protein abundance measurements.  
920 Table 1 provides an overview of the publications we considered. These are predominately mass spectrometry-based,  
921 with the exception of the work from Li *et al.* (2014) which used ribosomal profiling, and the fluorescence-based  
922 counting done in Taniguchi *et al.* (2010). After having compiled and comparing these measurements, we noted  
923 substantial deviations in the measurements from Taniguchi *et al.* (2010) and Soufi *et al.* (2015) (shown in the  
924 following section), and decided to only use the data from Taniguchi *et al.* (2010); Li *et al.* (2014); Valgepea *et al.*  
925 (2013); Peebo *et al.* (2015) in the main text. For completeness, we include these additional datasets in our discussion  
926 of the experimental data.

## 927 Fluorescence based measurements

928 In the work of Taniguchi *et al.* (2010), the authors used a chromosomal YFP fusion library where individual strains  
929 have a specific gene tagged with a YFP-coding sequence. 1018 of their 1400 attempted strains were used in the work.  
930 A fluorescence microscope was used to collect cellular YFP intensities across all these strains. Through automated  
931 image analysis, the authors normalized intensity measurements by cell size to account for the change in size and  
932 expression variability across the cell cycle. Following correction of YFP intensities for cellular autofluorescence,  
933 final absolute protein levels were determined by a calibration curve with single-molecule fluorescence intensities.  
934 This calibration experiment was performed separately using a purified YFP solution.

935 **Ribosomal profiling measurements**

936 The work of *Li et al. (2014)* takes a sequencing based approach to estimate protein abundance. Ribosomal  
937 profiling, which refers to the deep sequencing of ribosome-protected mRNA fragments, can provide a quantitative  
938 measurement of the protein synthesis rate. As long as the protein life-time is long relative to the cell doubling time,  
939 it is possible to estimate absolute protein copy numbers. The absolute protein synthesis rate has units of proteins  
940 per generation, and for stable proteins will also correspond to the protein copy number per cell.

941 In the experiments, ribosome-protected mRNA is extracted from cell lysate and selected on a denaturing  
942 polyacrylamide gel for deep sequencing (15–45 nt long fragments collected and sequenced by using an Illumina  
943 HiSeq 2000 in *Li et al. (2014)*). Counts of ribosome footprints from the sequencing data were then corrected  
944 empirically for position-dependent biases in ribosomal density across each gene, as well as dependencies on  
945 specific sequences including the Shine-Dalgarno sequence. These data-corrected ribosome densities represent  
946 relative protein synthesis rates. Absolute protein synthesis rates are obtained by multiplying the relative rates by  
947 the total cellular protein per cell. The total protein per unit volume was determined with the Lowry method to  
948 quantify total protein, calibrated against bovine serum albumin (BSA). By counting colony-forming units following  
949 serial dilution of their cell cultures, they then calculated the total protein per cell.

950 **Mass spectrometry measurements**

951 Perhaps not surprisingly, the data is predominantly mass spectrometry based. This is largely due to tremendous  
952 improvements in the sensitivity of mass spectrometers, as well as improvements in sample preparation and  
953 data analysis pipelines. It is now a relatively routine task to extract protein from a cell and quantify the majority  
954 of proteins present by shotgun proteomics. In general, this involves lysing cells, enzymatically digesting the  
955 proteins into short peptide fragments, and then introducing them into the mass spectrometer (e.g. with liquid  
956 chromatography and electrospray ionization), which itself can have multiple rounds of detection and further  
957 fragmentation of the peptides.

958 Most quantitative experiments rely on labeling protein with stable isotopes, which allow multiple samples  
959 to be measured together by the mass spectrometer. By measuring samples of known total protein abundance  
960 simultaneously (i.e. one sample of interest, and one reference), it is possible to determine relative protein  
961 abundances. Absolute protein abundances can be estimated following the same approach used above for  
962 ribosomal profiling, which is to multiply each relative abundance measurement by the total cellular protein per  
963 cell. This is the approach taken by *Valgepea et al. (2013)*; *Peebo et al. (2015)* and *Soufi et al. (2015)*, with relative  
964 protein abundances determined based on the relative peptide intensities (label free quantification 'LFQ' intensities).  
965 For the data of *Valgepea et al. (2013)*, total protein per cell was determined by measuring total protein by the  
966 Lowry method, and counting colony-forming units following serial dilution. For the data from *Peebo et al. (2015)*,  
967 the authors did not determine cell quantities and instead report the cellular protein abundances in protein per  
968 unit volume by assuming a mass density of 1.1 g/ml, with a 30% dry mass fraction.

969 An alternative way to arrive at absolute protein abundances is to dope in synthetic peptide fragments of known  
970 abundance. These can serve as a direct way to calibrate mass spectrometry signal intensities to absolute mass.  
971 This is the approach taken by *Schmidt et al. (2016)*. In addition to a set of shotgun proteomic measurements to  
972 determine proteome-wide relative abundances, the authors also performed absolute quantification of 41 proteins  
973 covering over four orders of magnitude in cellular abundance. Here, a synthetic peptide was generated for each of  
974 the proteins, doped into each protein sample, and used these to determine absolute protein abundances of the 41  
975 proteins. These absolute measurements, determined for every growth condition, were then used as a calibration  
976 curve to convert proteomic-wide relative abundances into absolute protein abundance per cell. A more extensive  
977 discussion of the *Schmidt et al. (2016)* data set can be found in Section Additional Considerations of Schmidt et al.  
978 Data Set.

979 **Summary of Proteomic Data**

980 In the work of the main text we only used the data from *Valgepea et al. (2013)*; *Li et al. (2014)*; *Peebo et al. (2015)*;  
981 *Schmidt et al. (2016)*. As shown in *Figure 12(A)*, the reported total protein abundances in the work of *Taniguchi*  
982 *et al. (2010)* and *Soufi et al. (2015)* differed quite substantially from the other work. For the work of *Taniguchi et al.*

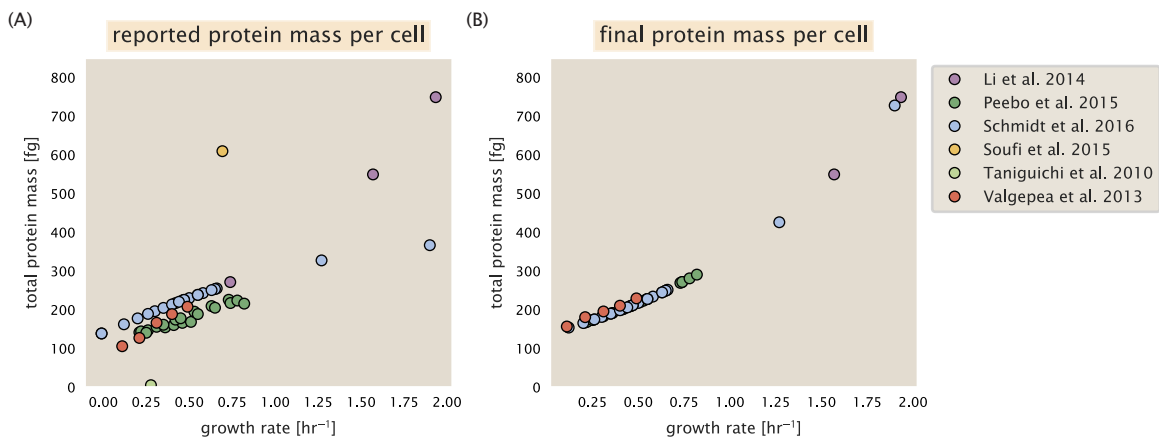


**Figure 12. Summary of the growth-rate dependent total protein abundance for each data set.** (A) Total protein abundance per cell as originally reported in the data sets of *Taniguchi et al. (2010)*; *Valgepea et al. (2013)*; *Li et al. (2014)*; *Soufi et al. (2015)*; *Peebo et al. (2015)*; *Schmidt et al. (2016)*. Note that the data from *Peebo et al. (2015)* only reported protein abundances per unit volume and total protein per cell was found by multiplying these by the growth-rate dependent cell size as determined by *Si et al. (2017)*. (B) Adjusted total protein abundances across the proteomic data sets are summarized. Protein abundances were adjusted so that all data shared a common set of growth-rate dependent total protein per cell and cellular protein concentration following the cell size expectations of *Si et al. (2017)* (see section on Estimation of Cell Size and Surface Area for further details).

983 (2010) this is in part due to a lower coverage in total proteomic mass quantified, though we also noticed that most  
984 proteins appear undercounted when compared to the other data.

985 **Figure 12(B)** summarizes the total protein mass for each data set used in our final compiled data set. Our  
986 inclination initially was to leave reported copy numbers untouched, but a notable discrepancy between the scaling  
987 of the total protein per cell between *Schmidt et al. (2016)* and the other data sets forced us to dig deeper into  
988 those measurements (compare *Schmidt et al. (2016)* and *Li et al. (2014)* data in **Figure 12(A)**). The particular trend  
989 in *Schmidt et al. (2016)* appears to be due to assumptions made about cell size and we provide a more extensive  
990 discussion and analysis of their data in Additional Considerations of Schmidt et al. Data Set. As a compromise, and  
991 in an effort to treat all data equally, we instead applied a correction factor to all protein abundance values based  
992 on a data-driven estimate of total protein per cell. Here we used cell size measurements from *Si et al. (2017, 2019)*,  
993 and an estimate of total protein content through expected dry mass. Total protein per cell was then determined  
994 using available data on total DNA, RNA, and protein from *Basan et al. (2015)*; *Dai et al. (2016)*, which account for  
995 the majority of dry mass in the cell. We describe these details further in sections on Estimation of Cell Size and  
996 Surface Area and Estimation of Total Protein Content per Cell that follows.

997 Lastly, in **Figure 13** we show the total proteomic coverage and overlap of proteins quantified across each data  
998 set. Here we have used an UpSet diagram (*Lex et al., 2014*) to compare the data. Overall, the overlap in quantified  
999 proteins is quite high, with 1157 proteins quantified across all data sets. The sequencing based approach of *Li*  
1000 *et al. (2014)* has substantially higher coverage compared to the mass spectrometry data sets (3394 genes versus  
1001 the 2041 genes quantified in the work of *Schmidt et al. (2016)*). However, in terms of total protein mass, the data  
1002 from *Li et al. (2014)*; *Schmidt et al. (2016)*; *Peebo et al. (2015)* each quantify roughly equivalent total protein mass.  
1003 An exception to this is in the data from *Valgepea et al. (2013)*, where we find that the total protein quantified in  
1004 *Valgepea et al. (2013)* is 90-95 % of the total protein mass (when using the data from *Schmidt et al. (2016)* as a  
1005 reference).

#### 1006 **Estimation of Cell Size and Surface Area**

1007 Since most of the proteomic data sets lack cell size measurements, we chose instead to use a common estimate of  
1008 size for any analysis requiring cell size or surface area. Since each of the data sets used either K-12 MG1655 or  
1009 its derivative, BW25113 (from the lab of Barry L. Wanner; the parent strain of the Keio collection (*Datsenko and*  
1010 *Wanner, 2000; Baba et al., 2006*)), below we fit the MG1655 cell size data from the supplemental material of *Si*

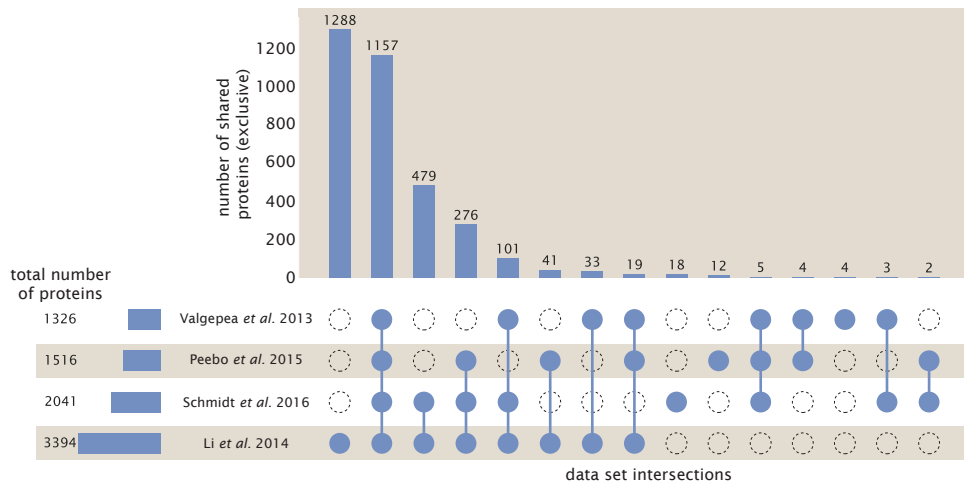


**Figure 13. Comparison of proteomic coverage across different data sets.** An UpSet diagram (*Lex et al., 2014*) summarizes the total number of protein coding genes whose protein abundance was reported in the data sets of *Valgepea et al. (2013)*; *Li et al. (2014)*; *Schmidt et al. (2016)*; *Peebo et al. (2015)*. Bar plot on bottom left indicates the total number of genes reported in each individual data. The main bar plot summarizes the number of unique proteins identified across overlapping subsets of the data. For example, in the first column only the data from *Li et al. (2014)* is considered (indicated by solid blue circle) and 1288 proteins are identified as exclusive to the data set. In the second column, the intersection of all four data sets is considered, with 1157 proteins quantified across them. This follows for each additional column in the plot, with the subset under consideration denoted by the solid blue circles.

1011     *et al. (2017, 2019)* using the `optimize.curve_fit` function from the Scipy python package (*Virtanen et al., 2020*). A  
 1012     quick comment on nomenclature: throughout the text, we usually refer to cell size, in units of  $\mu\text{m}^3$ ; however, on  
 1013     occasion we will mention size as a volume in units of fL.

1014     The average size measurements from each of their experiments are shown in **Figure 14**, with cell length and  
 1015     width shown in (A) and (B), respectively. The length data was well described by the exponential function  $0.5 e^{1.09 \cdot \lambda} +$   
 1016      $1.76 \mu\text{m}$ , while the width data was well described by  $0.64 e^{0.24 \cdot \lambda} \mu\text{m}$ . In order to estimate cell size we take the cell as  
 1017     a cylinder with two hemispherical ends (*Si et al., 2017; Basan et al., 2015*). Specifically, cell size is estimated from,

$$V = \pi \cdot r^2 \cdot (l - 2r/3), \quad (5)$$

1018     where  $r$  is half the cell width. A best fit to the data is described by  $0.533 e^{1.037 \cdot \lambda} \mu\text{m}^3$ . Calculation of the cell surface  
 1019     area is given by,

$$S = \eta \cdot \pi \left( \frac{\eta \cdot \pi}{4} - \frac{\pi}{12} \right)^{-2/3} V^{2/3}, \quad (6)$$

1020     where  $\eta$  is the aspect ratio ( $\eta = l/w$ ) (*Ojkic et al., 2019*).

## 1021     Estimation of Total Protein Content per Cell

1022     In order to estimate total protein per cell for a particular growth rate, we begin by estimating the cell size from the  
 1023     fit shown in **Figure 14(C)** (cell size =  $0.533 e^{1.037 \cdot \lambda} \mu\text{m}^3$ , as noted in the previous section). We then estimate the total  
 1024     protein content from the total dry mass of the cell. Here we begin by noting that for almost the entire range of  
 1025     growth rates considered here, protein, DNA, and RNA were reported to account for at least 90 % of the dry mass  
 1026     (*Basan et al. (2015)*). The authors also found that the total dry mass concentration was roughly constant across  
 1027     growth conditions. Under such a scenario, we can calculate the total dry mass concentration for protein, DNA, and  
 1028     RNA, which is given by  $1.1 \text{ g/ml} \times 30 \% \times 90 \% \text{ or about } [M_p] = 300 \text{ fg per fL}$ . Multiplying this by our prediction of  
 1029     cell size gives the total dry mass per cell.

1030     However, even if dry mass concentration is relatively constant across growth conditions, it is not obvious how  
 1031     protein concentration might vary due to the substantial increase in rRNA at faster growth rates (*Dai et al. (2016)*).  
 1032     The increase in rRNA increases from the linear increase in ribosomal content with faster growth rate (*Scott et al.*

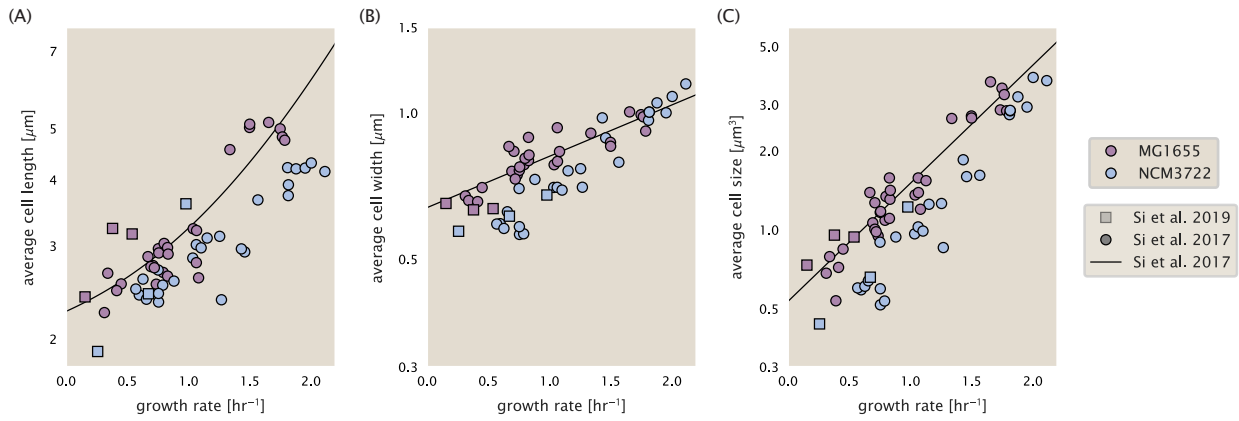


**Figure 14. Summary of size measurements from Si et al. 2017, 2019.** Cell lengths and widths were measured from cell contours obtained from phase contrast images, and refer to the long and short axis respectively. (A) Cell lengths and (B) cell widths show the mean measurements reported (they report 140-300 images and 5,000-30,000 for each set of samples; which likely means about 1,000-5,000 measurements per mean value reported here since they considered about 6 conditions at a time). Fits were made to the MG1655 strain data; length:  $0.5 e^{1.09 \cdot \lambda} + 1.76 \mu\text{m}$ , width:  $0.64 e^{0.24 \cdot \lambda} \mu\text{m}$ . (C) Cell size was calculated as cylinders with two hemispherical ends (Equation 5). The MG1655 strain data gave a best fit of  $0.533 e^{1.037 \cdot \lambda} \mu\text{m}^3$ .

1033 (2010)), since it makes up about about 2/3 or the ribosomal mass. To proceed we therefore relied on experimental  
 1034 measurements of total DNA content per cell from Basan et al. (2015), and RNA to protein ratios that were measured  
 1035 in Dai et al. (and cover the entire range of growth conditions considered here). These are reproduced in Figure 15(A)  
 1036 and (B), respectively.

1037 Assuming that the protein, DNA, and RNA account for 90 % of the total dry mass, the protein mass can then  
 1038 determined by first subtracting the experimentally measured DNA mass, and then using the experimental estimate  
 1039 of the RNA to protein ratio. The total protein per cell is will be related to the summed RNA and protein mass by,

$$M_P = \frac{[M_P + M_{RNA}]}{1 + (RP_{ratio})}. \quad (7)$$

1040 ( $RP_{ratio}$  refers to the RNA to protein ratio as measured by Dai et al.. In Figure 15(C) we plot the estimated cellular  
 1041 concentrations for protein, DNA, and RNA from these calculations, and in Figure 15(D) we plot their total expected  
 1042 mass per cell. This later quantity is the growth rate-dependent total protein mass that was used to estimate total  
 1043 protein abundance across all data sets (and summarized in Figure 12(B)).

#### 1044 Estimating Volume and Number of Amino Acids from Ribosome Copy Number

1045 Towards the end of the main text, we examine a coarse-grained model of nutrient-limited growth. A key point  
 1046 in our analysis was to consider how elongation rate  $r_i$  and growth rate  $\lambda$  vary with respect to the experimentally  
 1047 observed changes in cell size, total number of peptide bonds per cell  $N_{pep}$ , and ribosomal content. In order to  
 1048 restrict parameters to those observed experimentally, but otherwise allow us to explore the model, we performed  
 1049 a phenomenological fit of  $N_{pep}$  and  $V$  as a function of the measured ribosomal copy number  $R$ . As has been  
 1050 described in the preceding sections of this supplement, we estimate cell volume for each growth condition using  
 1051 the size measurements from Si et al. (2017, 2019), and  $N_{pep}$  is approximated by taking the total protein mass and  
 1052 dividing this number by the average mass of an amino acid, 110 Da (BNID: 104877).

1053 Given the exponential scaling of  $V$  and  $N_{pep}$  with growth rate, we performed a linear regression of the log  
 1054 transform of these parameters as a function of the log transform of the ribosome copy number. Using optimization  
 1055 by minimization, we estimated the best-fit values of the intercept and slope for each regression. Figure 16 shows  
 1056 the result of each regression as a dashed line.

#### 1057 Additional Considerations of Schmidt et al. Data Set

1058 While the data set from Schmidt et al. (2016) remains a heroic effort that our labs continue to return to as a resource,  
 1059 there were steps taken in their calculation of protein copy number that we felt needed further consideration. In

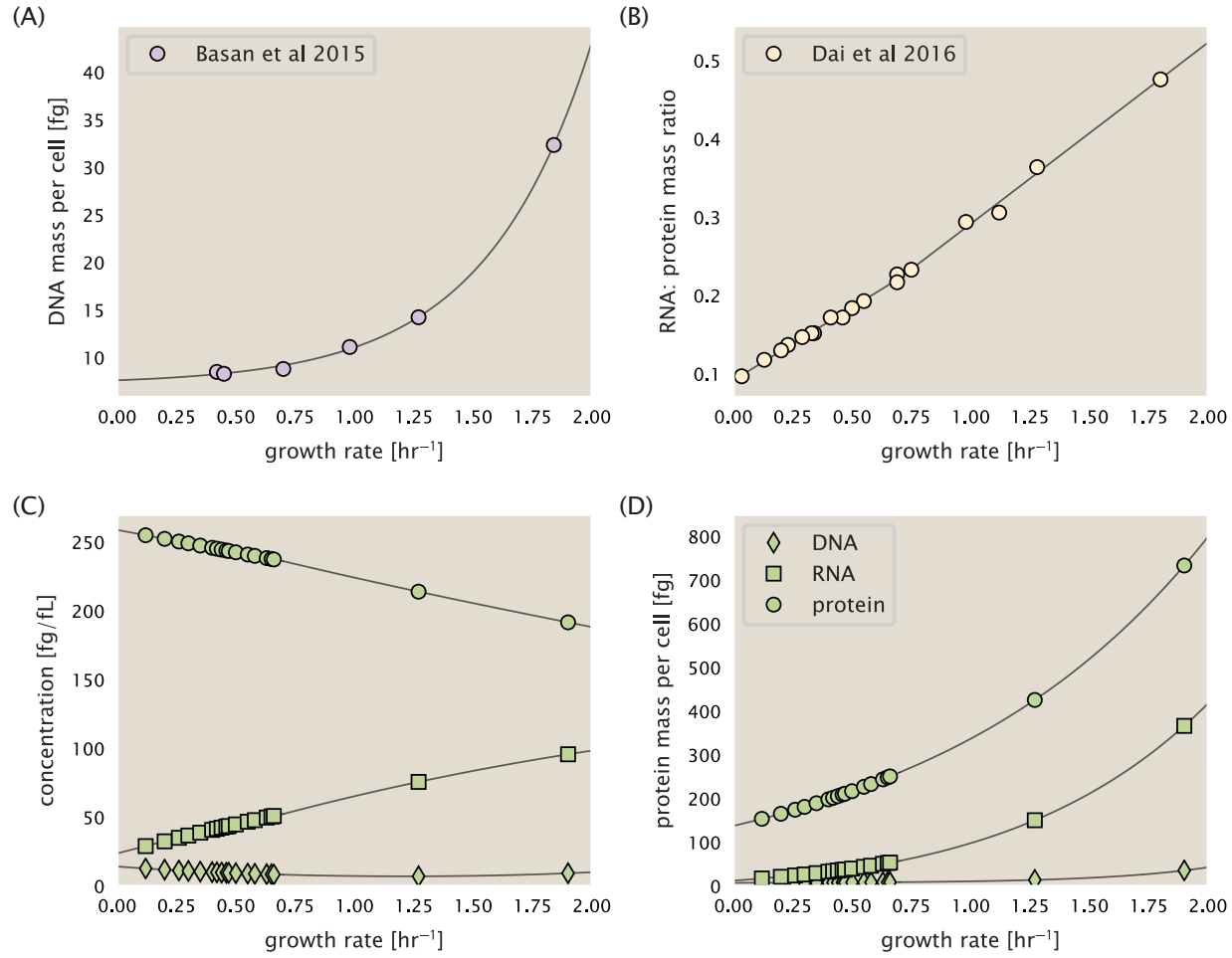


**Figure 15. Empirical estimate of cellular protein, DNA, and RNA as a function of growth rate.** (A) Measured DNA mass per cell as a function of growth rate, reproduced from Basan et al. 2015. The data was fit to an exponential curve (DNA mass in fg per cell is given by  $0.42 e^{2.23 \cdot \lambda} + 7.2$  fg per cell, where  $\lambda$  is the growth rate in  $\text{hr}^{-1}$ ). (B) RNA to protein measurements as a function of growth rate. The data was fit to two lines (shown in black) due to the change in slope at slower growth rates Neidhardt et al. (1991); Dai et al. (2016). For growth rates below  $0.7 \text{ hr}^{-1}$ , the RNA/protein ratio is  $0.18 \cdot \lambda + 0.093$ , while for growth rates faster than  $0.7 \text{ hr}^{-1}$  the RNA/protein ratio is given by  $0.25 \cdot \lambda + 0.035$ . For (A) and (B) cells are grown under varying levels of nutrient limitation, with cells grown in minimal media with different carbon sources for the slowest growth conditions, and rich-defined media for fast growth rates. (C) Estimation of cellular protein, DNA, and RNA concentration. (D) Total cellular mass estimated for protein, DNA, and RNA using the cell size calculated in ???. Symbols (diamond: DNA, square: RNA, circle: protein) show estimated values of mass concentration and mass per cell for the specific growth rates in Schmidt et al. (2016).

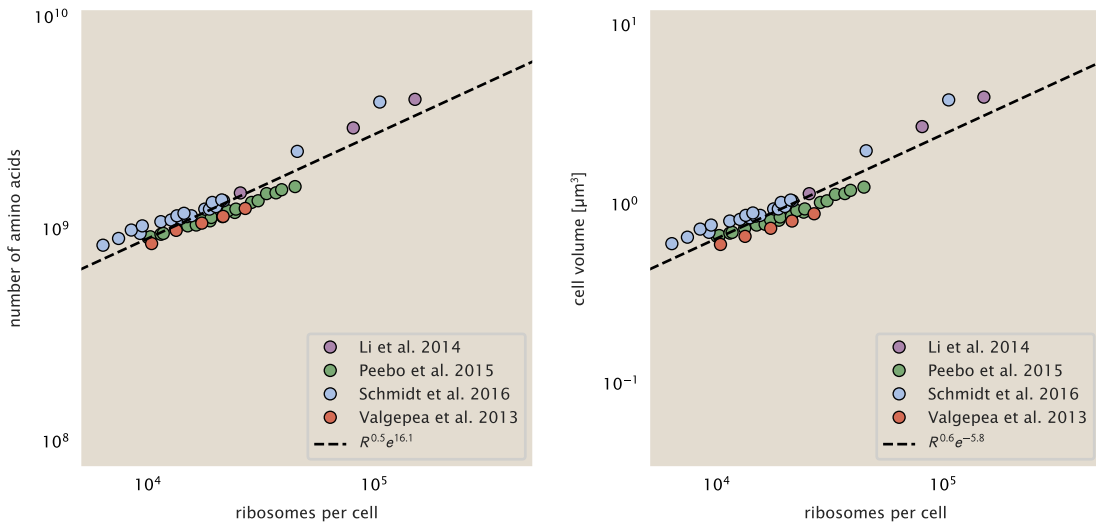


**Figure 16. Phenomenological regression of cell volume and number of amino acids per cell as a function of the ribosome copy number.** Colored points correspond to the measured value (or calculated value in the case of the cell volume) with colors denoting different data sets. The dashed black line shows the result of the fit, with the functional form of the equation given in the legend with  $R$  representing the ribosome copy number.

particular, the authors made an assumption of constant cellular protein concentration across all growth conditions and used measurements of cell volume that appear inconsistent with an expected exponential scaling of cell size with growth rate that is well-documented in *E. coli* (*Schaechter et al. (1958); Taheri-Araghi et al. (2015); Si et al. (2017)*).

We begin by looking at their cell volume measurements, which are shown in blue in Figure *Figure 17*. As a comparison, we also plot cell sizes reported in three other recent papers: measurements from Taheri-Araghi *et al.* and Si *et al.* come from the lab of Suckjoon Jun, while those from Basan *et al.* come from the lab of Terence Hwa. Each set of measurements used microscopy and cell segmentation to determine the length and width, and then calculated cell size by treating the cell as a cylinder with two hemispherical ends, as we considered in the previous section. While there is notable discrepancy between the two research groups, which are both using strain NCM3722, Basan *et al.* found that this came specifically from uncertainty in determining the cell width. This is prone to inaccuracy given the small cell size and optical resolution limits (further described in their supplemental text). Perhaps the more concerning point is that while each of these alternative measurements show an exponential increase in cell size at faster growth rates, the measurements used by Schmidt *et al.* appear to plateau. This resulted in an analogous trend in their final reported total cellular protein per cell as shown in *Figure 18* (purple data points), and is in disagreement with other measurements of total protein at these growth rates (*Basan et al., 2015*).

Since it is not obvious how measurements of cell size influenced their reported protein abundances, in the following subsections we begin by considering how the authors determined total protein mass per cell. We then consider three different approaches to estimate the growth-rate dependent total protein mass and compare these estimates with those reported by Schmidt *et al. (2016)*. Those results are summarized in *Figure 17(B)*, with the original values from both Schmidt *et al. (2016)* and Li *et al. (2014)* shown in *Figure 17(A)* for reference. For most growth conditions, we find reasonable agreement between our estimates and the reported total protein per cell. However, for the fastest growth conditions, with glycerol + supplemented amino acids, and LB media, all estimates are substantially higher than those originally reported. This is the main reason why we chose to readjust protein abundance as shown in *Figure 12(B)* (with the calculation described in section Estimation of Total Protein Content per Cell).

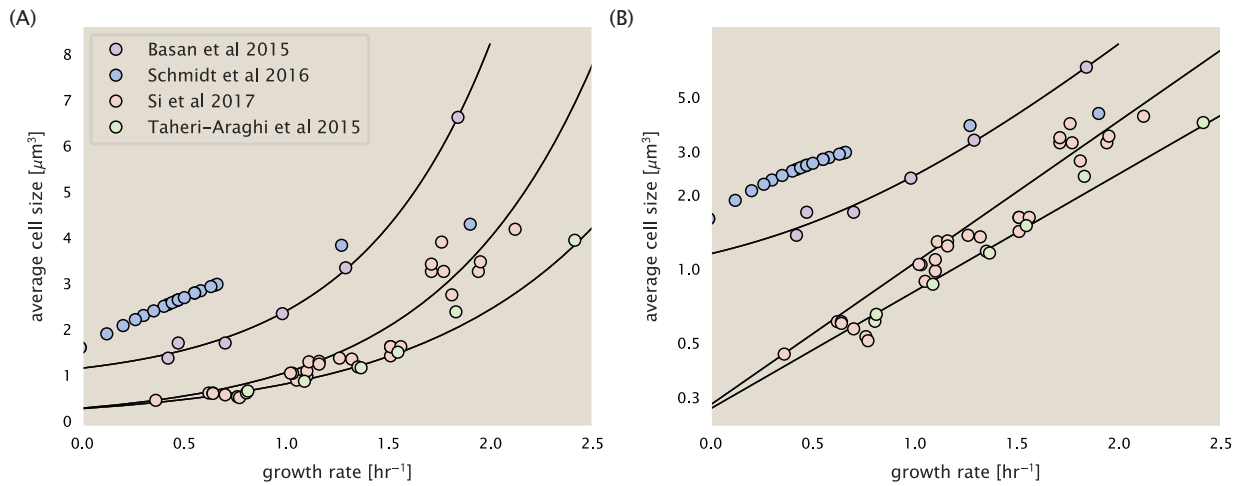


**Figure 17. Measurements of cell size as a function of growth rate.** (A) Plot of the reported cell sizes from several recent papers. The data in blue come from Volkmer and Heinemann, 2011 (*Volkmer and Heinemann (2011)*) and were used in the work of Schmidt *et al.*. Data from the lab of Terence Hwa are shown in purple (*Basan et al. (2015)*), while the two data sets shown in green and light red come from the lab of Suckjoon Jun (*Taheri-Araghi et al. (2015); Si et al. (2017)*). (B) Same as in (A) but with the data plotted on a logarithmic y-axis to highlight the exponential scaling that is expected for *E. coli*.

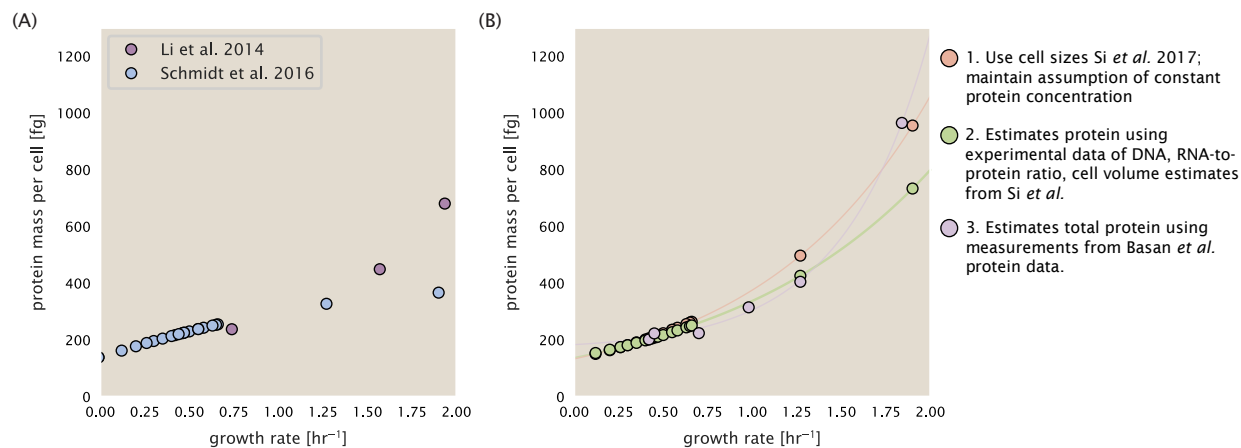


**Figure 18. Alternative estimates of total cellular protein for the growth conditions considered in Schmidt *et al.*** (A) The original protein mass from Schmidt *et al.* and Li *et al.* are shown in purple and blue, respectively. (B) Three alternative estimates of total protein per cell. 1. light red: Rescaling of total protein mass assuming a growth rate independent protein concentration and cell volumes estimated from Si *et al.* 2017. 2. light green: Rescaling of total protein mass using estimates of growth rate-dependent protein concentrations and cell volumes estimated from Si *et al.* 2017. Total protein per cell is calculated by assuming a 1.1 g/ml cellular mass density, 30% dry mass, with 90% of the dry mass corresponding to DNA, RNA, and protein (*Basan et al., 2015*). See Estimation of Total Protein Content per Cell for details on calculation. 3. light purple: Rescaling of total protein mass using the experimental measurements from Basan *et al.* 2015.

1087 **Effect of cell volume on reported absolute protein abundances**

1088 As noted in Experimental Details Behind Proteomic Data, the authors from the work in *Schmidt et al. (2016)*  
1089 calculated proteome-wide protein abundances by first determining absolute abundances of 41 pre-selected  
1090 proteins, which relied on adding synthetic heavy reference peptides into their protein samples at known abundance.  
1091 This absolute quantitation was performed in replicate for each growth condition. Separately, the authors also  
1092 performed a more conventional mass spectrometry measurement for samples from each growth condition,  
1093 which attempted to maximize the number of quantified proteins but only provided relative abundances based  
1094 on peptide intensities. Finally, using their 41 proteins with absolute abundances already determined, they then  
1095 created calibration curves with which to relate their relative intensity to absolute protein abundance for each  
1096 growth condition. This allowed them to estimate absolute protein abundance for all proteins detected in their  
1097 proteome-wide data set. Combined with their flow cytometry cell counts, they were then able to determine  
1098 absolute abundance of each protein detected on a per cell basis.

1099 While this approach provided absolute abundances, another necessary step to arrive at total cellular protein  
1100 was to account for any protein loss during their various protein extraction steps. Here the authors attempted  
1101 to determine total protein separately using a BCA protein assay. In personal communications, it was noted that  
1102 determining reasonable total protein abundances by BCA across their array of growth conditions was particularly  
1103 troublesome. Instead, they noted confidence in their total protein measurements for cells grown in M9 minimal  
1104 media + glucose and used this as a reference point with which to estimate the total protein for all other growth  
1105 conditions.

1106 For cells grown in M9 minimal media + glucose an average total mass of  $M_p = 240$  fg per cell was measured.  
1107 Using their reported cell volume, reported as  $V_{orig} = 2.84$  fl, a cellular protein concentration of  $[M_p]_{orig} = M_p/V_{orig} =$   
1108  $85$  fg/fl. Now, taking the assumption that cellular protein concentration is relatively independent of growth rate,  
1109 they could then estimate the total protein mass for all other growth conditions from,

$$M_{p\_i} = [M_p]_{orig} \cdot V_i \quad (8)$$

1110 where  $M_{p_i}$  represents the total protein mass per cell and  $V_i$  is the cell volume for each growth condition  $i$  as  
1111 measured in Volkmer and Heinemann, 2011. Here the thinking is that the values of  $M_{p_i}$  reflects the total cellular  
1112 protein for growth condition  $i$ , where any discrepancy from their absolute protein abundance is assumed to be due  
1113 to protein loss during sample preparation. The protein abundances from their absolute abundance measurements  
1114 noted above were therefore scaled to their estimates and are shown in Figure *Figure 18* (purple data points).

1115 If we instead consider the cell volumes predicted in the work of Si *et al.*, we again need to take growth in M9  
1116 minimal media + glucose as a reference with known total mass, but we can follow a similar approach to estimate  
1117 total protein mass for all other growth conditions. Letting  $V_{Si\_glu} = 0.6$  fl be the predicted cell volume, the cellular  
1118 protein concentration becomes  $[M_p]_{Si} = M_p/V_{Si\_glu} = 400$  fg/fl. The new total protein mass per cell can then be  
1119 calculated from,

$$M'_{p\_i} = [M_p]_{Si} \cdot V_{Si\_i} \quad (9)$$

1120 where  $M'_{p_i}$  is the new protein mass prediction, and  $V_{Si\_i}$  refers to the new volume prediction for each condition  $i$ ,  
1121 These are shown as red data points in Figure *Figure 18(B)*.

1122 **Relaxing assumption of constant protein concentration across growth conditions**

1123 We next relax the assumption that cellular protein concentration is constant and instead, attempt to estimate  
1124 it using experimental data. Here we use the estimation of total protein mass per cell detailed in Estimation of  
1125 Total Protein Content per Cell for all data points in the *Schmidt et al. (2016)* data set. The green data points in  
1126 *Figure 18(B)* show this prediction, and this represents the approach used to estimate total protein per cell for all  
1127 data sets.

1128 **Comparison with total protein measurements from Basan *et al.* 2015.**

1129 One of the challenges in our estimates in the preceding sections is the need to estimate protein concentration and  
1130 cell volumes. These are inherently difficult to measure accurately due to the small size of *E. coli*. Indeed, for all

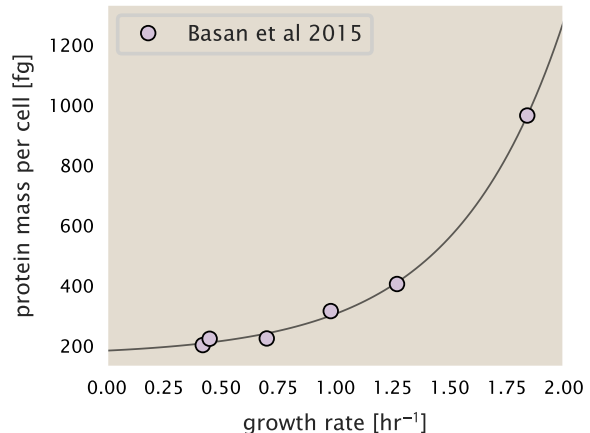


**Figure 19. Total cellular protein reported in Basan *et al.* 2015.** Measured protein mass as a function of growth rate as reproduced from Basan *et al.* 2015, with cells grown under different levels of nutrient limitation. The data was fit to an exponential curve where protein mass in fg per cell is given by  $14.65 e^{2.180 \cdot \lambda} + 172$  fg per cell, where  $\lambda$  is the growth rate in hr<sup>-1</sup>.

1131 the additional measurements of cell volume included in Figure *Figure 17*, no measurements were performed for  
 1132 cells growing at rates below 0.5 hr<sup>-1</sup>. It therefore remains to be determined whether our extrapolated cell volume  
 1133 estimates are appropriate, with the possibility that the logarithmic scaling of cell size might break down for slower  
 1134 growth.

1135 In our last approach we therefore attempt to estimate total protein using experimental data that required no  
 1136 estimates of concentration or cell volume. Specifically, in the work of Basan *et al.*, the authors measured total  
 1137 protein per cell for a broad range of growth rates (reproduced in Figure *Figure 19*). These were determined by  
 1138 first measuring bulk protein from cell lysate, measured by the colorimetric Biuret method (*You et al. (2013)*), and  
 1139 then abundance per cell was calculated from cell counts from either plating cells or a Coulter counter. While it  
 1140 is unclear why Schmidt *et al.* was unable to take a similar approach, the results from Basan *et al* appear more  
 1141 consistent with our expectation that cell mass will increase exponentially with faster growth rates. In addition,  
 1142 although they do not consider growth rates below about 0.5 hr<sup>-1</sup>, it is interesting to note that the protein mass per  
 1143 cell appears to plateau to a minimum value at slow growth. In contrast, our estimates using cell volume so far have  
 1144 predicted that total protein mass should continue to decrease slightly for slower growing cells. By fitting this data  
 1145 to an exponential function dependent on growth rate, we could then estimate the total protein per cell for each  
 1146 growth condition considered by Schmidt *et al.* (2016). These are plotted as red data points in *Figure 18(B)*.

### 1147 Calculation of Complex Abundance

1148 All protein data quantified the abundance of individual proteins per cell. However, this work requires estimates  
 1149 on the abundance of individual protein *complexes*, rather than the copy number of individual proteins. In our  
 1150 analysis of the protein copy number data, it became clear that the reported copy numbers do not always align  
 1151 with those based on reported stoichiometry. As one example of this, the F-O subunit of ATP synthase consists  
 1152 of three protein subunits with a stoichiometry of [AtpB][AtpF]<sub>2</sub>[AtpE]<sub>10</sub> (also referred to as subunits a, b, and c,  
 1153 respectively). In the experimental data of Schmidt *et al.* (2016), the values deviate from this quite substantially, with  
 1154 approximately 1000 AtpB, 9000 AtpF, and 300 AtpE reported per cell (minimal media + glucose growth condition).  
 1155 This highlights the technical challenges that still remain in our ability to quantify cellular composition, particularly  
 1156 for membrane-bound proteins like the ATP synthase complex considered here. In this section, we outline the  
 1157 approach we used to annotate proteins as part of each macromolecular complex and how we used averaging  
 1158 across the individual protein measurements to estimate an absolute complex abundances per cell.

1159 Protein complexes, and proteins individually, often have a variety of names, both longform and shorthand. As  
 1160 individual proteins can have a variety of different synonyms, we sought to ensure that each protein annotated  
 1161 in the data sets used the same synonym. To do use, we relied heavily on the EcoCyc Genomic Database (*Keseler*

1162 **et al., 2017**). Each protein in available data sets included an annotation of one of the gene name synonyms as  
1163 well as an accession ID – either a UniProt or Blattner "b-number". We programmatically matched up individual  
1164 accession IDs between the proteins in different data sets. In cases where accession IDs matched but the gene  
1165 names were different, we manually verified that the gene product was the same between the datasets and chose a  
1166 single synonym. All code used in the data cleaning and unification procedures can be found on the associated  
1167 [GitHub repository] (DOI:XXX) associated with this paper as well as on the associated [paper website](#).

1168 With each protein conforming to a single identification scheme, we then needed to identify the molecular  
1169 complexes each protein was a member of. Additionally, we needed to identify how many copies of each protein  
1170 were present in each complex (i.e. the subunit copy number) and compute the estimated abundance complex that  
1171 accounted for fluctuations in subunit stoichiometry. To map proteins to complexes, we accessed the EcoCyc *E.*  
1172 *coli* database **Keseler et al. (2017)** using PathwayTools version 23.0 **Karp et al. (2019)**. With a license for PathWay  
1173 Tools, we mapped each unique protein to its annotated complexes via the BioCyc Python package. As we mapped  
1174 each protein with *all* of its complex annotations, there was redundancy in the dataset. For example, ribosomal  
1175 protein L20 (RplT) is annotated to be a component of the 50S ribosome (EcoCyc complex CPLX-03962) as well as a  
1176 component of the mature 70S ribosome (EcoCyc complex CPLX-03964).

1177 In addition to the annotated complex, we collected information on the stoichiometry of each macromolecular  
1178 complex. For a complex with  $N_{\text{subunits}}$  protein species, for each protein subunit  $i$  we first calculate the number of  
1179 complexes that *could* be formed given the measured protein copy numbers per cell,

$$N_{\text{complex}}(\text{subunit } i) = \frac{P_{\text{subunit } i}^{(\text{measured})}}{m_{\text{subunit } i}}. \quad (10)$$

1180 Here,  $P_{\text{subunit } i}^{(\text{measured})}$  refers to the measured protein copy number of species  $i$ , and  $m$  refers to the number of monomers  
1181 present for that protein in the complex. For example, the 70S mature ribosome complex has 55 protein components,  
1182 all of which are present in a single copy except L4 (RplL), which is present in 4 copies ( $m = 4$ ). For each ribosomal  
1183 protein, we then calculate the maximum number of complexes that could be formed using **Equation 10**. This  
1184 example, along with example from 5 other macromolecular complexes, can be seen in **Figure 20**.

1185 It is important to note that measurement noise, efficiency of protein extraction, and differences in protein  
1186 stability will mean that the precise value of each calculation will be different for each component of a given complex.  
1187 Thus, to report the total complex abundance, we use the arithmetic mean of across all subunits in the complex,

$$\langle N_{\text{complex}} \rangle = \frac{1}{N_{\text{subunits}}} \sum_i^{N_{\text{subunits}}} \frac{P_i^{(\text{measured})}}{m_{\text{subunit } i}}. \quad (11)$$

1188 in **Figure 20**, we show this mean value as a grey line for a variety of different complexes. Additionally, we have built  
1189 an interactive figure accessible on the [paper website](#) where the validity of this approach can be examined for any  
1190 complex with more than two subunits (thus, excluding monomers and dimers).

## 1191 Extending Estimates to a Continuum of Growth Rates

1192 In the main text, we considered a standard stopwatch of 5000 s to estimate the abundance of the various protein  
1193 complexes considered. In addition to point estimates, we also showed the estimate as a function of growth rate as  
1194 transparent grey curves. In this section, we elaborate on this continuum estimate, giving examples of estimates  
1195 that scale with either cell volume, cell surface area, or number of origins of replication.

## 1196 Estimation of the total cell mass

1197 For many of the processes estimated in the main text we relied on a cellular dry mass of  $\approx 300$  fg from which we  
1198 computed elemental and protein fractions using knowledge of fractional composition of the dry mass. At modest  
1199 growth rates, such as the 5000 s doubling time used in the main text, this is a reasonable number to use as the  
1200 typical cell mass is  $\approx 1$  pg and *E. coli* cells can approximated as 70% water by volume. However, as we have shown  
1201 in the preceding sections, the cell size is highly dependent on the growth rate. This means that a dry mass of 300 fg  
1202 cannot be used reliably across all growth rates.

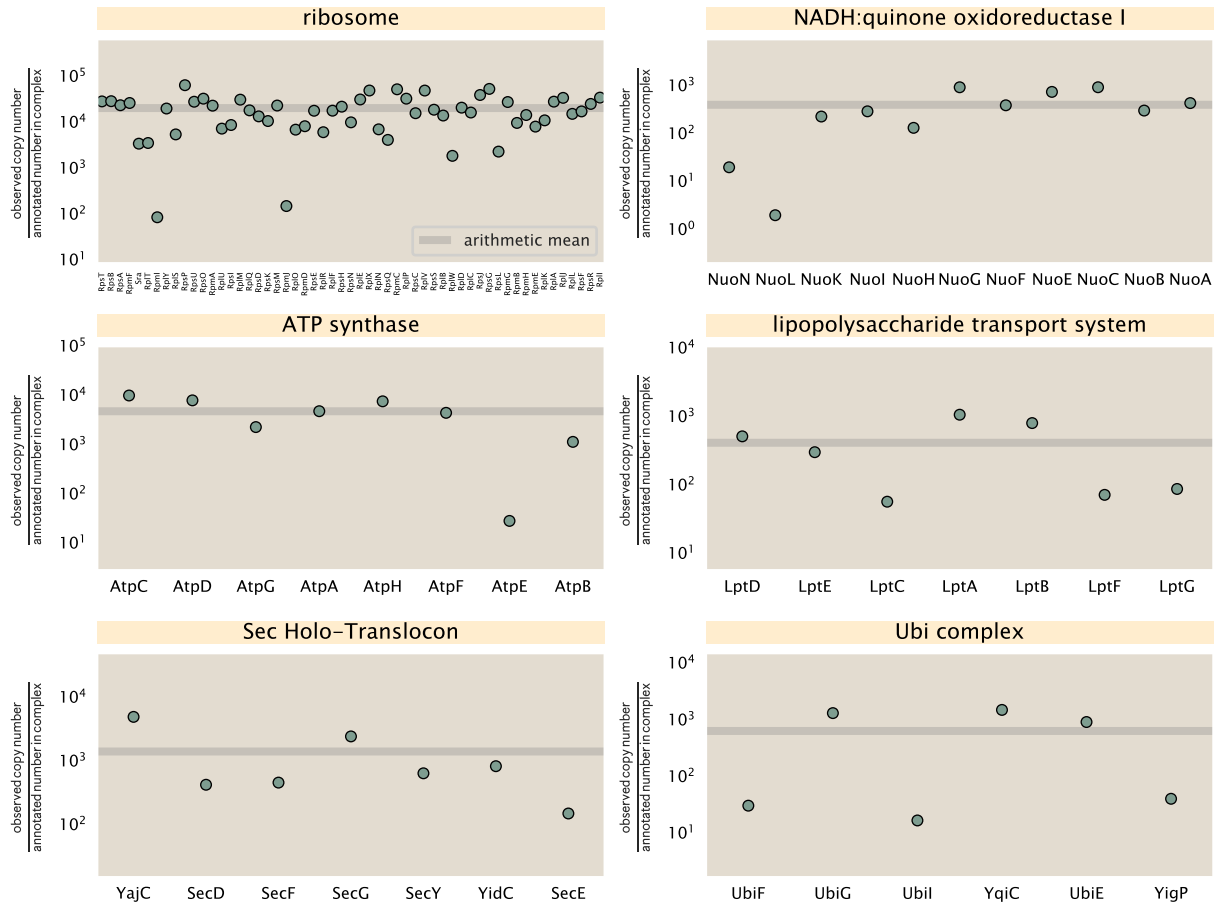


**Figure 20. Calculation of the mean complex abundance from measurements of single subunits.** Six of the largest complexes (by number of subunits) in *E. coli*. Points correspond to the maximum number of complexes that can be formed given measurement of that individual protein. Solid grey line corresponds to the arithmetic mean across all subunits. These data correspond to measurements from *Schmidt et al. (2016)* in a glucose-supplemented minimal growth medium.

1203 Rather, using the phenomenological description of cell volume scaling exponentially with growth rate, and  
 1204 using a rule-of-thumb of a cell buoyant density of  $\approx 1.1 \text{ pg} / \text{fL}$  (BNID: 103875), we can calculate the cell dry mass  
 1205 across a range of physiological growth rates as

$$m_{\text{cell}} \approx \rho V(\lambda) \approx \rho a e^{\lambda * b} \quad (12)$$

1206 where  $a$  and  $b$  are constants with units of  $\mu\text{m}^3$  and hr, respectively. The value of these constants can be estimated  
 1207 from the careful volume measurements performed by *Si et al. (2017,?)*, as considered in Appendix Estimation of  
 1208 Cell Size and Surface Area earlier.

### 1209 Complex Abundance Scaling With Cell Volume

1210 Several of the estimates performed in the main text are implicitly dependent on the cell volume. This includes  
 1211 processes such as ATP utilization and, most prominently, the transport of nutrients, whose demand will be  
 1212 proportional to the volume of the cell. Of the latter, we estimated the number of transporters that would be  
 1213 needed to shuttle enough carbon, phosphorus, and sulfur across the membrane to build new cell mass. To do so,  
 1214 we used elemental composition measurements combined with a 300 fg cell dry mass to make the point estimate.  
 1215 As we now have a means to estimate the total cell mass as a function of volume, we can generalize these estimates  
 1216 across growth rates.

1217 Rather than discussing the particular details of each transport system, we will derive this scaling expression in  
 1218 very general terms. Consider that we wish to estimate the number of transporters for some substance  $X$ , which  
 1219 has been measured to be made up some fraction of the dry mass,  $\theta_X$ . If we assume that, irrespective of growth  
 1220 rate, the cell dry mass is relatively constant (*Basan et al., 2015*) and  $\approx 30\%$  of the total cell mass, we can state that  
 1221 the total mass of substance  $X$  as a function of growth rate is

$$m_X \approx 0.3 \times \rho V(\lambda) \theta_X, \quad (13)$$

1222 where we have used  $\rho V(\lambda)$  as an estimate of the total cell mass, defined in *Equation 12*. To convert this to the  
 1223 number of units  $N_X$  of substance  $X$  in the cell, we can use the formula weight  $w_X$  of a single unit of  $X$  in conjunction  
 1224 with *Equation 13*,

$$N_X \approx \frac{m_X}{w_X}. \quad (14)$$

1225 To estimate the number of transporters needed, we make the approximation that loss of units of  $X$  via diffusion  
 1226 through porins or due to the permeability of the membrane is negligible and that a single transporter complex  
 1227 can transport substance  $X$  at a rate  $r_X$ . As this rate  $r_X$  is in units of  $X$  per time per transporter, we must provide  
 1228 a time window over which the transport process can occur. This is related to the cell doubling time  $\tau$ , which can  
 1229 be calculated from the the growth rate  $\lambda$  as  $\tau = \log(2)/\lambda$ . Putting everything together, we arrive at a generalized  
 1230 transport scaling relation of

$$N_{\text{transporters}}(\lambda) = \frac{0.3 \times \rho V(\lambda) \theta_X}{w_X r_X \tau}. \quad (15)$$

1231 This function is used to draw the continuum estimates for the number of transporters seen in Figures 2 and  
 1232 3 as transparent grey curves. Occasionally, this continuum scaling relationship will not precisely agree with the  
 1233 point estimate outlined in the main text. This is due to the choice of  $\approx 300 \text{ fg}$  total dry mass per cell for the point  
 1234 estimate, whereas we considered more precise values of cell mass in the continuum estimate. We note, however,  
 1235 that both this scaling relation and the point estimates are meant to describe the order-of-magnitude observed,  
 1236 and not the predict the exact values of the abundances.

1237 *Equation 15* is a very general relation for processes where the cell volume is the "natural variable" of the  
 1238 problem. This means that, as the cell increases in volume, the requirements for substance  $X$  also scale with  
 1239 volume rather than scaling with surface area, for example. So long as the rate of the process, the fraction of the  
 1240 dry mass attributable to the substance, and the formula mass of the substance is known, *Equation 15* can be used  
 1241 to compute the number of complexes needed. For example, to compute the number of ATP synthases per cell,  
 1242 *Equation 15* can be slightly modified to the form

$$N_{\text{ATP synthases}}(\lambda) = \frac{0.3 \times \rho V(\lambda) \theta_{\text{protein}} N_{\text{ATP}}}{w_{AA} r_{\text{ATP}} \tau}, \quad (16)$$

1243 where we have included the term  $N_{ATP}$  to account for the number of ATP equivalents needed per amino acid for  
 1244 translation ( $\approx 4$ , BNID: 114971), and  $w_{AA}$  is the average mass of an amino acid. The grey curves in Figure 4 of the  
 1245 main text were made using this type of expression.

## 1246 A Relation for Complex Abundance Scaling With Surface Area

1247 In our estimation for the number of complexes needed for lipid synthesis and peptidoglycan maturation, we used  
 1248 a particular estimate for the cell surface area ( $\approx 5 \mu m$ , BNID: 101792) and the fraction of dry mass attributable to  
 1249 peptidoglycan ( $\approx 3\%$ , BNID: 101936). Both of these values come from glucose-fed *E. coli* in balanced growth. As we  
 1250 are interested in describing the scaling as a function of the growth rate, we must also consider how these values  
 1251 scale with cell surface area, which is the natural variable for these types of processes. In the coming paragraphs,  
 1252 we highlight how we incorporate a condition-dependent surface area into our calculation of the number of lipids  
 1253 and murein monomers that need to be synthesized and crosslinked, respectively.

### 1254 Number of Lipids

1255 To compute the number of lipids as a function of growth rate, we make the assumption that some features, such as  
 1256 the surface area of a single lipid ( $A_{lipid} \approx 0.5 \text{ nm}^2$ , BNID: 106993) and the total fraction of the membrane composed  
 1257 of lipids ( $\approx 40\%$ , BNID: 100078) are independent of the growth rate. Using these approximations combined with  
 1258 **Equation 6**, and recognizing that each membrane is composed of two leaflets, we can compute the number of  
 1259 lipids as a function of growth rate as

$$N_{lipids}(\lambda) \approx \frac{4 \text{ leaflets} \times 0.4 \times \eta \pi \left( \frac{\eta \pi}{4} - \frac{\pi}{12} \right)^{-2/3} V(\lambda)^{2/3}}{A_{lipid}} \quad (17)$$

1260 where  $\eta$  is the length-to-width aspect ratio and  $V$  is the cell volume.

### 1261 Number of Murein Monomers

1262 In calculation of the number of transpeptidases needed for maturation of the peptidoglycan, we used an empirical  
 1263 measurement that  $\approx 3\%$  of the dry mass is attributable to peptidoglycan and that a single murien monomer is  
 1264  $m_{murein} \approx 1000 \text{ Da}$ . While the latter is independent of growth rate, the former is not. As the peptidoglycan exists as  
 1265 a thin shell with a width of  $w \approx 10 \text{ nm}$  encapsulating the cell, one would expect the number of murein monomers  
 1266 scales with the surface area of this shell. In a similar spirit to our calculation of the number of lipids, the total  
 1267 number of murein monomers as a function of growth rate can be calculated as

$$N_{murein \text{ monomers}}(\lambda) \approx \frac{\rho_{pg} w \eta \pi \left( \frac{\eta \pi}{4} - \frac{\pi}{12} \right)^{-2/3} V(\lambda)^{2/3}}{m_{murein}}, \quad (18)$$

1268 where  $\rho_{pg}$  is the density of peptidoglycan.

## 1269 Complex Abundance Scaling With Number of Origins, and rRNA Synthesis

1270 While the majority of our estimates hinge on the total cell volume or surface area, processes related to the central  
 1271 dogma, namely DNA replication and synthesis of rRNA, depend on the number of chromosomes present in the  
 1272 cell. As discussed in the main text, the ability of *E. coli* to parallelize the replication of its chromosome by having  
 1273 multiple active origins of replication is critical to synthesize enough rRNA, especially at fast growth rates. Derived in  
 1274 *Si et al. (2017)* and reproduced in the main text and Appendix Estimation of  $\langle \#ori \rangle / \langle \#ter \rangle$  and  $\langle \#ori \rangle$  below, the  
 1275 average number of origins of replication at a given growth rate can be calculated as

$$\langle \#ori \rangle \approx 2^{t_{cyc} \lambda / \ln 2} \quad (19)$$

1276 where  $t_{cyc}$  is the total time of replication and division. We can make the approximation that  $t_{cyc} \approx 70 \text{ min}$ , which is  
 1277 the time from the initiation of chromosomal replication until division. This time corresponds to the sum of the  
 1278 so-called C and D periods of the cell cycle, which correspond to the time it takes to replicate the entire chromosome  
 1279 (C period) and the time from completion to eventual division (D period) *Helmstetter and Cooper (1968)*.

1280 In the case of rRNA synthesis, the majority of the rRNA operons are surrounding the origin of replication. Thus,  
1281 at a given growth rate  $\lambda$ , the average dosage of rRNA operons per cell  $D_{\text{rRNA}}$  is

$$D_{\text{rRNA}}(\lambda) \approx N_{\text{rRNA operons}} \times 2^{t_{\text{cyc}}\lambda/\ln 2}. \quad (20)$$

1282 This makes the approximation that *all* rRNA operons are localized around the origin. In reality, the operons are  
1283 some distance away from the origin, making **Equation 20** an approximation (*Dennis et al., 2004*).

1284 In the main text, we stated that at a growth rate of  $0.5 \text{ hr}^{-1}$ , there is  $\approx 1$  chromosome per cell. While a fair  
1285 approximation, **Equation 19** illustrates that is not precisely true, even at slow growth rates. In estimating the  
1286 number of RNA polymerases as a function of growth rate, we consider that regardless of the number of rRNA  
1287 operons, they are all sufficiently loaded with RNA polymerase such that each operon produces one rRNA per  
1288 second. Thus, the total number of RNA polymerase as a function of the growth rate can be calculated as

$$N_{\text{RNA polymerase}}(\lambda) \approx L_{\text{operon}} D_{\text{rRNA}} \rho_{\text{RNA polymerase}}, \quad (21)$$

1289 where  $L_{\text{operon}}$  is the total length of an rRNA operon ( $\approx 4500 \text{ bp}$ ) and  $\rho_{\text{RNA polymerase}}$  is packing density of RNA  
1290 polymerase on a given operon, taken to be 1 RNA polymerase per 80 nucleotides.

### 1291 Calculation of active ribosomal fraction.

1292 In the main text we used the active ribosomal fraction  $f_a$  that was reported in the work of *Dai et al. (2016)* to  
1293 estimate the active ribosomal mass fraction  $\Phi_R \times f_a$  across growth conditions. We lacked any specific model to  
1294 consider how  $f_a$  should vary with growth rate, and instead find that the data is well-approximated by fitting to an  
1295 exponential curve ( $f_a = -0.889 e^{4.6\lambda} + 0.922$ ; dashed line in inset of **Figure 9(C)**). We use this function to estimate  $f_a$   
1296 for each of the data points shown in **Figure 9(C)**.

### 1297 Estimation of $\langle \# \text{ori} \rangle / \langle \# \text{ter} \rangle$ and $\langle \# \text{ori} \rangle$ .

1298 *E. coli* shows robust scaling of cell size with the average number of origins per cell,  $\langle \# \text{ori} \rangle$  (*Si et al., 2017*). Since  
1299 protein makes up a majority of the cell's dry mass, the change in cell size is also a reflection of the changes in  
1300 proteomic composition and total abundance across growth conditions. Given the potential constraints on rRNA  
1301 synthesis and changes in ribosomal copy number with  $\langle \# \text{ori} \rangle$ , it becomes important to also consider how protein  
1302 copy numbers vary with the state of chromosomal replication. This is particularly true when trying to make sense of  
1303 the changes in ribosomal fraction and growth-rate dependent changes in proteomic composition at a mechanistic  
1304 level. As considered in the main text, it is becoming increasingly apparent that regulation through the secondary  
1305 messengers (p)ppGpp may act to limit DNA replication and also reduce ribosomal activity in poorer nutrient  
1306 conditions. In this context, both  $\langle \# \text{ori} \rangle$ , as well as the  $\langle \# \text{ori} \rangle / \langle \# \text{ter} \rangle$  ratio become important parameters to consider  
1307 and keep track of. An increase in  $\langle \# \text{ori} \rangle / \langle \# \text{ter} \rangle$  ratio in particular, causes a relatively higher gene dosage in rRNA  
1308 and r-protein genes due to skew in genes near the origin, where the majority of these are located

1309 In the main text we estimated the change in  $\langle \# \text{ori} \rangle$  with growth rate using the nutrient-limited wild-type cell  
1310 data from *Si et al. (2017)*. We consider their measurements of DNA replication time ( $t_C$ , 'C' period of cell division),  
1311 total cell cycle time ( $t_{\text{cyc}}$ , 'C' + 'D' period of cell division), and doubling time  $\tau$  from wild-type *E. coli* growing across  
1312 a range of growth conditions. Here we show how we estimate this parameter, as well as the  $\langle \# \text{ori} \rangle / \langle \# \text{ter} \rangle$  ratio  
1313 from their data. We begin by considering  $\langle \# \text{ori} \rangle$ . If the cell cycle time takes longer than the time of cell division, the  
1314 cell will need to initiate DNA replication more often than its rate of division,  $2^{\lambda t} = 2^{\ln(2)\cdot t/\tau}$  to maintain steady state  
1315 growth. Cells will need to do this in proportion to the ratio  $\lambda_{\text{cyc}}/\lambda = t_{\text{cyc}}/\tau$ , and the number of origins per cell (on  
1316 average) is then given by  $2^{t_{\text{cyc}}/\tau}$ . The average number of termini will in contrast depend on the lag time between  
1317 DNA replication and cell division,  $t_D$ , with  $\langle \# \text{ori} \rangle / \langle \# \text{ter} \rangle$  ratio =  $2^{t_{\text{cyc}}/\tau - t_D/\tau} = 2^{t_C/\tau}$ .

1318 In Figure 21(A) and (B) we plot the measured  $t_C$  and  $t_{\text{cyc}}$  values versus the doubling time from *Si et al. (2017)*.  
1319 The authors estimated  $t_C$  by marker frequency analysis using qPCR, while  $t_{\text{cyc}} = t_C + t_D$  were inferred from  $t_C$  and  
1320  $\tau$ . In the plots we see that both  $t_C$  and  $t_{\text{cyc}}$  reach a minimum at around 40 and 75 minutes, respectively. For a C  
1321 period of 40 minutes, this would correspond to a maximum rate of elongation of about 1,000 bp/sec. Since we  
1322 lacked a specific model to describe how each of these parameters vary with growth condition, we assumed that  
1323 they were linearly dependent on the doubling time. For each parameter,  $t_C$  and  $t_{\text{cyc}}$ , we split them up into two

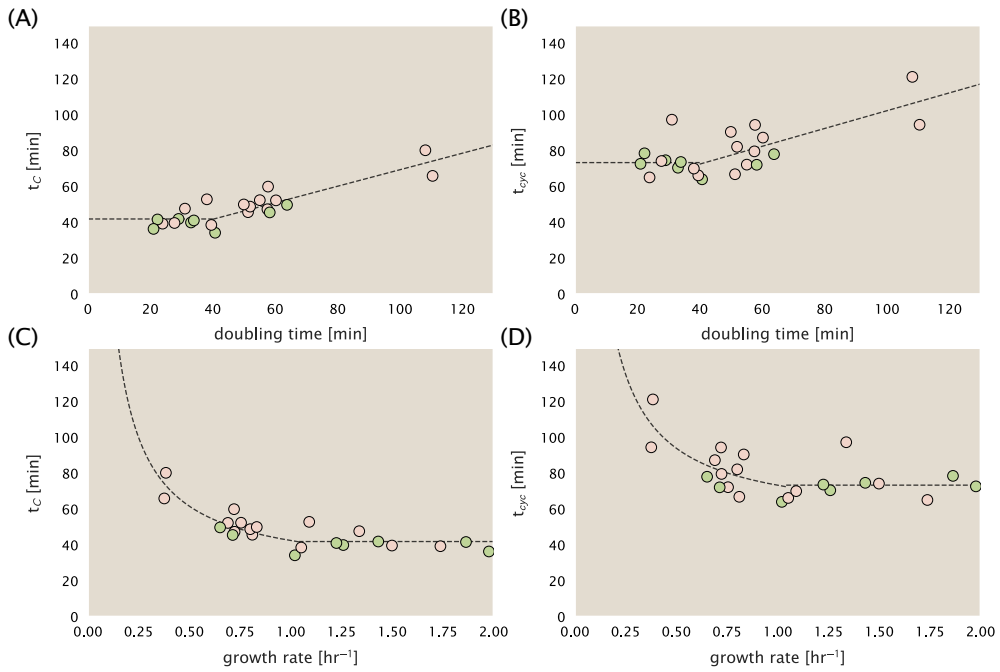


**Figure 21. Estimation of  $\langle \# \text{ori} \rangle / \langle \# \text{ter} \rangle$  and  $\langle \# \text{ori} \rangle$  using data from Si et al. (2017).** (A) and (B) plot the reported  $t_C$  and  $t_{cyc}$  as a function of cell doubling time  $\tau$ , respectively. The dashed lines show a piecewise fit to the data. For short doubling times (rich media),  $t_C$  and  $t_{cyc}$  are assumed constant ( $t_C = 42$  minutes,  $t_{cyc} = 73$  minutes). At the transition, taken to occur at 40 minutes, the dashed line corresponds to an assumed proportional increase in each parameter as a function of the doubling time ( $t_C = 0.46 \tau + 23.3$  minutes,  $t_{cyc} = 0.50 \tau + 52.7$  minutes). (C) and (D) plot the same data as in (A) and (B), but as a function of growth rate, given by  $\lambda = \ln(2)/\tau$ .

1324 domains corresponding to poorer nutrient conditions and rich nutrient conditions (cut off at  $\tau \approx 40$  minutes where  
 1325 chromosomal replication becomes nearly constant). The fit lines are shown as solid black lines. In Figure 21(C) and  
 1326 (D) we also show  $t_C$  and  $t_{cyc}$  as a function of growth rate  $\lambda$  along with our piecewise linear fits, which match the  
 1327 plots in the main text.

1328 **References**

- 1329 Abelson, H., Johnson, L., Penman, S., and Green, H. (1974). Changes in RNA in relation to growth of the fibroblast: II. The lifetime  
1330 of mRNA, rRNA, and tRNA in resting and growing cells. *Cell*, 1(4):161–165.
- 1331 Aidelberg, G., Towbin, B. D., Rothschild, D., Dekel, E., Bren, A., and Alon, U. (2014). Hierarchy of non-glucose sugars in *Escherichia*  
1332 *coli*. *BMC Systems Biology*, 8(1):133.
- 1333 Antonenko, Y. N., Pohl, P., and Denisov, G. A. (1997). Permeation of ammonia across bilayer lipid membranes studied by  
1334 ammonium ion selective microelectrodes. *Biophysical Journal*, 72(5):2187–2195.
- 1335 Ashburner, M., Ball, C. A., Blake, J. A., Botstein, D., Butler, H., Cherry, J. M., Davis, A. P., Dolinski, K., Dwight, S. S., Eppig, J. T., Harris,  
1336 M. A., Hill, D. P., Issel-Tarver, L., Kasarskis, A., Lewis, S., Mateescu, J. C., Richardson, J. E., Ringwald, M., Rubin, G. M., and Sherlock, G.  
1337 (2000). Gene Ontology: tool for the unification of biology. *Nature Genetics*, 25(1):25–29.
- 1338 Ason, B., Bertram, J. G., Hingorani, M. M., Beechem, J. M., O'Donnell, M., Goodman, M. F., and Bloom, L. B. (2000). A Model  
1339 for *Escherichia coli* DNA Polymerase III Holoenzyme Assembly at Primer/Template Ends: DNA Triggers A Change In Binding  
1340 Specificity of the  $\gamma$  Complex Clamp Loader. *Journal of Biological Chemistry*, 275(4):3006–3015.
- 1341 Assentoft, M., Kaptan, S., Schneider, H.-P., Deitmer, J. W., de Groot, B. L., and MacAulay, N. (2016). Aquaporin 4 as a  $\text{NH}_3$  Channel.  
1342 *Journal of Biological Chemistry*, 291(36):19184–19195.
- 1343 Baba, T., Ara, T., Hasegawa, M., Takai, Y., Okumura, Y., Baba, M., Datsenko, K. A., Tomita, M., Wanner, B. L., and Mori, H. (2006).  
1344 Construction of *Escherichia coli*K-12 in-frame, single-gene knockout mutants: the Keio collection. *Molecular Systems Biology*,  
1345 2(1):2460.
- 1346 Basan, M., Zhu, M., Dai, X., Warren, M., Sévin, D., Wang, Y.-P., and Hwa, T. (2015). Inflating bacterial cells by increased protein  
1347 synthesis. *Molecular Systems Biology*, 11(10):836.
- 1348 Bauer, S. and Ziv, E. (1976). Dense growth of aerobic bacteria in a bench-scale fermentor. *Biotechnology and Bioengineering*,  
1349 18(1):81–94. \_eprint: <https://onlinelibrary.wiley.com/doi/pdf/10.1002/bit.260180107>.
- 1350 Belliveau, N. M., Barnes, S. L., Ireland, W. T., Jones, D. L., Sweredoski, M. J., Moradian, A., Hess, S., Kinney, J. B., and Phillips, R.  
1351 (2018). Systematic approach for dissecting the molecular mechanisms of transcriptional regulation in bacteria. *Proceedings of  
1352 the National Academy of Sciences*, 115(21):E4796–E4805.
- 1353 Booth, I. R., Mitchell, W. J., and Hamilton, W. A. (1979). Quantitative analysis of proton-linked transport systems. The lactose  
1354 permease of *Escherichia coli*. *Biochemical Journal*, 182(3):687–696.
- 1355 Bremer, H. and Dennis, P. P. (2008). Modulation of Chemical Composition and Other Parameters of the Cell at Different Exponential  
1356 Growth Rates. *EcoSal Plus*, 3(1).
- 1357 Browning, D. F. and Busby, S. J. W. (2016). Local and global regulation of transcription initiation in bacteria. *Nature Reviews  
1358 Microbiology*, 14(10):638–650.
- 1359 Büke, F., Grilli, J., Lagomarsino, M. C., Bokinsky, G., and Tans, S. (2020). ppGpp is a bacterial cell size regulator. *bioRxiv*,  
1360 266:2020.06.16.154187.
- 1361 Catherwood, A. C., Lloyd, A. J., Tod, J. A., Chauhan, S., Slade, S. E., Walkowiak, G. P., Galley, N. F., Punekar, A. S., Smart, K., Rea, D.,  
1362 Evans, N. D., Chappell, M. J., Roper, D. I., and Dowson, C. G. (2020). Substrate and Stereochemical Control of Peptidoglycan  
1363 Cross-Linking by Transpeptidation by *Escherichia coli* PBP1B. *Journal of the American Chemical Society*, 142(11):5034–5048.
- 1364 Cox, G. B., Newton, N. A., Gibson, F., Snoswell, A. M., and Hamilton, J. A. (1970). The function of ubiquinone in *Escherichia coli*.  
1365 *Biochemical Journal*, 117(3):551–562.
- 1366 Dai, X., Zhu, M., Warren, M., Balakrishnan, R., Okano, H., Williamson, J. R., Fredrick, K., and Hwa, T. (2018). Slowdown of Translational  
1367 Elongation in *Escherichia coli* under Hyperosmotic Stress. - PubMed - NCBI. *mBio*, 9(1):281.
- 1368 Dai, X., Zhu, M., Warren, M., Balakrishnan, R., Patsalo, V., Okano, H., Williamson, J. R., Fredrick, K., Wang, Y.-P., and Hwa, T.  
1369 (2016). Reduction of translating ribosomes enables *Escherichia coli* to maintain elongation rates during slow growth. *Nature  
1370 Microbiology*, 2(2):16231.
- 1371 Datsenko, K. A. and Wanner, B. L. (2000). One-step inactivation of chromosomal genes in *Escherichia coli* K-12 using PCR products.  
1372 *Proceedings of the National Academy of Sciences*, 97(12):6640–6645.
- 1373 Dennis, P. P., Ehrenberg, M., and Bremer, H. (2004). Control of rRNA Synthesis in *Escherichia coli*: a Systems Biology Approach.  
1374 *Microbiology and Molecular Biology Reviews*, 68(4):639–668.

- 1375 Dill, K. A., Ghosh, K., and Schmit, J. D. (2011). Physical limits of cells and proteomes. *Proceedings of the National Academy of Sciences*,  
1376 108(44):17876–17882.
- 1377 Erickson, D. W., Schink, S. J., Patsalo, V., Williamson, J. R., Gerland, U., and Hwa, T. (2017). A global resource allocation strategy  
1378 governs growth transition kinetics of *Escherichia coli*. *Nature*, 551(7678):119–123.
- 1379 Escalante, A., Salinas Cervantes, A., Gosset, G., and Bolívar, F. (2012). Current knowledge of the *Escherichia coli* phosphoenolpyru-  
1380 vate–carbohydrate phosphotransferase system: Peculiarities of regulation and impact on growth and product formation.  
1381 *Applied Microbiology and Biotechnology*, 94(6):1483–1494.
- 1382 Feist, A. M., Henry, C. S., Reed, J. L., Krummenacker, M., Joyce, A. R., Karp, P. D., Broadbelt, L. J., Hatzimanikatis, V., and Palsson,  
1383 B. Ø. (2007). A genome-scale metabolic reconstruction for *Escherichia coli* K-12 MG1655 that accounts for 1260 ORFs and  
1384 thermodynamic information. *Molecular Systems Biology*, 3(1):121.
- 1385 Fernández-Coll, L., Maciąg-Dorszynska, M., Tailor, K., Vadia, S., Levin, P. A., Szalewska-Palasz, A., Cashel, M., and Dunny, G. M.  
1386 (2020). The Absence of (p)ppGpp Renders Initiation of *Escherichia coli* Chromosomal DNA Synthesis Independent of Growth  
1387 Rates. *mBio*, 11(2):45.
- 1388 Fijalkowska, I. J., Schaaper, R. M., and Jonczyk, P. (2012). DNA replication fidelity in *Escherichia coli*: A multi-DNA polymerase affair.  
1389 *FEMS Microbiology Reviews*, 36(6):1105–1121.
- 1390 Finkelstein, I. J. and Greene, E. C. (2013). Molecular Traffic Jams on DNA. *Annual Review of Biophysics*, 42(1):241–263.
- 1391 Gallagher, L. A., Bailey, J., and Manoil, C. (2020). Ranking essential bacterial processes by speed of mutant death. *Proceedings of  
1392 the National Academy of Sciences*.
- 1393 Gama-Castro, S., Salgado, H., Santos-Zavaleta, A., Ledezma-Tejeida, D., Muñiz-Rascado, L., García-Sotelo, J. S., Alquicira-Hernández,  
1394 K., Martínez-Flores, I., Pannier, L., Castro-Mondragón, J. A., Medina-Rivera, A., Solano-Lira, H., Bonavides-Martínez, C., Pérez-  
1395 Rueda, E., Alquicira-Hernández, S., Porrón-Sotelo, L., López-Fuentes, A., Hernández-Koutoucheva, A., Moral-Chávez, V. D.,  
1396 Rinaldi, F., and Collado-Vides, J. (2016). RegulonDB version 9.0: High-level integration of gene regulation, coexpression, motif  
1397 clustering and beyond. *Nucleic Acids Research*, 44(D1):D133–D143.
- 1398 Ge, J., Yu, G., Ator, M. A., and Stubbe, J. (2003). Pre-Steady-State and Steady-State Kinetic Analysis of *E. coli* Class I Ribonucleotide  
1399 Reductase. *Biochemistry*, 42(34):10071–10083.
- 1400 Godin, M., Delgado, F. F., Son, S., Grover, W. H., Bryan, A. K., Tzur, A., Jorgensen, P., Payer, K., Grossman, A. D., Kirschner, M. W., and  
1401 Manalis, S. R. (2010). Using buoyant mass to measure the growth of single cells. *Nature Methods*, 7(5):387–390.
- 1402 Guo, Y., Li, D., Zhang, S., Yang, Y., Liu, J.-J., Wang, X., Liu, C., Milkie, D. E., Moore, R. P., Tulu, U. S., Kiehart, D. P., Hu, J., Lippincott-  
1403 Schwartz, J., Betzig, E., and Li, D. (2018). Visualizing Intracellular Organelle and Cytoskeletal Interactions at Nanoscale Resolution  
1404 on Millisecond Timescales. *Cell*, 175(5):1430–1442.e17.
- 1405 Harris, L. K. and Theriot, J. A. (2018). Surface Area to Volume Ratio: A Natural Variable for Bacterial Morphogenesis. *Trends in  
1406 microbiology*, 26(10):815–832.
- 1407 Harris, R. M., Webb, D. C., Howitt, S. M., and Cox, G. B. (2001). Characterization of PitA and PitB from *Escherichia coli*. *Journal of  
1408 Bacteriology*, 183(17):5008–5014.
- 1409 Hauriyliuk, V., Atkinson, G. C., Murakami, K. S., Tenson, T., and Gerdes, K. (2015). Recent functional insights into the role of  
1410 (p)ppGpp in bacterial physiology. *Nature Reviews Microbiology*, 13(5):298–309.
- 1411 Heldal, M., Norland, S., and Tumyr, O. (1985). X-ray microanalytic method for measurement of dry matter and elemental content  
1412 of individual bacteria. *Applied and Environmental Microbiology*, 50(5):1251–1257.
- 1413 Helmstetter, C. E. and Cooper, S. (1968). DNA synthesis during the division cycle of rapidly growing *Escherichia coli* Br. *Journal of  
1414 Molecular Biology*, 31(3):507–518.
- 1415 Henkel, S. G., Beek, A. T., Steinsiek, S., Stagge, S., Bettenbrock, K., de Mattos, M. J. T., Sauter, T., Sawodny, O., and Ederer, M. (2014).  
1416 Basic Regulatory Principles of *Escherichia coli*'s Electron Transport Chain for Varying Oxygen Conditions. *PLoS ONE*, 9(9):e107640.
- 1417 Hui, S., Silverman, J. M., Chen, S. S., Erickson, D. W., Basan, M., Wang, J., Hwa, T., and Williamson, J. R. (2015). Quantitative proteomic  
1418 analysis reveals a simple strategy of global resource allocation in bacteria. *Molecular Systems Biology*, 11(2):e784–e784.
- 1419 Ingledew, W. J. and Poole, R. K. (1984). The respiratory chains of *Escherichia coli*. *Microbiological Reviews*, 48(3):222–271.
- 1420 Ireland, W. T., Beeler, S. M., Flores-Bautista, E., Belliveau, N. M., Sweredoski, M. J., Moradian, A., Kinney, J. B., and Phillips, R. (2020).  
1421 Deciphering the regulatory genome of *Escherichia coli*, one hundred promoters at a time. *bioRxiv*.

- 1422 Jensen, R. B., Wang, S. C., and Shapiro, L. (2001). A moving DNA replication factory in *Caulobacter crescentus*. *The EMBO journal*,  
1423 20(17):4952–4963.
- 1424 Jun, S., Si, F., Pugatch, R., and Scott, M. (2018). Fundamental principles in bacterial physiology - history, recent progress, and the  
1425 future with focus on cell size control: A review. *Reports on Progress in Physics*, 81(5):056601.
- 1426 Karp, P. D., Billington, R., Caspi, R., Fulcher, C. A., Latendresse, M., Kothari, A., Keseler, I. M., Krummenacker, M., Midford, P. E., Ong,  
1427 Q., Ong, W. K., Paley, S. M., and Subhraveti, P. (2019). The BioCyc collection of microbial genomes and metabolic pathways.  
1428 *Briefings in Bioinformatics*, 20(4):1085–1093.
- 1429 Karr, J. R., Sanghvi, J. C., Macklin, D. N., Gutschow, M. V., Jacobs, J. M., Bolival, B., Assad-Garcia, N., Glass, J. I., and Covert, M. W.  
1430 (2012). A Whole-Cell Computational Model Predicts Phenotype from Genotype. *Cell*, 150(2):389–401.
- 1431 Keseler, I. M., Mackie, A., Santos-Zavaleta, A., Billington, R., Bonavides-Martínez, C., Caspi, R., Fulcher, C., Gama-Castro, S., Kothari,  
1432 A., Krummenacker, M., Latendresse, M., Muñiz-Rascado, L., Ong, Q., Paley, S., Peralta-Gil, M., Subhraveti, P., Velázquez-Ramírez,  
1433 D. A., Weaver, D., Collado-Vides, J., Paulsen, I., and Karp, P. D. (2017). The EcoCyc database: reflecting new knowledge about  
1434 Escherichia coliK-12. *Nucleic Acids Research*, 45(D1):D543–D550.
- 1435 Khademi, S., O'Connell, J., Remis, J., Robles-Colmenares, Y., Miercke, L. J. W., and Stroud, R. M. (2004). Mechanism of Ammonia  
1436 Transport by Amt/MEP/Rh: Structure of AmtB at 1.35 Å. *Science*, 305(5690):1587–1594.
- 1437 Khademian, M. and Imlay, J. A. (2017). *Escherichia coli* cytochrome c peroxidase is a respiratory oxidase that enables the use of  
1438 hydrogen peroxide as a terminal electron acceptor. *Proceedings of the National Academy of Sciences*, 114(33):E6922–E6931.
- 1439 Klumpp, S. and Hwa, T. (2014). Bacterial growth: Global effects on gene expression, growth feedback and proteome partition.  
1440 *Current Opinion in Biotechnology*, 28:96–102.
- 1441 Klumpp, S., Scott, M., Pedersen, S., and Hwa, T. (2013). Molecular crowding limits translation and cell growth. *Proceedings of the  
1442 National Academy of Sciences*, 110(42):16754–16759.
- 1443 Klumpp, S., Zhang, Z., and Hwa, T. (2009). Growth Rate-Dependent Global Effects on Gene Expression in Bacteria. *Cell*, 139(7):1366–  
1444 1375.
- 1445 Kostinski, S. and Reuveni, S. (2020). Ribosome Composition Maximizes Cellular Growth Rates in *E. coli*. *Physical Review Letters*,  
1446 125(2):028103.
- 1447 Kraemer, J. A., Sanderlin, A. G., and Laub, M. T. (2019). The Stringent Response Inhibits DNA Replication Initiation in *E. coli* by  
1448 Modulating Supercoiling of oriC. *mBio*, 10(4):822.
- 1449 Lascu, I. and Gonin, P. (2000). The Catalytic Mechanism of Nucleoside Diphosphate Kinases. *Journal of Bioenergetics and  
1450 Biomembranes*, 32(3):237–246.
- 1451 Laxhuber, K. S., Morrison, M. J., Chure, G., Belliveau, N. M., Strandkvist, C., Naughton, K. L., and Phillips, R. (2020). Theoretical  
1452 investigation of a genetic switch for metabolic adaptation. *PLOS ONE*, 15(5):e0226453.
- 1453 Lex, A., Gehlenborg, N., Strobelt, H., Vuillemot, R., and Pfister, H. (2014). UpSet: visualization of intersecting sets. *IEEE Transactions  
1454 on Visualization and Computer Graphics*, 20(12):1983–1992.
- 1455 Li, G.-W., Burkhardt, D., Gross, C., and Weissman, J. S. (2014). Quantifying absolute protein synthesis rates reveals principles  
1456 underlying allocation of cellular resources. *Cell*, 157(3):624–635.
- 1457 Liebermeister, W., Noor, E., Flamholz, A., Davidi, D., Bernhardt, J., and Milo, R. (2014). Visual account of protein investment in  
1458 cellular functions. *Proceedings of the National Academy of Sciences*, 111(23):8488–8493.
- 1459 Liu, M., Durfee, T., Cabrera, J. E., Zhao, K., Jin, D. J., and Blattner, F. R. (2005). Global Transcriptional Programs Reveal a Carbon  
1460 Source Foraging Strategy by *Escherichia coli*. *Journal of Biological Chemistry*, 280(16):15921–15927.
- 1461 Lu, D., Grayson, P., and Schulten, K. (2003). Glycerol Conductance and Physical Asymmetry of the *Escherichia coli* Glycerol Facilitator  
1462 GlpF. *Biophysical Journal*, 85(5):2977–2987.
- 1463 Lynch, M. and Marinov, G. K. (2015). The bioenergetic costs of a gene. *Proceedings of the National Academy of Sciences*,  
1464 112(51):15690–15695.
- 1465 Maaløe, O. (1979). *Regulation of the Protein-Synthesizing Machinery—Ribosomes, tRNA, Factors, and So On*. Gene Expression. Springer.
- 1466 Metzl-Raz, E., Kafri, M., Yaakov, G., Soifer, I., Gurvich, Y., and Barkai, N. (2017). Principles of cellular resource allocation revealed by  
1467 condition-dependent proteome profiling. *eLife*, 6:e03528.

- 1468 Mikucki, J. A., Pearson, A., Johnston, D. T., Turchyn, A. V., Farquhar, J., Schrag, D. P., Anbar, A. D., Priscu, J. C., and Lee, P. A. (2009). A  
1469 Contemporary Microbially Maintained Subglacial Ferrous "Ocean". *Science*, 324(5925):397–400.
- 1470 Milo, R., Jorgensen, P., Moran, U., Weber, G., and Springer, M. (2010). BioNumbers—the database of key numbers in molecular  
1471 and cell biology. *Nucleic Acids Research*, 38(suppl\_1):D750–D753.
- 1472 Monod, J. (1947). The phenomenon of enzymatic adaptation and its bearings on problems of genetics and cellular differentiation.  
1473 *Growth Symposium*, 9:223–289.
- 1474 Monod, J. (1949). The Growth of Bacterial Cultures. *Annual Review of Microbiology*, 3(1):371–394.
- 1475 Morgenstein, R. M., Bratton, B. P., Nguyen, J. P., Ouzounov, N., Shaevitz, J. W., and Gitai, Z. (2015). RodZ links MreB to cell wall  
1476 synthesis to mediate MreB rotation and robust morphogenesis. *Proceedings of the National Academy of Sciences*, 112(40):12510–  
1477 12515.
- 1478 Neidhardt, F. C., Ingraham, J., and Schaechter, M. (1991). *Physiology of the Bacterial Cell - A Molecular Approach*, volume 1. Elsevier.
- 1479 Ojkic, N., Serbanescu, D., and Banerjee, S. (2019). Surface-to-volume scaling and aspect ratio preservation in rod-shaped bacteria.  
1480 *eLife*, 8:642.
- 1481 Patrick, M., Dennis, P. P., Ehrenberg, M., and Bremer, H. (2015). Free RNA polymerase in *Escherichia coli*. *Biochimie*, 119:80–91.
- 1482 Peebo, K., Valgepea, K., Maser, A., Nahku, R., Adamberg, K., and Vilu, R. (2015). Proteome reallocation in *Escherichia coli* with  
1483 increasing specific growth rate. *Molecular BioSystems*, 11(4):1184–1193.
- 1484 Phillips, R. (2018). Membranes by the Numbers. In *Physics of Biological Membranes*, pages 73–105. Springer, Cham, Cham.
- 1485 Ramos, S. and Kaback, H. R. (1977). The relation between the electrochemical proton gradient and active transport in *Escherichia*  
1486 *coli* membrane vesicles. *Biochemistry*, 16(5):854–859.
- 1487 Ranganathan, S., Tee, T. W., Chowdhury, A., Zomorodi, A. R., Yoon, J. M., Fu, Y., Shanks, J. V., and Maranas, C. D. (2012). An  
1488 integrated computational and experimental study for overproducing fatty acids in *Escherichia coli*. *Metabolic Engineering*,  
1489 14(6):687–704.
- 1490 Rogers, H., Perkins, H., and Ward, J. (1980). *Microbial Cell Walls and Membranes*. Chapman and Hall, London.
- 1491 Roller, B. R. K., Stoddard, S. F., and Schmidt, T. M. (2016). Exploiting rRNA operon copy number to investigate bacterial reproductive  
1492 strategies. *Nature microbiology*, 1(11):1–7.
- 1493 Rosenberg, H., Gerdes, R. G., and Chegwidden, K. (1977). Two systems for the uptake of phosphate in *Escherichia coli*. *Journal of*  
1494 *Bacteriology*, 131(2):505–511.
- 1495 Rudd, S. G., Valerie, N. C. K., and Helleday, T. (2016). Pathways controlling dNTP pools to maintain genome stability. *DNA Repair*,  
1496 44:193–204.
- 1497 Ruppe, A. and Fox, J. M. (2018). Analysis of Interdependent Kinetic Controls of Fatty Acid Synthases. *ACS Catalysis*, 8(12):11722–  
1498 11734.
- 1499 Sánchez-Romero, M. A., Molina, F., and Jiménez-Sánchez, A. (2011). Organization of ribonucleoside diphosphate reductase during  
1500 multifork chromosome replication in *Escherichia coli*. *Microbiology*, 157(8):2220–2225.
- 1501 Schaechter, M., Maaløe, O., and Kjeldgaard, N. O. (1958). Dependency on Medium and Temperature of Cell Size and Chemical  
1502 Composition during Balanced Growth of *Salmonella typhimurium*. *Microbiology*, 19(3):592–606.
- 1503 Schmidt, A., Kochanowski, K., Vedelaar, S., Ahrné, E., Volkmer, B., Callipo, L., Knoops, K., Bauer, M., Aebersold, R., and Heinemann,  
1504 M. (2016). The quantitative and condition-dependent *Escherichia coli* proteome. *Nature Biotechnology*, 34(1):104–110.
- 1505 Scott, M., Gunderson, C. W., Mateescu, E. M., Zhang, Z., and Hwa, T. (2010). Interdependence of cell growth and gene expression:  
1506 origins and consequences. *Science*, 330(6007):1099–1102.
- 1507 Sekowska, A., Kung, H.-F., and Danchin, A. (2000). Sulfur Metabolism in *Escherichia coli* and Related Bacteria: Facts and Fiction.  
1508 *Journal of Molecular Microbiology and Biotechnology*, 2(2):34.
- 1509 Shi, H., Bratton, B. P., Gitai, Z., and Huang, K. C. (2018). How to Build a Bacterial Cell: MreB as the Foreman of *E. coli* Construction.  
1510 *Cell*, 172(6):1294–1305.
- 1511 Si, F., Le Treut, G., Sauls, J. T., Vadia, S., Levin, P. A., and Jun, S. (2019). Mechanistic Origin of Cell-Size Control and Homeostasis in  
1512 Bacteria. *Current Biology*, 29(11):1760–1770.e7.

- 1513 Si, F., Li, D., Cox, S. E., Sauls, J. T., Azizi, O., Sou, C., Schwartz, A. B., Erickstad, M. J., Jun, Y., Li, X., and Jun, S. (2017). Invariance of  
1514 Initiation Mass and Predictability of Cell Size in *Escherichia coli*. *Current Biology*, 27(9):1278–1287.
- 1515 Sirko, A., Zatyka, M., Sadowy, E., and Hulanicka, D. (1995). Sulfate and thiosulfate transport in *Escherichia coli* K-12: Evidence for a  
1516 functional overlapping of sulfate- and thiosulfate-binding proteins. *Journal of Bacteriology*, 177(14):4134–4136.
- 1517 Sohlenkamp, C. and Geiger, O. (2016). Bacterial membrane lipids: Diversity in structures and pathways. *FEMS Microbiology Reviews*,  
1518 40(1):133–159.
- 1519 Soufi, B., Krug, K., Harst, A., and Macek, B. (2015). Characterization of the *E. coli* proteome and its modifications during growth  
1520 and ethanol stress. *Frontiers in Microbiology*, 6:198.
- 1521 Stasi, R., Neves, H. I., and Spira, B. (2019). Phosphate uptake by the phosphonate transport system PhnCDE. *BMC Microbiology*, 19.
- 1522 Stouthamer, A. H. (1973). A theoretical study on the amount of ATP required for synthesis of microbial cell material. *Antonie van  
1523 Leeuwenhoek*, 39(1):545–565.
- 1524 Stouthamer, A. H. and Bettenhausen, C. W. (1977). A continuous culture study of an ATPase-negative mutant of *Escherichia coli*.  
1525 *Archives of Microbiology*, 113(3):185–189.
- 1526 Svenningsen, S. L., Kongstad, M., Stenum, T. S. n., Muñoz-Gómez, A. J., and Sørensen, M. A. (2017). Transfer RNA is highly unstable  
1527 during early amino acid starvation in *Escherichia coli*. *Nucleic Acids Research*, 45(2):793–804.
- 1528 Szenk, M., Dill, K. A., and de Graff, A. M. R. (2017). Why Do Fast-Growing Bacteria Enter Overflow Metabolism? Testing the  
1529 Membrane Real Estate Hypothesis. *Cell Systems*, 5(2):95–104.
- 1530 Taheri-Araghi, S., Bradde, S., Sauls, J. T., Hill, N. S., Levin, P. A., Paulsson, J., Vergassola, M., and Jun, S. (2015). Cell-size control and  
1531 homeostasis in bacteria. - PubMed - NCBI. *Current Biology*, 25(3):385–391.
- 1532 Taniguchi, Y., Choi, P. J., Li, G.-W., Chen, H., Babu, M., Hearn, J., Emili, A., and Xie, X. S. (2010). Quantifying *E. coli* proteome and  
1533 transcriptome with single-molecule sensitivity in single cells. *Science (New York, N.Y.)*, 329(5991):533–538.
- 1534 Tatusov, R. L., Galperin, M. Y., Natale, D. A., and Koonin, E. V. (2000). The COG database: a tool for genome-scale analysis of  
1535 protein functions and evolution. *Nucleic Acids Research*, 28(1):33–36.
- 1536 Taymaz-Nikerel, H., Borujeni, A. E., Verheijen, P. J. T., Heijnen, J. J., and van Gulik, W. M. (2010). Genome-derived minimal metabolic  
1537 models for *Escherichia coli* mg1655 with estimated in vivo respiratory ATP stoichiometry. *Biotechnology and Bioengineering*,  
1538 107(2):369–381. \_eprint: <https://onlinelibrary.wiley.com/doi/10.1002/bit.22802>.
- 1539 The Gene Ontology Consortium (2018). The Gene Ontology Resource: 20 years and still GOing strong. *Nucleic Acids Research*,  
1540 47(D1):D330–D338.
- 1541 Valgepea, K., Adamberg, K., Seiman, A., and Vilu, R. (2013). *Escherichia coli* achieves faster growth by increasing catalytic and  
1542 translation rates of proteins. *Molecular BioSystems*, 9(9):2344.
- 1543 van Heeswijk, W. C., Westerhoff, H. V., and Boogerd, F. C. (2013). Nitrogen Assimilation in *Escherichia coli*: Putting Molecular Data  
1544 into a Systems Perspective. *Microbiology and Molecular Biology Reviews*, 77(4):628–695.
- 1545 Virtanen, P., Gommers, R., Oliphant, T. E., Haberland, M., Reddy, T., Cournapeau, D., Burovski, E., Peterson, P., Weckesser, W.,  
1546 Bright, J., van der Walt, S. J., Brett, M., Wilson, J., Jarrod Millman, K., Mayorov, N., Nelson, A. R. J., Jones, E., Kern, R., Larson,  
1547 E., Carey, C., Polat, İ., Feng, Y., Moore, E. W., Vand erPlas, J., Laxalde, D., Perktold, J., Cimrman, R., Henriksen, I., Quintero,  
1548 E. A., Harris, C. R., Archibald, A. M., Ribeiro, A. H., Pedregosa, F., van Mulbregt, P., and Contributors, S. . . (2020). SciPy 1.0:  
1549 Fundamental Algorithms for Scientific Computing in Python. *Nature Methods*, 17:261–272.
- 1550 Volkmer, B. and Heinemann, M. (2011). Condition-Dependent Cell Volume and Concentration of *Escherichia coli* to Facilitate Data  
1551 Conversion for Systems Biology Modeling. *PLOS ONE*, 6(7):e23126.
- 1552 Vollmer, W., Blanot, D., and De Pedro, M. A. (2008). Peptidoglycan structure and architecture. *FEMS Microbiology Reviews*,  
1553 32(2):149–167.
- 1554 Weber, J. and Senior, A. E. (2003). ATP synthesis driven by proton transport in F1F0-ATP synthase. *FEBS Letters*, 545(1):61–70.
- 1555 Willsky, G. R., Bennett, R. L., and Malamy, M. H. (1973). Inorganic Phosphate Transport in *Escherichia coli*: Involvement of Two  
1556 Genes Which Play a Role in Alkaline Phosphatase Regulation. *Journal of Bacteriology*, 113(2):529–539.
- 1557 You, C., Okano, H., Hui, S., Zhang, Z., Kim, M., Gunderson, C. W., Wang, Y.-P., Lenz, P., Yan, D., and Hwa, T. (2013). Coordination of  
1558 bacterial proteome with metabolism by cyclic AMP signalling. *Nature*, 500(7462):301–306.

- 1559 Yu, X., Liu, T., Zhu, F., and Khosla, C. (2011). In vitro reconstitution and steady-state analysis of the fatty acid synthase from  
1560 *Escherichia coli*. *Proceedings of the National Academy of Sciences*, 108(46):18643–18648.
- 1561 Zhang, L., Jiang, W., Nan, J., Almqvist, J., and Huang, Y. (2014a). The *Escherichia coli* CysZ is a pH dependent sulfate transporter that  
1562 can be inhibited by sulfite. *Biochimica et Biophysica Acta (BBA) - Biomembranes*, 1838(7):1809–1816.
- 1563 Zhang, Z., Aboulwafa, M., and Saier, M. H. (2014b). Regulation of crp gene expression by the catabolite repressor/activator, cra, in  
1564 *Escherichia coli*. *Journal of Molecular Microbiology and Biotechnology*, 24(3):135–141.
- 1565 Zhu, M. and Dai, X. (2019). Growth suppression by altered (p)ppGpp levels results from non-optimal resource allocation in  
1566 *Escherichia coli*. *Nucleic Acids Research*, 47(9):4684–4693.

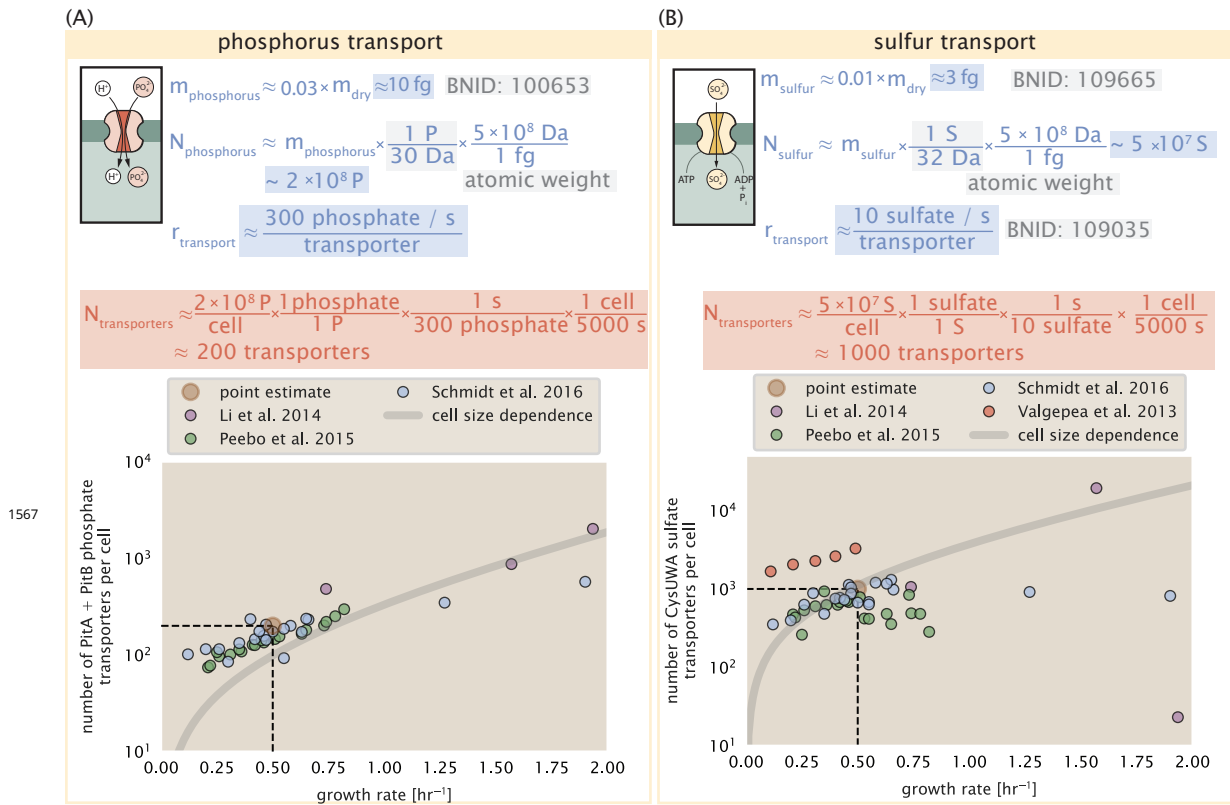


**Figure 2-Figure supplement 1.** (A) Estimate for the number of PitA phosphate transport systems needed to maintain a 3% phosphorus *E. coli* dry mass. Points in plot correspond to the total number of PitA transporters per cell. (B) Estimate of the number of CysUWA complexes necessary to maintain a 1% sulfur *E. coli* dry mass. Points in plot correspond to average number of CysUWA transporter complexes that can be formed given the transporter stoichiometry  $[CysA]_2[CysU][CysW][Sbp/CysP]$ . Grey line in (A) and (B) represents the estimated number of transporters per cell at a continuum of growth rates.

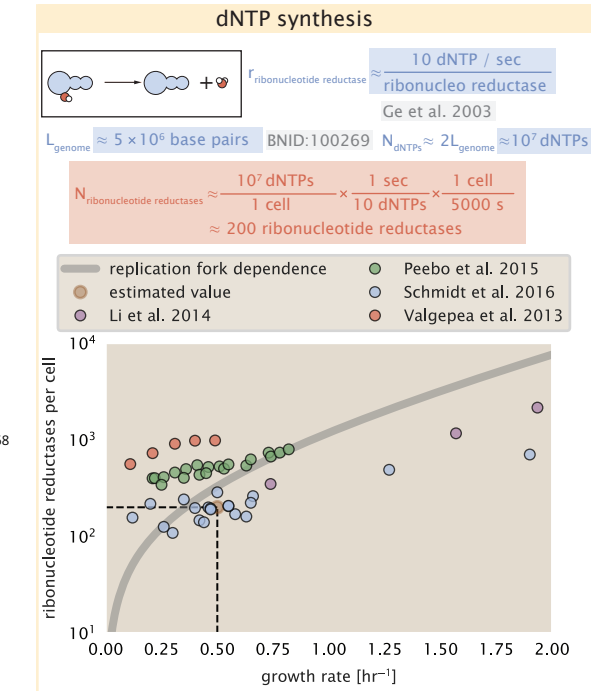


**Figure 6–Figure supplement 1.** Estimate of the number of ribonucleotide reductase enzymes needed to facilitate the synthesis of  $\approx 10^7$  dNTPs over the course of a 5000 second generation time. Points in the plot correspond to the total number of ribonucleotide reductase I ( $[NrdA]_2[NrdB]_2$ ) and ribonucleotide reductase II ( $[NrdE]_2[NrdF]_2$ ) complexes. Grey lines in top panel show the estimated number of complexes needed as a function of growth, the details of which are described in the Appendix.

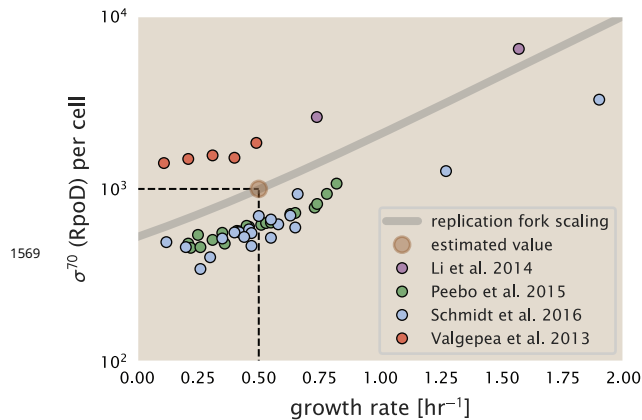


**Figure 7–Figure supplement 1.** The abundance of  $\sigma^{70}$  as a function of growth rate. Estimated value for the number of RNAP is shown as a translucent brown point and grey line.

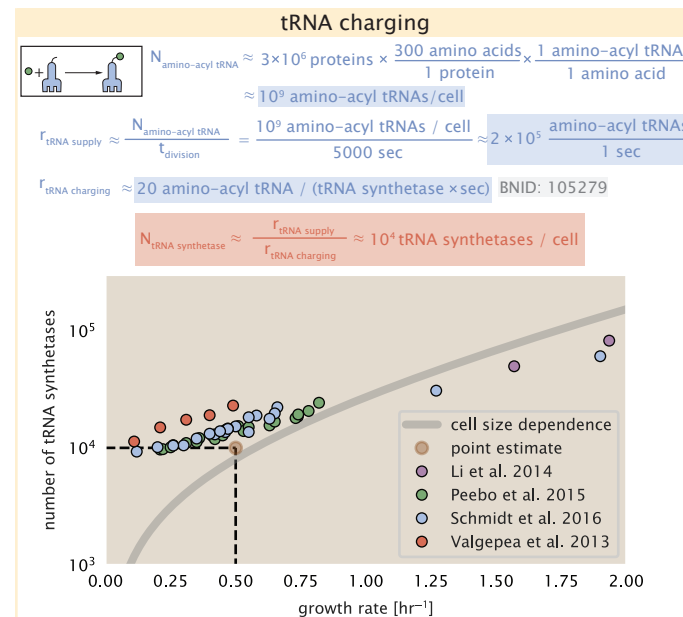


**Figure 8-Figure supplement 1.** Estimation for the number of tRNA synthetases that will supply the required amino acid demand. The sum of all tRNA synthetases copy numbers are plotted as a function of growth rate ([ArgS], [CysS], [GlnS], [GltX], [IleS], [LeuS], [ValS], [AlaS]<sub>2</sub>, [AsnS]<sub>2</sub>, [AspS]<sub>2</sub>, [TyrS]<sub>2</sub>, [TrpS]<sub>2</sub>, [ThrS]<sub>2</sub>, [SerS]<sub>2</sub>, [ProS]<sub>2</sub>, [PheS]<sub>2</sub>[PheT]<sub>2</sub>, [MetG]<sub>2</sub>, [lysS]<sub>2</sub>, [HisS]<sub>2</sub>, [GlyS]<sub>2</sub>[GlyQ]<sub>2</sub>).

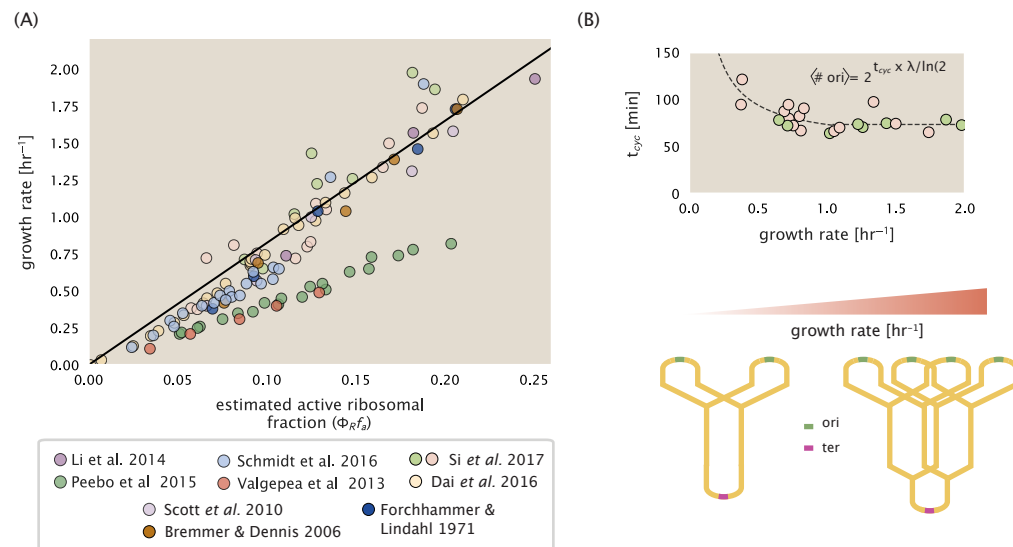


**Figure 9-Figure supplement 1.** (A) Actively translating ribosomal fraction versus growth rate. The actively translating ribosomal fraction is calculated using the estimated values of  $f_a$  from **Dai et al. (2016)** (shown in inset; see Appendix Calculation of active ribosomal fraction for additional detail). Additional measurements in addition to the proteomic measurements are based on measurements of cellular RNA to protein ratio, with  $\Phi_R \approx$  the cellular RNA to protein ratio divided by 2.1 (**Dai et al., 2016**). (B) Experimental measurements of the cell doubling time  $\tau$  and cell cycle time  $t_{\text{cyc}}$  from **Si et al. (2017)**. Dashed line shows fit to the data, which were used to estimate  $\langle \# \text{ori} \rangle$ .  $t_{\text{cyc}}$  was assumed to vary in proportion to  $\tau$  for doubling times greater than 40 minutes, and reach a minimum value of 73 minutes. See Appendix Estimation of  $\langle \# \text{ori} \rangle / \langle \# \text{ter} \rangle$  and  $\langle \# \text{ori} \rangle$  for additional details exact estimation of rRNA copy number. Red data points correspond to measurements in strain MG1655, while light green points are for strain NCM3722. Schematic shows the expected increase in replication forks (or number of ori regions) as *E. coli* cells grow faster.

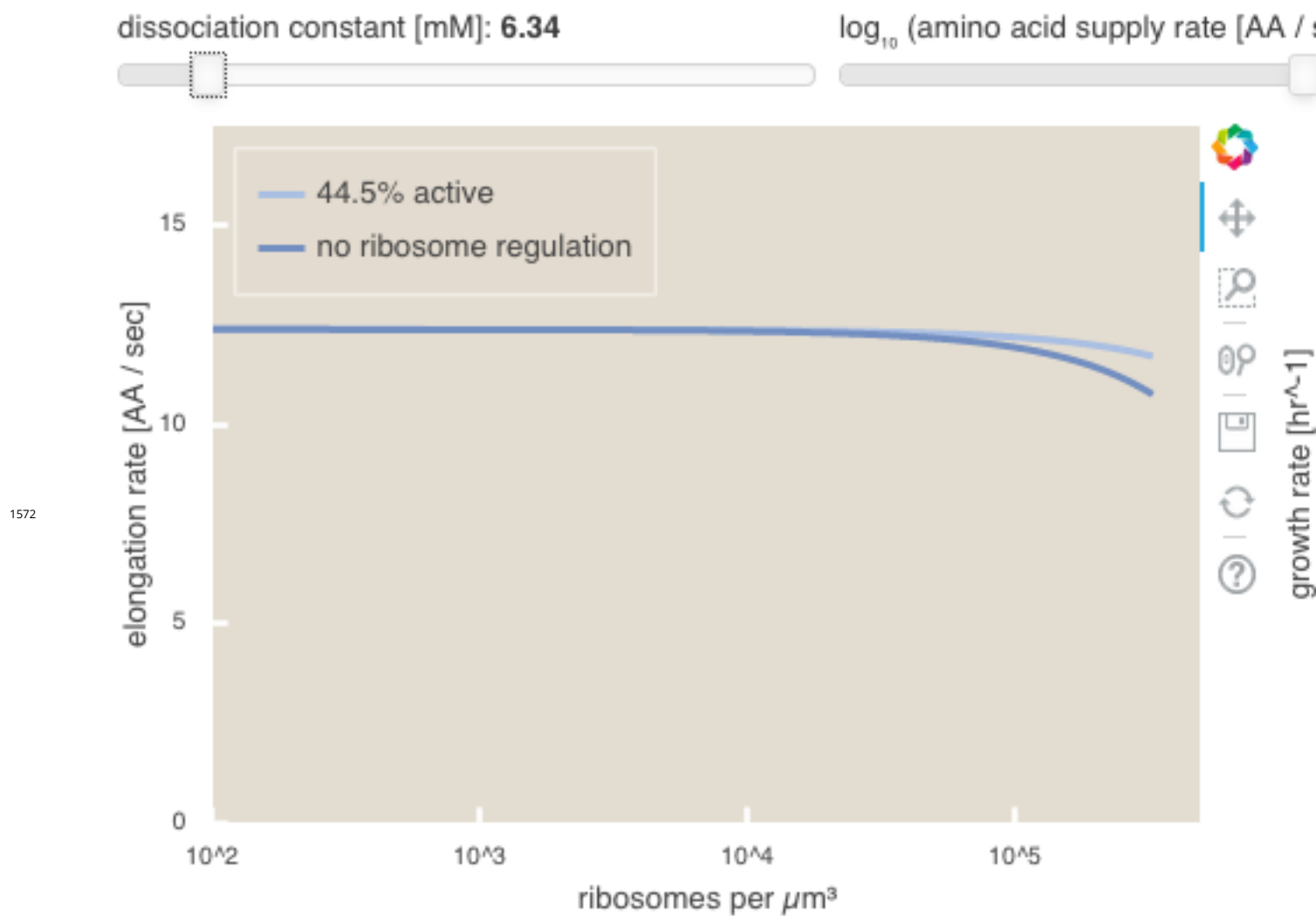


**Figure 11–Figure supplement 1.** An interactive version of parts (B) and (C) of **Figure 11** which permit the user to modulate the rate of amino acid supply, the dissociation constant of amino acids to the ribosome, and the fraction of the ribosome pool that is actively translating. This interactive figure, and the code used to generate it, is available on the [paper website](#).